020406-1-F

An Earth Longwave Radiation Climate Model

(NASA-CR-175749) AN EARTH LONGWAVE RADIATION CLIMATE MODEL Final Report (Michigan Univ.) 197 p HC A09/MF A01 N85-25984
CSCL 04B Unclas
G3/47 15133

SHI-KENG YANG

December, 1984

National Aeronautics and Space Administration
Langley Research Center
NASA Research Cooperative Agreement NCC1-76
Hampton, Virginia

Department of Atmospheric and Oceanic Science

THE UNIVERSITY OF MICHIGAN

COLLEGE OF ENGINEERING
Department of Atmospheric and Oceanic Science

AN EARTH LONGWAVE RADIATION CLIMATE MODEL

SHI-KENG YANG

NATIONAL AERONAUTICS AND SPACE ADMINISTRATION
LANGLEY RESEARCH CENTER
NASA RESEARCH COOPERATIVE AGREEMENT NCC1-76
HAMPTON, VIRGINIA

Administered through:

OFFICE OF RESEARCH ADMINISTRATION, THE UNIVERSITY OF MICHIGAN

ANN ARBOR, MICHIGAN

DECEMBER, 1984

PREFACE

This is the final report on research carried out under the two year (Jan. 1983 to Dec. 1984) cooperative agreement NCC1-76 "Application of Satellite Radiation Budget Measurements to Study Climate Processes of the Earth". Under this cooperative agreement Mr. Shi-Keng Yang, a graduate student in Atmospheric Science of the University of Michigan, worked with Dr. G. Louis Smith of the Atmospheric Sciences Division at NASA Langley Research Center.

The research accomplished consists of two parts:

(a) The development of a model which used climatological data for the Earth-Atmosphere system for the calculation of earth emitted radiation. This was the Ph.D. dissertation of Mr. Shi-Keng Yang, "An Earth Outgoing Longwave Radiation Climate Model", which constitutes the main part of this report.

(b) A study of atmospheric temperature lapse rate. The result of this study are summarized in a paper "Further Study on Atmospheric Lapse Rate Regimes", which has been submitted to the Journal of Atmospheric Sciences. An initial version of this paper appears in the semi-annual report on this project which was submitted in August, 1984.

Fred L. Bartman
Project Director

ABSTRACT

AN EARTH OUTGOING LONGWAVE RADIATION CLIMATE MODEL

by
Shi-Keng Yang

Chairmen: Fred L. Bartman, G. Louis Smitn

An Earth outgoing longwave radiation (OLWR) climate model has been constructed for radiation budget study. The model consists of the upward radiative transfer parameterization of Thompson and Warren (1982), the cloud cover model of Sherr et al. (1968) and a monthly average climatology defined by the data from Crutcher and Meserve (1971) and Taljaard et al. (1969). Additional required information is provided by the empirical 100mb water vapor mixing ratio equation of Harries (1976), and the mixing ratio interpolation scheme of Briegleb and Ramanathan (1982). Cloud top temperature is adjusted so that the the calculation would agree with NOAA scanning radiometer measurements. Both clear sky and cloudy sky cases are calculated and discussed for global average, zonal average and world-wide distributed cases. The results agree well with the satellite observations.

The clear sky case shows that the OLWR field is highly modulated by water vapor, especially in the tropics. The strongest longitudinal variation occurs in the tropics. This variation can be mostly explained by the strong water vapor gradient. Although in the zonal average case the tropics have a minimum in OLWR, the minimum is essentially contributed by a few very low flux regions, such as the Amazon,

Indonesia and the Congo. There are regions in the tropics such that their OLWR is as large as that of the subtropics. In the high latitudes, where cold air contains less water vapor, OLWR is basically modulated by the surface temperature. Thus, the topographical heat capacity becomes a dominant factor in determining the distribution.

Clouds enhance water vapor modulation of OLWR. Tropical clouds have the coldest cloud top temperatures. This again increases the longitudinal variation in the region. However, in the polar region, where temperature inversion is prominent, cloud top temperature is warmer than the surface. Hence, cloud has the effect of increasing OLWR. The implication of this cloud mechanism is that the latitudinal gradient of net radiation is thus further increased, and the forcing of the general atmospheric circulation is substantially different due to the increased additional available energy.

The analysis of the results also suggests that to improve the performance of the Budyko-Sellers type energy balance climate model in the tropical region, the parameterization of the longwave cooling should include a water vapor absorbing term.

AN EARTH OUTGOING LONGWAVE RADIATION CLIMATE MODEL

by
Shi-Keng Yang

A dissertation submitted in partial fulfillment
of the requirements for the degree of
Doctor of Philosophy
(Atmospheric Science)
in The University of Michigan
1984

Doctoral Committee:

Professor Fred L. Bartman, Co-chairman
G. Louis Smith, Co-chairman; Senior Scientist,
NASA Langley Research Center, Hampton, Virginia
Professor David M. Gates
Professor William R. Kuhn

AKNOWLEGEMENTS

I am indebted to my dissertation co-chairmen, Professor Fred L. Bartman and Dr. G. Louis Smith. Fred has been my mentor throughout my graduate study. His immense intellectual and spiritual support have been a real source of encourgement to me over the past several years. Louis has patiently guided my research for the last two years and has provided me with enlightening discussions concerning both my life and aspects that have been fundamental to the completion of this work.

Appreciation is also extended to the committee members Professor William R. Kuhn for his valuable suggestions and criticism and Professor David M. Gates for his constructive review.

Many people have contributed to this work: Mr. Edwin Harrison and Dr. Tim Suttles not only helped in arranging my two-year visit at Langley Research Center, but also commented on the manuscripts; discussions with Fellows of the Radiation Science Branch have been very fruitful. The help of Dale Bess, who has kindly allowed me to use his unpublished results, and Mary Alice Woerner, who assisted in debugging many programs, are also acknowledged.

Without the moral support from my parents and my fiancée, Chen-lin, none of this would have been possible.

This work has been sponsored by NASA Grant NCC1-76.

TABLE OF CONTENTS

CHAPTER

LIST OF TABLES

Table

LIST OF FIGURES

Figure

LIST OF SYMBOLS

A_c	cloud cover
A, B, C_1, C_2	coefficents for outgoing longwave parameterization
e	water vapor pressure
e_s	saturation water vapor pressure
F	outgoing longwave flux
gph	geopotential height
P	pressure
Q	specific humidity
RH	relative humidity
$\underline{RH}$	height weighted mean relative humidity
T_c	cloud top temperature
T_s	surface temperature
W	mixing ratio
z	height

LIST OF ABBREVIATIONS

GCM	General Circulation Model
GOES	Geosynchronous Operational Enviromental Satellite
HIRS	High Resolution Infrared Sounder
ITCZ	Inter-Tropical Convergence Zone
LIMS	Limbs Infrared Measurements of Stratospheric gases
LW	Longwave
MH	Minnis and Harrison
MSU	Microwave Sounding Unit
NCAR	National Center for Atmospheric Research
OLWR	Outgoing Longwave Radiation
OLWF	Outgoing Longwave Flux
RMS	Root Mean Square
OR	Oort and Rasmusson
SW	Shortwave
T.O.A.	Top Of the Atmosphere
TW	Thosmpson and Warren

LIST OF APPENDICES

CHAPTER 1

INTRODUCTION

1.1 Background

The Earth radiation budget characterizes climate. Net radiation, the difference between the absorbed solar radiation and earth emitted outgoing longwave (LW) radiation, defines the regions of energy sources and energy sinks. These are the dynamic force driving the atmosphere-ocean system. An understanding of the radiative processes and distribution of the radiation energy is important to gaining insight into weather and climate processes, and hence is important to improving our prognostic ability, which is one of the most fundamental problems in atmospheric science.

Earth outgoing LW radiation is an indication of Earth-atmosphere conditions. Its temporal and spatial variations result from changes in the Earth-atmosphere properties. For example, Lau and Chan (1983) used LW as an indicator for studying teleconnections; Gill and Rasmusson (1983) and Quiroz (1983) used the LW anomaly to analyze the latest " El Niño" event.

The introduction of the time-space dependent radiation field into numerical prediction schemes will hopefully increase predictability in extended weather forecasts (Wang et al., 1983). The study by Belov et al. (1971) incorporating radiative heat influx in numerical forecasting is another example. In the case of short-term climate prediction, radiation maps provide one more set of sample data of present day statistics for anomaly analysis, which appears to be the only method used in current operational climate forecasts. Many theoretical energy balance climate models are simplified to zonally-averaged 1-D models for economy of computation. Although this energy balance concept has been widely used in theoretical climate models, e.g. Budyko (1969) and Sellers (1973), it has not been applied to real time forecasts except for the work of Adem (1969 and 1981), who used an energy balance model to forecast sea temperature anomalies and drought with limited successes. This simplification filters out longitudinal variations, including the so called monsoonal circulation, hence some interesting pheonomena of the outgoing LW radiation features vanish. On the other hand, the top of the hierarchy of climate models, GCMs, are more dynamically oriented, but the radiation budget has not been well simulated yet (Herman, 1981).

Radiation budget measurements have long been performed at ground bases. London (1957) summarized zonally averaged radiation components in this manner. It was not until the Explorer 7 satellite (Suomi, et al., 1960) that it was possible to directly measure the earth-space radiation exchange, regardless of its crude instrument resolution. The Nimbus 6 Earth Radiation budget (ERB) Experiment started a continuous time series of measurements in July 1975, which were later succeeded by Nimbus 7 ERB. Bess, et al. (1981), using the method developed by Smith and Green (1981), analyzed the LW from the first year of Nimbus 6 ERB data thereby revealing some interesting intra-annual variations. This method enhances the instrument resolution of the wide-field-of-view radiometer. Campbell and Vonder Haar (1980) averaged data from some satellite observations and formed a climatology of radiation budget measurements, which provides very broad information on all the earth radiation components. Some of the radiation features described by these authors have been qualitatively explained. The questions on how the radiation field affects weather and climate still need to be explored. Beginning in October 1984, the Earth radiation budget experiment (ERBE) onboard the ERBE satellite and NOAA-F satellite will continue to update the measurements with more advanced instruments and data analysis procedures.

Bartman (1980 and 1981) first built a radiation budget oriented global albedo climate model. This 2-D model empirically describes the solar radiation transfer process on the earth surface and in the atmosphere and calculates planetary albedo at the top of the atmosphere for each $10^\circ \times 10^\circ$ grid interval. This model can also serve as a reference for the climate model in specifying the absorbed solar radiation of each region, the radiative heating. No similar work, however, has been done on earth emitting LW radiation, the radiative cooling. An Earth outgoing longwave radiation climate model of this kind will be important to the understanding of our Earth-atmosphere climate.

1.2 Current Work

To simulate the earth's outgoing LW radiation field, a 2-D longitude-latitude varying outgoing LW radiation climate model is constructed. The seasonal variation of LW radiation due to variation in surface temperature, cloud cover, cloud top temperature and moisture, the most influential elements, will be studied. The model also provides a tool to study some interesting features of the LW field, such as the LW maximum in the subtropics and drastic longitudinal variations along the tropics.

The model consists of a radiation calculation and a data base of climatologies of the input parameters, i.e. the monthly average fields of surface temperature, cloud cover, cloud top temperature and moisture over the globe. For efficiency, a parameterization by Thompson and Warren (1982), which is derived from Wiscombe's radiative transfer model (1976), is used for the radiation calculation. This will be discussed in Chapter 2.

For describing climatologies of input parameters, a $10^o \times 10^o$ grid system is selected. A climatological data set from Crutcher and Meserve (1970) and Taljaard _et_ _al_. (1971) is used to provide temperatures, dew point and geopotential height for various altitudes. This will be discussed in Chapter 3.

In Chapter 4, because of the lack of data at 300mb and 200mb, the interpolation method used by Briegleb and Ramanathan (1982) is incorporated to get 300mb and 200mb specific humidities with the formula derived by Harries (1976) for 100mb. Also a theoretical climatology of clear sky outgoing LW radiation is presented.

In Chapter 5, Sherr _et al_. (1968) cloud type classification and cloud cover data are incorporated with satellite observations to derive a scheme for determining cloud top temperature. In Chapter 6, the calculated cloudy sky outgoing longwave radiation is discussed in detail. Finally, the conclusions and recommendations are stated in Chapter 7. In most cases, only the results of the extreme seasons, January and July, are discussed. The cases of the transient seasons, April and October, are generally more moderate for all the features. These results are organized in the Appendices for comparison.

Fig.1 summarizes the methodology of this outgoing LW radiation climate model. This model explains quantitatively each parameter's contribution to the LW field, and thus gives a better understanding of the physics of longwave radiation in the earth climate.

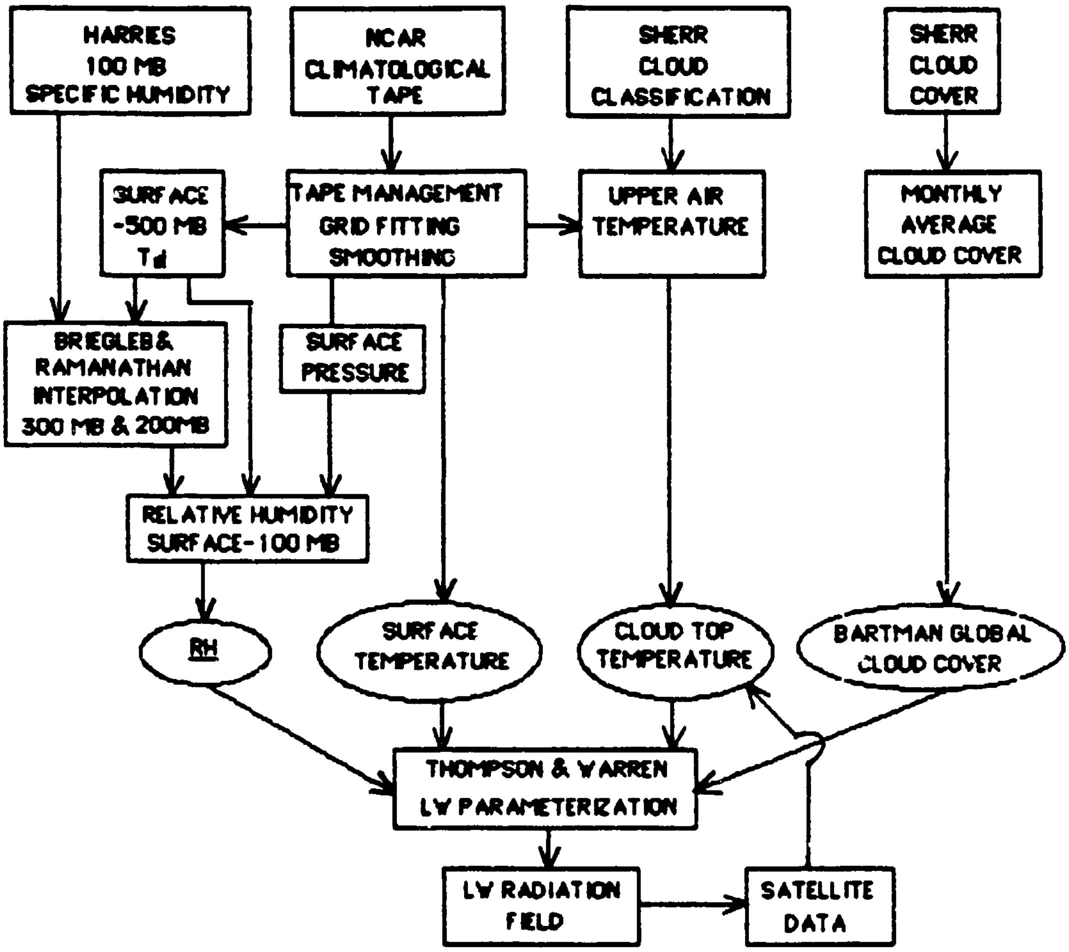

FIGURE 1. METHODOLOGY OF EARTH OUTGOING LONG WAVE CLIMATE MODEL
<u>RH</u> is height weighted mean relative humidity, see chapter 2.

CHAPTER 2

PARAMETERIZATION OF EARTH OUTGOING LONGWAVE RADIATION

2.1 Introduction

As briefly mentioned in the previous chapter, an Earth outgoing longwave radiation (OLWR) parameterization by Thompson and Warren (1982, hereafter denoted as TW) is used for this study. In section 2.1, the reason for choosing this parameterization is discussed. In section 2.2, the different parameterizations of OLWR are reviewed, and in section 2.3, the TW parameterization is outlined and discussed.

2.1.1 Longwave Parameterization and Climate Model

In spite of the fact that the basic radiative transfer equation is simple for the plane-parallel atmosphere, the solutions are not straightforward for the reasons that (1) the atmosphere is inhomogeneous and (2) the molecular absorption spectra are extremely complicated. Often a band model is used to alleviate the cumbersome line-by-line integration of absorption for transmission functions. Also the Curtis-Godson approximation is widely used to replace an inhomogeneous optical depth with an equivalent homogeneous one. Nevertheless the selection of bandwidth and the treatment of the distribution of line strengths are somewhat arbitrary, e.g. band width could be as narrow as $10 cm^{-1}$ for a narrow band model to more than $100 cm^{-1}$ for a wide band model. The classic Elsasser regular band model and Goody random model are the backbone of most derivations.

To verify band models, a detailed line-by-line calculation is indispensable. Drayson (1967) first performed the calculation with very fine line width of 0.001 cm^{-1} over line center and 0.1 cm^{-1} over line wings and integrated over very thin layers so that the inhomogeneous path could be accounted for.

McClatchey _et al_. (1972) compiled absorption line data, from microwave to the visible, not only for CO_2, O_3 and H_2O bands but as well for the other trace gases which are radiatively active in the earth atmosphere. This set of absorption line data is being updated constantly and currently contains 159,000 lines. It is the most complete data tape available. McClatchey _et al_. also developed a line-by-line calculation program for transmisson and radiation, FASCODE. The main problem in intercomparing detailed line-by-line models with band models using published results is that different models have different input conditions and different resolutions (Luther, 1983), which makes direct comparison with output results meaningless. Luther has conducted a workshop in 1984 to compare the results from different models. Some of the preliminary results have shown that great uncertainty on the water vapor continuum absorption could cause significant error. This work will substantially improve our understanding of the performance of radiation models.

A detailed radiative transfer model is expensive to use. Even a one-dimension Quasi-Random model takes a few seconds computation time. To calculate a 10 ° x 10 ° grid global distribution 648 grid points is very costly. A well parameterized radiative scheme can give results as good as the radiative transfer model. Also, parameterization creates an indispensable interface with available input data.

Based on these arguments, a parameterization is selected for this study to calculate outgoing LW radiation directly.

2.2 A Review of Earth Outgoing Longwave Radiation Parameterization

Budyko (1969) empirically parameterized the Earth's outgoing LW radiation using monthly data of 260 stations as

$$F= a+bT-(a_1+b_1T)C \qquad 2.1$$

Where F is outgoing LW radiation at the top of atmosphere in w/m^2

T is the surface temperature.

C is cloud cover.

a,b,a_1 and b_1 are constants.

This formulation was compared with the result of the theoretical radiative transfer model of Manabe and Wetherald (1967) and claimed to be in good agreement for the clear sky case but with some differences for the cloudy sky case (Budyko, 1969).

Subsequently, a series of experiments was performed on the derivation of coefficients using either an empirical approach or a theoretical model calculations, such as Schneider (1972), Cess (1974) and Gupta et al. (1978). A summary of these coefficients are tabulated in Table A.18. It is clear that they are in good agreement for the global average case.

As pointed out by Thompson and Warren (1982), the disadvantages of empirically derived parameterzations are:

(1) the coefficients vary from data set to data set. Currently there is no generally recognized best value of b for equ.2.1. Recently Short *et al*. (1984) have shown that b is temporally and spacially dependent in the tropics.

(2) When two physically distinguishable but highly correlated factors, such as cloud and humidity, both influence F, it is very difficult to separate them and establish their relative magnitude by regression analysis.

The advantage of the empirical approach is that the parameterization might implicitly account for some unsuspected feedback effect in the climate system that might otherwise be neglected in a climate model. On the other hand, the advantage of the parameterization derived from the transfer model is that the relation between input atmospheric condition and the corresponding output F are perfectly known. The disadvantage is that the result would possess the defects of the model. For example, the concentration of stratospheric water vapor is not well known yet (see Chapter 4). In most radiative transfer models it is assumed to be about 3ppm. Altering stratospheric water vapor concentration would change the longwave opacity and thus the outgoing LW flux. Wang *et al*. (1976) estimated that doubling water vapor concentration would decrease LW flux by about $2W/m^{-2}$. Therefore, a model could have a potential error due to the difference between the assumption and the true value. A parameterization derived from such a model would thus inherit this error as well.

Different formulations of the outgoing LW radiation have been tried by other investigators, especially to avoid the uncertainty of cloud amount. Sellers (1969) used an atmospheric attenuation coefficient to replace cloudiness in a simple zonally averaged climate model. Fromm (1982) and Jensenius et al. (1978) derived a parameterization using other meteorological parameters, such as pressure tendency, wind magnitude, vorticity, etc., which cloudiness is implicitly related to. This approach is relevent for short term numerical model applications.

Since the intriguing question of how the temporal and spacial variation of water vapor impact on the outgoing LW radiation is the focus of this study, the Thompson and Warren (1982) parameterization is chosen for its special feature of water vapor as an input predictor. This allows one to study the relative impacts on the outgoing LW radiation of both cloud and water vapor. For example, in the zonally averaged case, the outgoing LW radiation exhibits a minimum near the equator 20 to 40 W/m^2 smaller than the peaks at the subtropics. In a calculation by Warren and Thompson (1983), they found that one third of the dip can be explained by the variation of atmospheric water vapor. Only a small fraction is attributed to cloudiness, if the published cloud climatology is used. The rest remains unexplained. They thus suspect that the cirrus and cumulonimbus amounts near equator are much higher than the published cloud climatology. In chapter 4, we will further discuss how the atmospheric water vapor modulates outgoing LW radiation.

A brief discription of the important features of this parameterization follows, as well as some crucial information not mentioned in the original work.

2.3 Thompson and Warren Parameterization

2.3.1 Wiscombe Model

In Thompson and Warren (1982), outgoing LW parameterization is derived from a radiative-transfer model. The model used is Wiscombe (1975) ATRAD, which employs the exponential-sum-fitting of transmision function method. Essentially the transmission functions are those of LOWTRAN 5 (Kneizys et al., 1980). The LW spectrum is covered from 3 to 500 μ m, but differs from LOWTRAN 5 in that water vapor continuum is included. This is important in the tropics with its high water vapor content; omission of the continuum absorption in the radiative transfer calculation in early GCMs led to the calculation of very low atmospheric temperatures.

2.3.2 Assumptions

1) Major Gases:

Mixing ratios of the gases, CO_2, N_2O, CH_4, CO, N_2 and O_2 remain constant at all altitudes at the following values: 320, 0.28, 1.6, 0.075, 7.965×10^5 and 2.095×10^5 ppm respectively. Current prominent attention on the climatic impact of anthropogenic CO_2 increase leads to the question of how outgoing LW radiation responds. Increaing the concentration of CO_2 in the atmosphere will result in:

(1) an increase of tropospheric-surface temperature because of the greenhouse effect. This can be measured from the net change in LW flux at the tropopause (Ramanathan et al., 1979).

(2) Cool stratospheric temperature resulting from increasing stratospheric opacity, i.e. more effective emission.

However, the influence on the outgoing LW at the top of the atmosphere is roughly a factor of 2 smaller than the net change of LW at the tropopause. Doubling the CO_2 concentration will only change outgoing LW radiation at the T.O.A. about 2 w/m^2. Error from neglecting the variation of CO_2 is smaller than the errors from other sources, such as data error and cloud fraction. A broad band channel which measures the total outgoing LW is not sensitive enough to detect such a small fractional variation. However an instrument on a satellite using a narrow channel centered at the CO_2 absorption band can detect more significant change in that spectral range due to atmospheric CO_2 change (Kiehl, 1983 and Charlock, 1984b).

2) Ozone:

Ozone O_3 profiles are interpolated from the McClatchey (1972) model atmosphere. In the LW spectrum, O_3 is only significant at the 9.6 μm band. Changing the O_3 concentration causes significant change in the outgoing flux of this band only; for broad band the total change is very small. For example, a change of O_3 concentration from the tropical atmospheric value (.246 atm cm) to its mid latitude atmospheric value (.345 atm cm), changes the outgoing flux for the 9.6um band (1000 to $1120cm^{-1}$) about $3.7w/m^2$, but the whole LW spectrum (400 to 1400cm^{-1}) only changes about 4.3 w/m^2 (Charlock, 1984a). In the cloudy sky case, fixing the O_3 distribution should have less error.

3.) Aerosols:

The question of the possible impact of increasing aerosols on climate is gaining as much attention as the CO_2 greenhouse effect these days. Some inconclusive conjectures predict that anthropogenic aerosols' impact will be of the same order as that of CO_2 in the future. Nevertheless, modeling aerosols is far more complicated than CO_2 (Ramanathan and Coakley, 1978). Unlike CO_2, aerosols are a more localized problem, which do not diffuse homogeneously to the whole atmosphere. In the United States, current aerosol concentration in urban areas can be three times greater than those over rural areas. Fallout time of normal tropospheric aerosols is 1 to 2 weeks, while that of stratospheric aerosols can be as long as years. Thus the concentrations, size distributions (.01 to 20 µm) and optical properties have high dependence on both time and space.

Aerosols not only reduce outgoing longwave radiation as does CO_2 or any other atmospheric constituents, but also scatter and absorb incoming solar radiation covering the entire spectrum. The scattering-absorption processes can result in either increase or decrease of planetary albedo depending on the nature of a particular type of aerosol. Some absorb (scatter) more solar energy than they scatter (absorb), which will decrease (increase) planetary albedo when the concentration increases. Hence, the sign of heating on the earth surface temperature from increasing aerosol would be from the difference of the two processes: the net planetary albedo change and the decrease of outgoing longwave radiation. Coakley and Grams (1976) found that both small particles (radii smaller than 0.05 µm) and large particles (radii larger than 1.0 µm) generally have a greater influence on longwave radiation than on incoming solar radiation, therefore these particles contribute to warming the surface temperature. Particles of the intermediate size affect the incoming solar radiation more strongly than they affect the longwave radiation and thus contribute to cooling the surface temperature. Reck (1974) and Wang and Domoto (1974) also found that the surface albedo has a crucial role in determining the sign of heating. When the surface albedo is higher than a critical value, increasing aerosols will cause surface temperature warming. However, not all of the study results agree. Most of these experiments were carried out with the one dimensional radiative convective models or energy balance models with the size distribution of spherical particle between 0.1 µm and 1 µm, which is not representative in simulating a localized problem. One can thus only expect to gain the qualitative understanding of aerosol physics.

In conclusion, these studies showed that the aerosol self competing effects might have important climatic influence on the surface temperature. For the purpose of the present investigation on outgoing LW radiation, the effect of aerosols will be neglected.

4) Surface emissivity:

Surface emissivity is assumed fixed at .95 by the TW parameterization. Data of global distribution of surface emissivity are not available yet. In the 8 to 14 µm region, which accounts for most of the surface radiation contribution to outgoing LW radiation, this is the intermediate between extremes of .90 for sand desert and .99 for snow. Ocean is about .98. Outside this window band the variation of surface emissivity has little effect on the outgoing LW radiation from the surface. TW showed that a change of .05 in surface emissivity will vary clear sky outgoing LW radiation by only 1 to 3 W/m^2 depending on atmospheric opacity.

5) Discontinuity of temperature at the surface:

Surface and surface-air temperatures are assumed equal. In fact there is usually a few degrees Kelvin difference of diurnal mean temperatures between surface air and ground temperature. Tests show that a one degree temperature difference between surface-air and ground would contribute a .7 to 1.5 W/m^2 change in clear sky outgoing LW (Thompson and Warren, 1982), which means that with this assumption the model can not simulate well the LW diurnal variation. For monthly averaged cases, this assumption has little effect on monthly mean outgoing LW.

6) Surface Elevation.

Surface elevation is not included as a predictor of F. In the case of low temperature, such as in the Antarctic, this assumption contributes little error because there is less water in the air column. However, if the surface temperature is higher, such as in Tibet, the error can be higher. TW tested this by chan,ing surface pressure from 1013mb to 700 mb, which can increase outgoing LW by $8w/m^2$ if the 40^oN zonal average temperature is used. However, if the local temperature, which is lower than zonal average temperature, is used, the difference will substantially decrease. For very high elevation, the surface temperature is generally lower, which will reduce water vapor content, and thus produce less error.

2.3.3 Predictors and Characteristics of Parameterization

The parameterization now has the form:

$$F=C_1-C_2A_c \qquad 2.2$$

where C_1 and C_2 are coefficients, and are now functions of surface temperature, cloud top temperature and height weighted mean relative humidity which will be further discussed later. A_c is effective cloud fraction, C_1 accounts for the clear sky ougoing LW, and C_2A_c is the modification term which accounts for the effect of cloudiness on the outgoing LW.

A more physically straightforward form of equ 2.2 is

$$F=C_1(1-A_c)+C'_2A_c \qquad 2.3$$

where $C'_2=C_1-C_2$. This equation simply separates the clear sky part from the overcast part. However, equation 2.2 is more often used because $C_2= dF/dA_c$ measures the cloud LW feedback (Cess and Ramanathan, 1978).

For outgoing LW budget on a global scale, the surface radiation contributes about 10 to 15%, the atmosphere about 24% to 54% and the remaining is cloud radiation (Wallace and Hobbs, 1977). The infrared cooling of the troposphere is highly dependent on the temperature at different levels of the atmosphere. Since the temperature sounding profiles at most latitudes have similar characteristics (Liou, 1980), using surface temperature to represent both surface and atmospheric LW emission is a very relevant and convenient simplification. As altitude increases, the absorbent contents decrease, and the atmosphere above becomes more transparent. Above the cloud top, generally it is clear enough for cloud radiation to escape to outer space very efficiently. Thus, using cloud top temperature as another predictor is well justified.

Another predictor, effective cloudiness, is a simplification of compressing multilayer clouds into one simple black cloud layer. In reality, this assumption may be valid for single layer low thick clouds. The high thin cirrus type clouds generally exhibit spectral emissivities smaller than .5. In those cases without overlapping, the effective cloudiness would be emissivity times cloud fraction A_c, such that a grid area is divided into a simple clear part and an overcast part. This is a very idealistic assumption. However, until one knows more about complex cloud behavior, this is a feasible approach in terms of modeling. Clouds will be further discussed in Chapter 5.

Atmospheric water vapor is the most efficient LW absorber. As observed from the space, one would find that atmospheric water vapor is the only LW sink compared to the other three predictors, T_S, T_C and A_C, just discussed above. In the earlier empirical LW parameterization, this term is often omitted probably due to lack of simultaneous observation. As will be discussed in Chapter 4, even in this modern age there are still some substantial problems in the measurement of atmospheric water vapor. Yet there are many ways to describe atmospheric water vapor, namely relative humidity, dew point, mixing ratio, specific humidity or precipitable water. For the TW parameterization, relative humidity is chosen from a perturbation test on the McClatchey atmospheres (McClatchey et al, 1972). They changed the tropospheric temperature lapse rate, which is not included as a predictor, in Wiscombe's radative transfer model, and used different water vapor parameters to calculate outgoing LW flux. They found that the results are not sensitive to lapse rate change if relative humidity is used. Therefore they defined a height weighted mean relative humidity as:

$$\underline{RH} = \frac{1}{12\ \mathrm{km}} \int_0^{12\mathrm{km}} RH(z)\, dz \qquad 2.4$$

This predictor gives greater weight to relative humidity at high altitudes, because high altitudes are more transparent to space than the lower levels and therefore contribute more to F. Using 12km as the upper limit for integration is mainly due to the convenience of parameterzation. The altitude of 12km is approximately the average height of the tropopause. This simplification eliminates the latitudinal and seasonal variation of the tropopause height, which is above 12km at the tropics and below 12km at higher latitudes. The error of underestimating tropopause height at the tropics and overestimating in the higher latitude is difficult to measure due to lack of observation in this region. This will be further discussed in Chapter 4.

Tables 2.1 and 2.2 from TW show the parameterization of C_1 and C_2 respectively. Corresponding figures 2.1 and 2.2 illustrate C_1 as a function of surface temperature and height weighted mean relative humidity $\underline{RH}$, and C_2 as a function of $\underline{RH}$ and the temperature difference between the surface and cloud top.

Table 2.1 Parameterization for clear-sky outgoing IR irradiance at the top of the atmosphere ($z = 50$ km) after TW.

c_1 = outgoing clear sky IR (W m $^{-2}$).

T_s = surface air temperature (°C) ($-118°C < T_s < 57°C$).

$\underline{RH}$ = height-mean relative humidity from 0 to 12 km (Eq. 2.4) ($0.2 < \underline{RH} < 1.0$).

PARAMETERIZATION:

$$c_1 = a_o + a_1T_s + a_2T_s{}^2 + a_3T_s{}^3, \text{ where}$$

$$a_n = b_{0n} + b_{1n}\underline{RH} + b_{2n}\underline{RH}^2, \; n = 0, 1, 2, 3.$$

n = 0

$b_{00} = 2.43414 \times 10^2$
$b_{10} = -3.47968 \times 10^1$
$b_{20} = 1.02790 \times 10^1$

n = 1

$b_{01} = 2.60065 \times 10^0$
$b_{11} = -1.62064 \times 10^0$
$b_{21} = 6.34856 \times 10^{-1}$

n = 2

$b_{02} = 4.40272 \times 10^{-3}$
$b_{12} = -2.26092 \times 10^{-2}$
$b_{22} = 1.12265 \times 10^{-2}$

n = 3

$b_{03} = -2.05237 \times 10^{-5}$
$b_{13} = -9.67000 \times 10^{-5}$
$b_{23} = 5.62925 \times 10^{-5}$

Table 2.2 Parameterization of cloud modification term for outgoing IR irradiance at the top of the atmosphere ($z = 50$ km) after TW

c_2A_c = cloud modification term (W m^{-2}) [see Eq. (2.2)].

A_c = fractional total cloud amount.

$T_{sc} = T_s - T_c$ ($0 < T_{sc}$, 60K).

T_s = surface air temperature (-118°C $< T_c <$ 57°C).

T_c = cloud top temperature (-118°C $< T_c <$ 57°C).

$\underline{RH}$ = height-mean relative humidity [Eq. (2.4)]
($0.2 < \underline{RH} < 1.0$).

PARAMETERIZATION:

$$c_2 = c_1\ (T_s, \underline{RH}) - c_1(T_c, \underline{RH}) + f(T_{sc}, \underline{RH})$$
(for c_1 see Table 2.1)

$$f(T_{sc}, \underline{RH}) = f_1(T_{sc}) + f_2(T_{sc}, \underline{RH})$$

$$f_1 = d_0 + d_1T_{sc} + d_2T^2{}_{sc}$$

$$f_2 = d_3T_{sc}(T_{sc} + d_4)\ (\underline{RH} + d_5)$$

$d_0 = -3.1$

$d_1 = -0.4146$

$d_2 = 4.084 \times 10^{-3}$

$d_3 = -4.44 \times 10^{-3}$

$d_4 = 80.0$

$d_5 = -0.40$

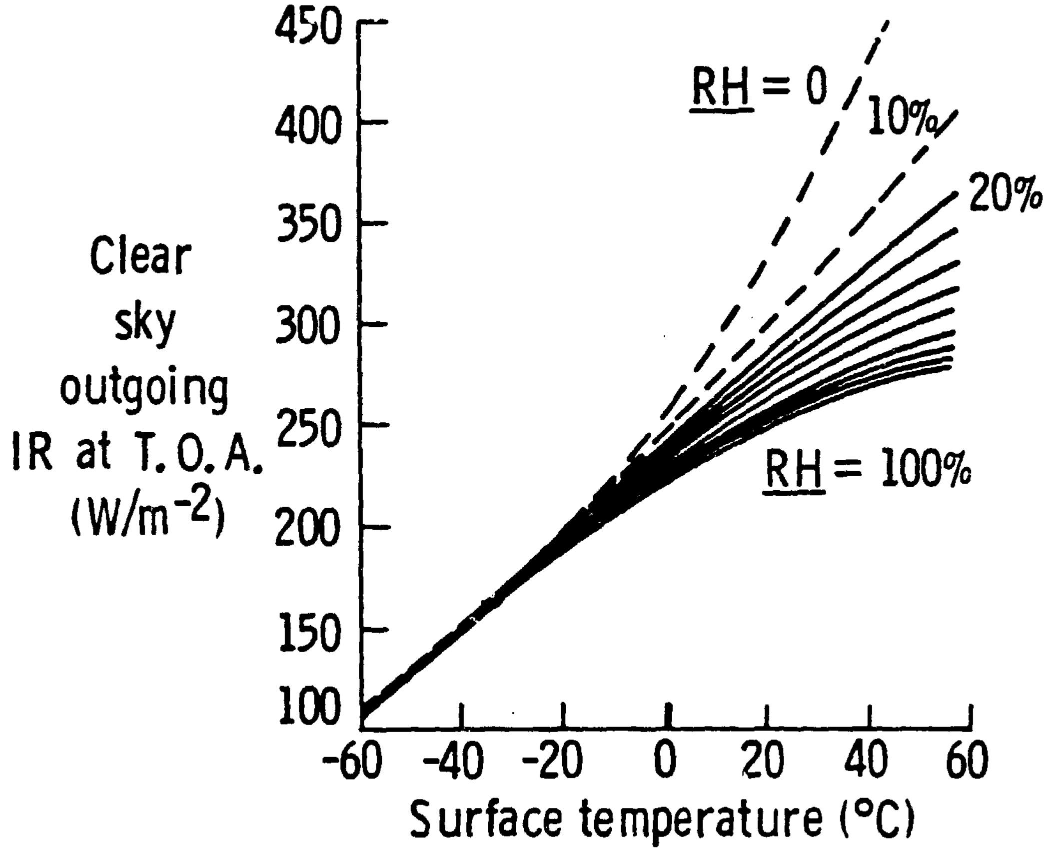

Figure 2.1 Family of curves depicting the parameterization of clear sky outgoing longwave irradiance as a function of T_s and RH.

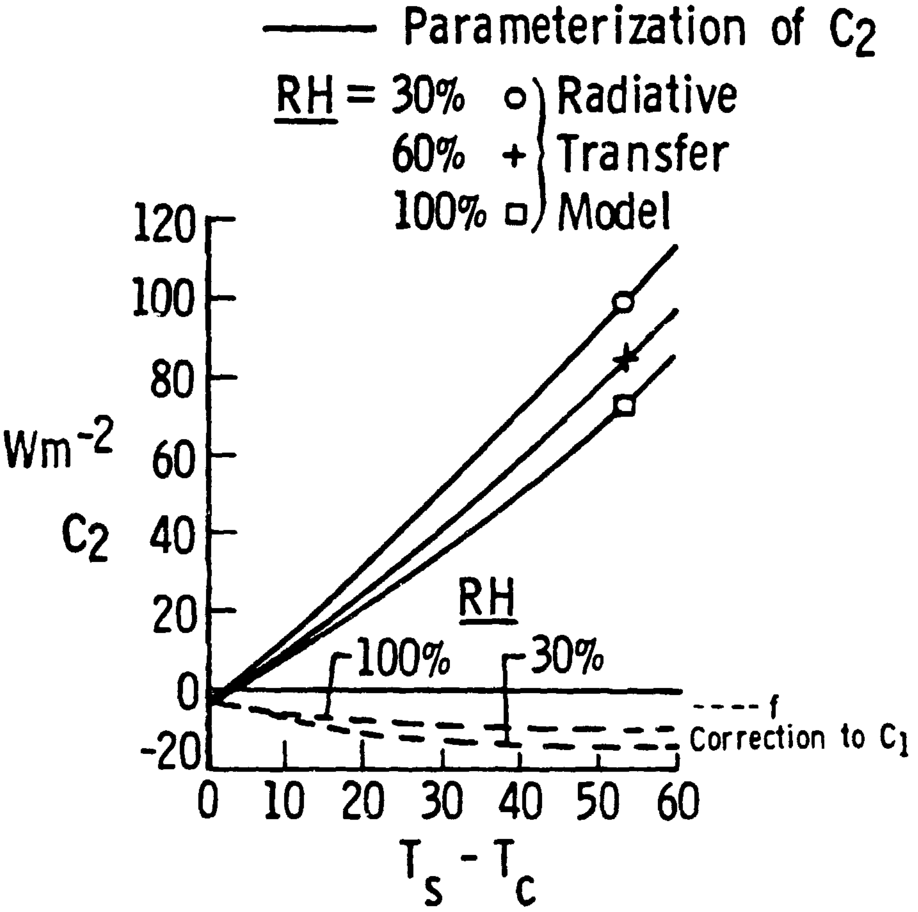

Figure 2.2 The cloud modification parameter C_2 as a function of T_s-T_c and RH for McClatchey et al. (1972) tropical temperature profile.

CHAPTER 3

DATA AND DATA MANAGEMENT

A climatological monthly mean data tape supplied by NCAR provides a great portion of the input data base for this study. In sec.3.1, we briefly discuss the content of the tape. In sec.3.2, the data averaging is mentioned.

3.1 Data

The data tape consists of two data files, one for each hemisphere. Both files have data on a 5^ox5^o horizontal grid system. Meteorological variables on the tape are: temperature, dew point, geopotential height, standard deviation of these parameters and geostrophic wind. On the surface, sea surface pressure replaces geopotential height. Dew points are only recorded from the surface through 500mb. Two different forms of data are provided, one is hand analyzed, and the other is smoothed data. The smoothed temperature, dew point and geopotential height are selected for this study for the reason that the climatic fields are smooth after long term averaging.

Crutcher and Meserve (1970) used the data gathered by the World Meteorological Organization (WMO) climate data program for the Northern Hemisphere. The period of surface data is from 1931 through 1960, and the period of upper air data covers the years from 1950 through 1964. However, many stations have much less data; some only have data 2 to 3 years. The data for the Southern Hemisphere were compiled by Taljaard, et al. (1969). Data sources are mostly from the WMO International Geophysical Year, Air Force Air Weather Service and historical data from various sources. Station density is less in the Southern Hemisphere due to more ocean coverage. Isopleths were subjectively drawn across void grid points, and therefore the reliability of each grid varies depending on the availability of data.

Data are also subject to instrumentation errors, which include bad calibration and different performance from different instrument manufacturers. In the troposphere, the standard deviation of temperature measurement from using different instruments is about .5°C, and in the stratosphere is about 2°C. Errors are also introduced in communication processes, such as radio noise, teletype errors and human error.

Computer routines were designed by Crutcher and Meserve (1970) and Jenne, et al. (1974) to eliminate the unreasonable data. All of the errors mentioned above are summarized in the variance analysis and tabulated as standard deviations for each parameter except geostrophic wind, which we did not use.

3 2 Data Averaging

A simple scheme is defined to merge the two files of the Northern Hemisphere and the Southern Hemisphere together, and to average the orginal 5°x5° grid system to 10°x10°. The reasons for using 10°x10°

grid system is that the cloud data are not available in more detail. Also, the Thompson and Warren (1982) parameterization is limited to coarse resolution application.

The new grid points are selected at latitude 85°N, 75°N,..., 75°S, 85°S on longitude 5°W, 15°W, ..., 355°W. Data from all nine grid points around each new grid point (see Fig 3.1) are included in the averaging process. However, near the poles, i.e. 85°N and 85°S, the original data at 90° are only counted once to avoid overweighting the repetition of same data at every longitude. This procedure also smooths the data slightly.

(a) (b)

Figure 3.1 Grid points for the new 10°x10° system relative to the NCAR 5°x5° system; (a) for ordinary latitude, (b) at the poles.

CHAPTER 4

WATER VAPOR AND CLEAR SKY OUTGOING LONGWAVE RADIATION

4.1 Introduction

As mentioned in Chapter 2, one of the parameters used in the longwave outgoing flux calculation is the average relative humidity, defined as:

$$\underline{RH} = \frac{1}{12\ \mathrm{km}} \int_0^{12\mathrm{km}} RH(z)\, dz \qquad 4.1$$

where the pressure at 12km height is about 190mb (U.S. Standard Atmosphere, 1976). To implement equation 4.1, one needs (1) sufficient water vapor data from the surface to 12km, (2) an algorithm to convert dew point or mixing ratio to relative humidity, and (3) an integration scheme. However, the observational data set described in Chapter 3 only provides dew point information from the surface to 500mb. This data between 500mb and 12km must be furnished through another source. To fulfill this, we adapt an empirical formula by Harries (1976), which describes the water vapor distribution at 100mb, and an interpolating scheme which incorporates the Harries empirical formula and the observational data to generate water vapor data at 200mb and 300mb.

In section 4.2, we will discuss the atmospheric water vapor. In section 4.3, the interpolation scheme will be discussed. In section 4.4, the method of converting dew point temperature and mixing ratio to relative humidity is discussed. Section 4.5 describes the integration of equation 4.1. In section 4.6, the world wide RH and clear sky outgoing longwave radiation are presented. In section 4.7, the sensitivities of the interpolation scheme and averaging scheme are discussed.

4.2 Atmospheric Water Vapor

Although it is not necessarily true that atmospheric water vapor, when expressed as relative humidity, decreases with altitude, it is well recognized that mixing ratio decreases rapidly with altitude (Smith, 1966) as it is an exponential function of temperature. Unable to cope with such a drastic change, the hygrometers used in conventional radiosondes generally lose their sensitivities as temperature goes below -40°C. Even under the warmest atmospheric conditions, radiosonde humidity observations seldom exceed an altitude of 10 km (U.S. Standard Atmosphere, 1976). London (1957) urged water vapor measurement in the upper troposphere for its importance to the radiation budget. Yet, Routhier and Davis (1980) analyzed the data collected from the Global Atmospheric Measurements Experiment of Tropospheric Aerosols and Gases, and suggested that some of the global climatological dew point data in the middle troposphere measured from the conventional method was too high due to such an instrumental limitation.

Meanwhile, several *in situ* stratospheric water vapor experiments with special instruments, which included part of the higher troposphere had been performed. The most well known are the long term series of the measurements conducted by Mastenbrook (1968). These measurements used balloon soundings with a frost-point hygrometer. The results showed that there is a seasonal variation in mixing ratio with the lowest mixing ratio in late winter and early spring and the highest in late summer and early fall. Also, the magnitude of the seasonal change decreases with height. He thus suggested that the temperature of the tropopause regulates the level of stratospheric moisture.

However, not all of the experiments agree well with each other. Figure 4.1, from a review of Harries (1976), shows results from the major measurements performed at different times, seasons, latitudes and with different instruments. By rejecting some of the conflicting data, he managed to formulate an equation governing the latitudinal variation at 100mb, but without the time variation:

$$Q_{100mb}(J) = 3 \times 10^{-6} \Big/ \left(1 + \frac{(J-20)^2}{128}\right) \qquad 4.2$$

where J is the index for latitude; 1, 2, 3, ..., 35 correspoing to -85°, -80°, ..., 85°. This equation was later implemented by Briegleb and Ramanathan (1982) for their clear sky albedo calculation.

A more recent review on stratospheric water vapor was done by Ellsasser (1983). He tried to interpret the tropospheric-stratospheric water vapor transfer mechanism with minimum rejection of

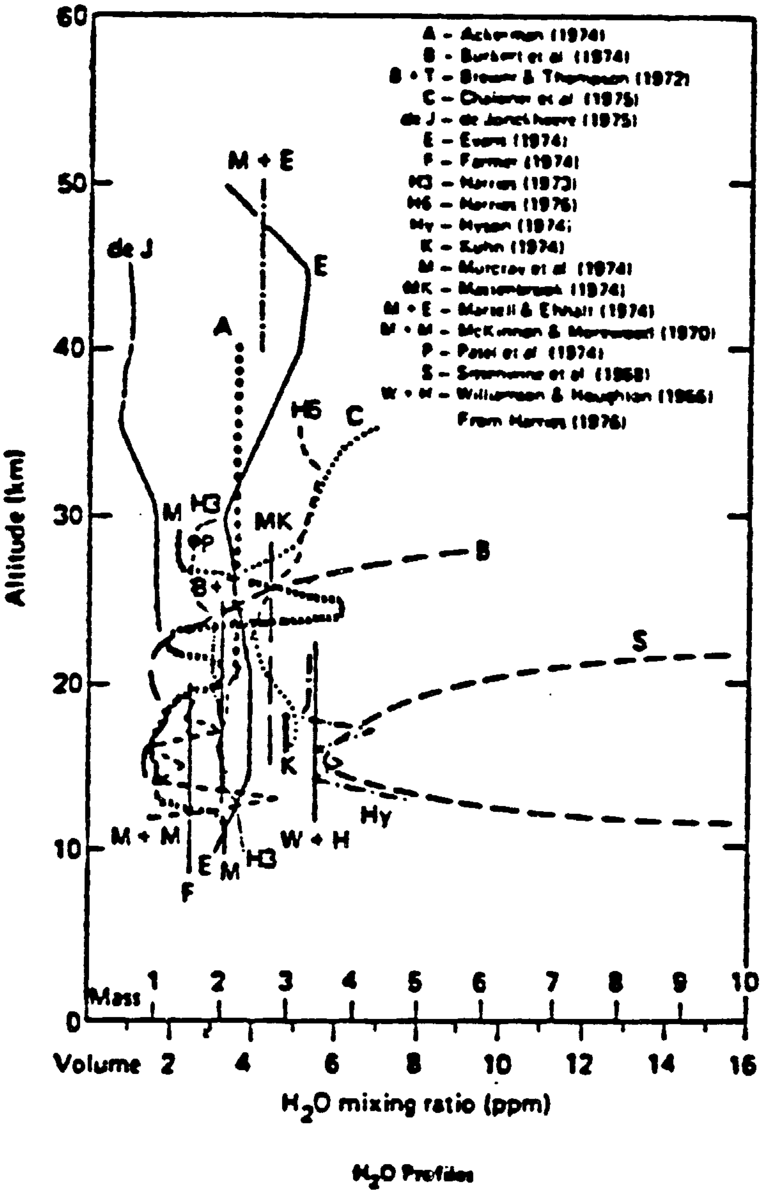

Figure 4.1 Summary of observations of vertical profiles of high altitude water vapor compiled by Harries (1976).

conflicting observational data. Basically, the stratospheric water vapor is flushed by air entering only through the tropical tropopause and leaving only through the polar tropopauses or tropopause gaps. There is also a possible chemical source, methane oxidation, which however, does not have significant effect.

In contrast to the in situ measurements, the recent LIMS Experiment on the Nimbus 7 satellite measured the water vapor distribution higher than 100mb. This experiment revealed very remarkable stratospheric water vapor information (Russell et al., 1984): there is a broad tropical minimum in mixing ratio, extending from 100mb to about 30mb as shown in Figure 4.2, which coincides with the "cold trap", the coldest temperature region in the stratosphere. The data also showed a poleward gradient at all levels up to 4mb. These results are very different from the perceptions of the previous investigations and might have very substantial implications for water vapor budget and stratospheric general circulation studies. In the process of the present study, this result was not available.

More than 25 years after London (1957), the climatological water vapor distribution between 500mb and 100mb over the globe is still unavailable except for some zonally averaged data for the Northern Hemisphere from London (1957) and from Oort and Rasmusson (1971). The latter raises some problem in converting mixing ratio to relative humidity, which will be discussed in section 4.4. Some data for the tropics from Newell, et al. (1972) are also available. Clearly, there is a demand for refining current sounding instruments in order that the measurement be operable under low water vapor pressure, low

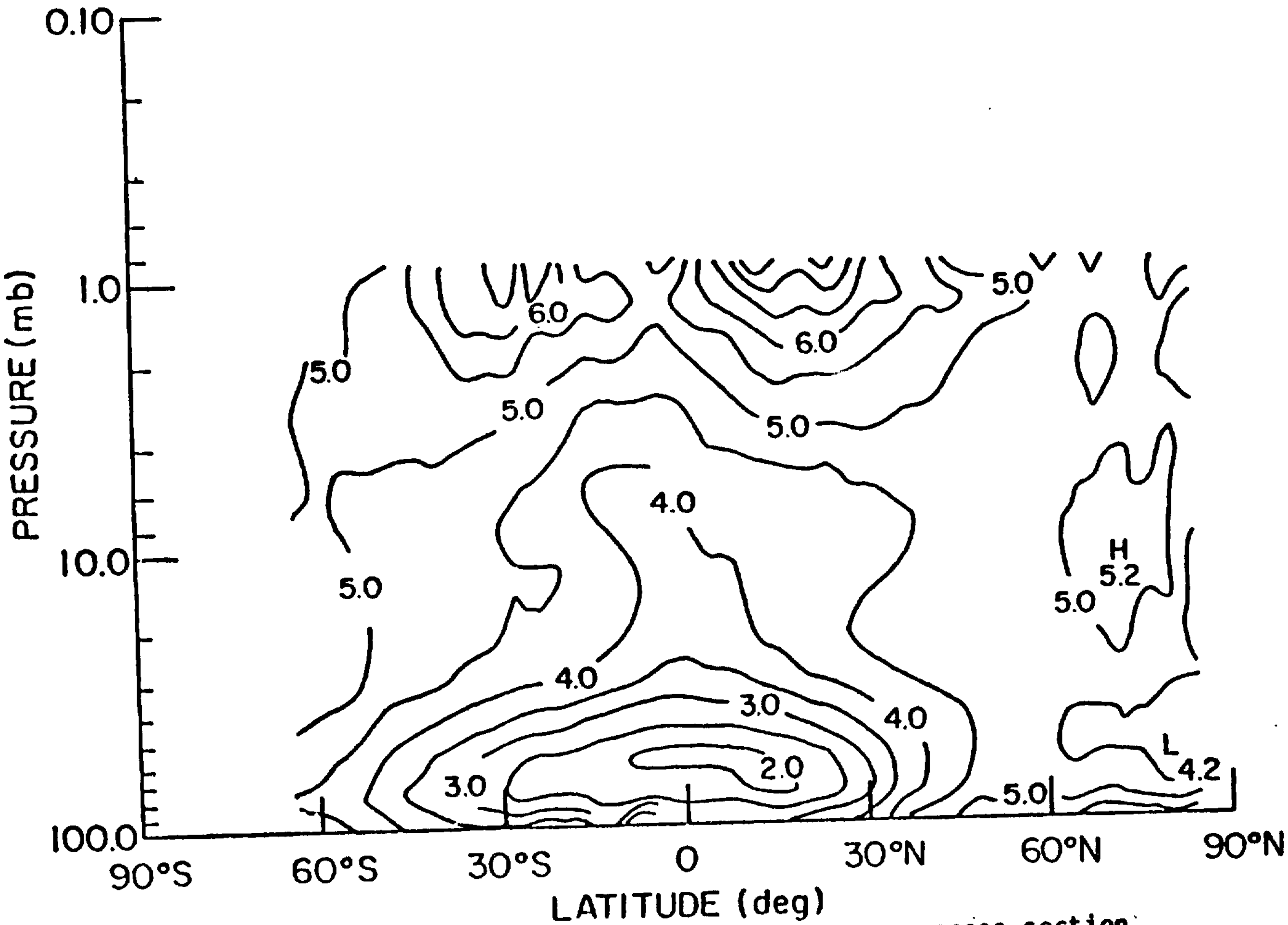

Figure 4.2 LIMS five day zonal mean water vapor cross-section for January 5-9, 1979 after Russell et al. (1984), in ppm.

pressure conditions, so that compiled climatologies such as Thompson and Warren's (1982) zonally averaged relative humidity or the results from complicated general circulation models, such as Sirutis, et al. (1980) can be verified.

4.3 Vertical Interpolation for 300mb and 200mb Specific Humidity from 500mb and 100mb

As mentioned in the section 4.1, we need to fill in water vapor data higher than 500mb in order to perform the vertical integration.

An interpolation method similar to that used by Briegleb and Ramanathan (1982) is adapted for this purpose. This method incorporates Harries (1976) empirical formula for 100mb water vapor, equation 4.2, and the NCAR data base described in Chapter 3 as boundary conditions. It will be shown in section 4.7 that the error of the final longwave flux calculation due to this interpolation is minimal.

Briegleb and Ramanathan studied the radiosonde measurements from Rogers and Walshaw (1966) and found that the variation of the logarithm specific humidity ln(Q) with pressure P from 500mb to 100mb has a quadratic relationship as $\ln(Q) \sim p^2$. Thus, if the data of these two layers are available, the data of intermediate layers can be obtained through interpolation. A special interpolation function with a single parameter is selected such that only upper and lower boundary conditions are needed, compared to polynomial interpolation which generally needs more than three data points specified. The interpolation formula is

$$\ln Q(P) = \frac{n}{2}(\ln Q_{100mb} + \ln Q_{500mb}) + (\ln Q_{500mb} - \ln Q_{100mb})(\frac{P-300}{400}) + 4(1-n)(\frac{\ln Q_{100mb} + \ln Q_{500mb}}{2})(\frac{P-300}{400})^2 \qquad 4.3$$

where subscripts indicate pressure levels and n is an interpolation factor. When n=1, this is a linear interpolation and when n is adjusted to be less than 1, Q can be fitted to the quadratic curves required for climatological specific humidity, see Figure 4.3.

In order that the zonal average Q's of 300mb vary the same way as the observations of Oort and Rasmusson (1971), and for the reason that Q varies from the tropics to the poles only by a factor of 3 at the 100mb pressure level, while at the 500mb pressure level it varies by a factor of 10 (Briegleb and Ramanathan 1982), n must be latitudinally dependent so that there is more linear interpolation in the poles and more quadratic interpolation in the tropics. Both can be accomplished by letting n, in equation 4.3, vary as a function of latitude as:

$$n(j) = 0.86\ [1 + \frac{(J-19)^2}{1500}] \qquad 4.4$$

where j is the index of latitude, 1,2,3,... referring to latitudes -87.5°, -82.5°, ..., 87.5°, respectively.

To restrict overestimation when compared to the climatology of Rogers and Walshaw (1966) another constraint needs to be applied: when equation 4.4 gives $n(j) > .92$, it is set to .92.

Using this method to calculate relative humidity will result in

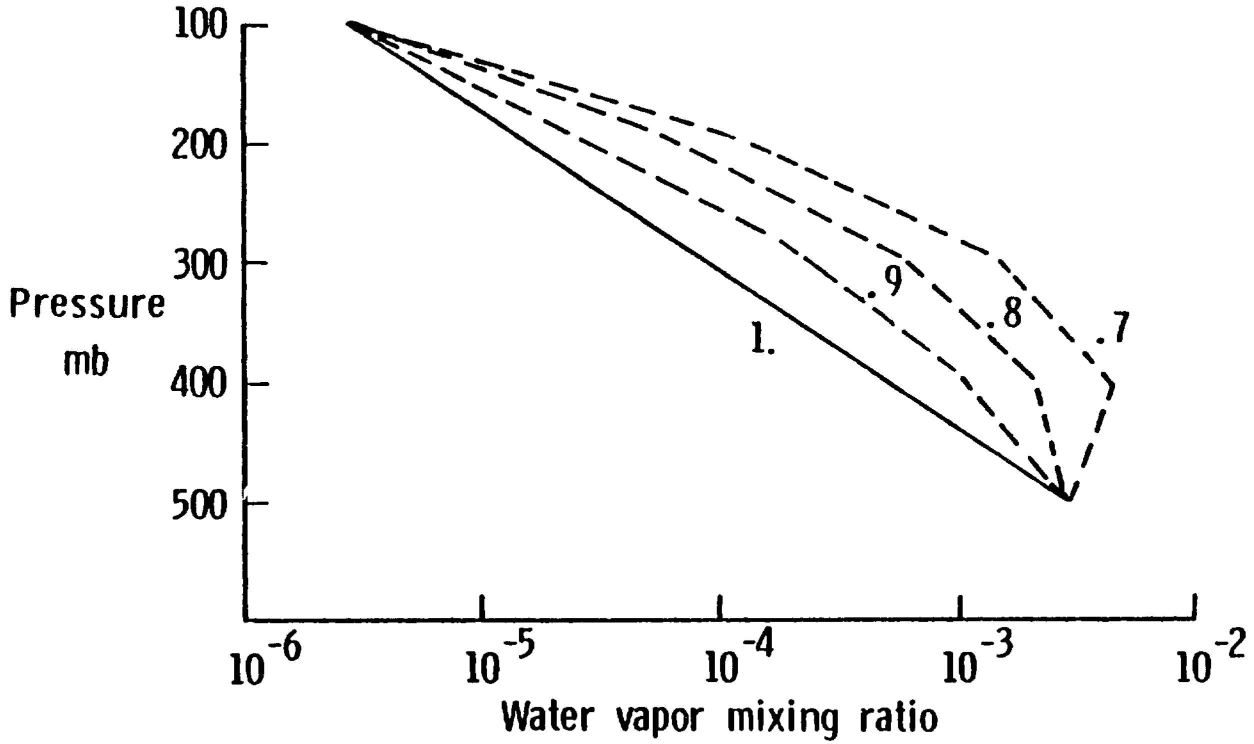

Figure 4.3 Characteristics of the interpolation function equation 4.3 for different values of parameter n.

a few points with a value higher than 100% at 300mb and 200mb. For those cases, the value is set equal to 100%. This is not unexpected for coupling two different data sets together. Even using matched zonal average specific humidity and temperature, such as Oort and Rasmusson (1971), will yield RH higher than 100%. The reason for this will be discussed in the latter part of the next section.

4.4 Relative Humidity Calculations from Dew Point Temperature and Mixing Ratio

When dew point temperature (T_d) or mixing ratio (W) are available either from measurements or from interpolation as generated from the method described in the previous section, one must convert them to relative humidity (RH). The definition of RH according to List (1959) is

$$RH=W/W_s \qquad 4.5$$

where the subscript s denotes saturation and W is defined as

$$W=.622\ e/(p-e) \qquad 4.6$$

where e is water vapor pressure. Equation 4.6 can be written as

$$RH=(e/e_s)(p-e_s/p-e) \qquad 4.7$$

The second parentheses on the right hand side approximates to unity, so that Thompson and Warren (1982) simplified the definition to

$$RH=\begin{matrix} e/e_{sw} & t > 0^oC \\ e/e_{si} & t < 0^oC \end{matrix} \qquad 4.8$$

where e_{sw} is the saturation water vapor pressure over water, and e_{si} is the saturation water vapor pressure over ice. There are many methods available for calculation of e_{sw} and e_{si}. One can use the integrated form of the Clausius-Clapeyron equation, the equations by List (1959), Richard (1971) or Parish and Putnum (1974). The latter three are empirical equations which fit the observed water vapor pressure; any one of them can give slightly better results than the standard Clausius-Clapeyron equation in some narrower specific temperature range. In this study, we follow Thompson and Warren (1982) using Richards (1971) for e_{sw}:

$$e_{sw} = 1013.25\ \mathrm{EXP}(13.3185t-1.9760t^2-0.6445t^3-0.1299t^4) \qquad 4.9$$

where $t=1-373.15\ T^{-1}$ and T is the temperature in Kelvin.

Using List (1959) for e_{si}:

$$\begin{aligned}\mathrm{Log}_{10}\ e_{si} &= -9.09718(x-1)-3.56654\ \mathrm{Log}_{10}x+0.876793(1-x^{-1})\\ &\quad +\mathrm{Log}_{10}6.1071\end{aligned} \qquad 4.10$$

where $x=273.16\ T^{-1}$.

By definition $W=e/(p-e)$, and $Q=e/p$. Because e is much smaller than P, W approximates Q through the meteorological range. In calculating relative humidity at the 300mb to 100mb levels, W is considered to be equal to Q, which is calculated by the interpolation scheme of the section 4.3. Also the corresponding W_s must be calculated and transformed to e_s. From the surface to the 500mb level, e and e_s are calculated from dew point and temperature.

One caution should be taken in selecting the phase change temperature. Thompson and Warren arbitrarily selected 0°C in their study. In the atmosphere, it is very common that water vapor exists in supercooled form. As pointed out by List (1959), water vapor can exist in the air temperature below 0^oC as supercooled; however, hygrometers which essentially only respond to water vapor indicate relative humidity with respect to water vapor only, regardless of the temperature. Thus, in relative humidity calculations, improper selection of the phase change temperature would significantly introduce error when comparing water vapor pressure to saturation vapor pressure of the wrong water phase. To alleviate this error, one should select a phase change temperature below 0^oC, such as London (1957) did.

Another significant problem in converting climatological specific humidity or mixing ratio to relative humidity is that relative humidity is often overestimated. The error is not directly from the converting scheme, but from the time or space averaging scheme for the climatology. This can be clearly illustrated by the following example in averaging two cases.

Case I. temperature 273^oK, relative humidity 90%, e=5.50mb.

Case II. temperature 279^oK, relative humidity 84%, e=7.85mb.

So the averaged temperature is 276^oK and the averaged e=6.67mb. The e_s of the averaged temperature 276^oK is 7.56mb. If one uses averaged e and the e_s based on averaged temperature to calculate relative humidity, the result would be 88.2%. However, if one just averages the relative humidities, the result would be 87%. A 1.2% difference is created. As the sample's deviation increases, the result would get worse. This is simply caused by the fact that e_s is an exponential function of temperature which is concave upward, as shown in

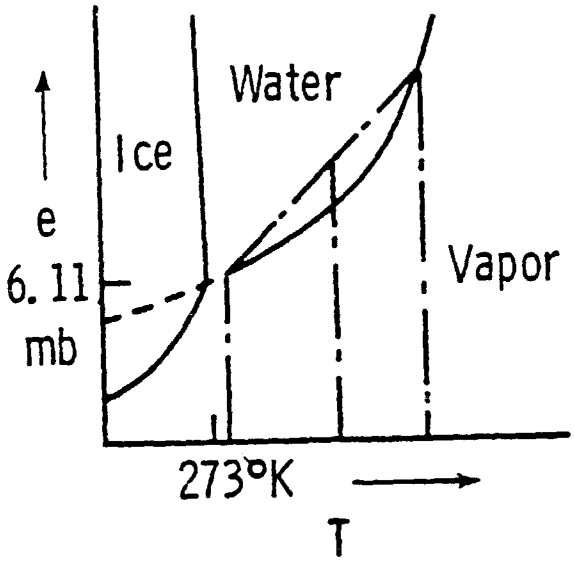

Figure 4.4 Temperature and vapor pressure phase diagram for water substance. The dash-dot line illustrates the example in section 4.4.

Figure 4.4. The water vapor pressure is not supposed to be linearly averaged as temperature. Thus when one uses specific humidity and temperature for temporal and space averaged climatological data as Oort and Rasmusson (1971) and converts them to relative humidity, the result is overestimated. In many cases of this data set, the results are higher than 100%, (see Table 4.1). On the other hand, if one uses averaged dew point temperature to calculate relative humidity, then it would be underestimated.

There is no straightforward remedy for this problem unless one has sample relative humidity data to start with and directly averages over relative humidity.

4.5 Vertical Integration of relative humidity

To perform the vertical integration, equation 4.1 is changed to numerical form as

$$\underline{RH} = 1/12\text{km} \quad \sum (RH_i + RH_{i+1})(gph_{i+1} - gph_i)/2 \qquad 4.11$$

where gph is geopotential height, subscript i is the index of each pressure level from 1 to 6 as surface, 850mb, 700mb, ..., 200mb.

As mentioned earlier, pressure level 200mb is located around 12km geopotential height, depending on the location. Since equation 4.1 is an integration function with upper bound at 12km, we replace the relative humidity at 200mb by relative humidity at 12km. These values are obtained by linear interpolation along the geopotential height between 300mb and 200mb or 200mb and 100mb, depending on where the geopotential height of 200mb is located.

Table 4.1 Relative humidity derived from the climatology of Oort & Rasmusson (1971) for January, in %.

100	0	0	0	0	0	0	0	0	0	0	0	0	0	0	0	0	0
200	0	0	0	0	0	0	0	0	0	0	0	0	0	0	0	0	0
300	46	45	31	32	17	20	25	39	65	100	130	160	184	215	235	0	0
400	48	43	35	28	25	24	32	49	60	62	85	109	134	156	184	218	252
500	47	38	30	25	27	32	41	48	60	60	66	85	79	95	75	90	107
700	56	56	49	38	33	33	36	42	49	59	70	77	77	83	86	88	88
850	75	73	67	61	67	56	56	57	65	76	84	93	99	99	105	105	97
900 mb	82	82	74	66	63	61	61	68	74	82	93	98	100	106	111	119	114
950 mb	82	81	77	72	68	66	68	71	79	88	101	106	111	121	131	135	137
1000 mb	78	79	78	75	73	71	72	74	79	89	99	106	112	132	140	160	153
Latitude	-55	0	5	10	15	20	25	30	35	40	45	50	55	60	65	70	75°N

4.6 RH and Clear Sky Outgoing Longwave Radiation Fields

4.6.1 Zonally Averaged RH field

First, the zonally averaged RH of January and July calculated from this scheme are compared with the climatology compiled by Thompson and Warren (1982), whose data are from London (1957) for 7~ 22km, 0 ~ 75°N; Oort and Rasmusson (1971, hereafter denoted as OR) for 0 ~ 7km, 10°S 75°N and from Sasamori, et al. (1972) for 0 ~ 22km, 10 ~ 90°S.

Figures 4.5 and 4.6 show the comparison of the averaged RH of January and July respectively. It is clear that both cases have good agreement in low and mid-latitudes with a maximum at the tropics which coincides with the ITCZ, and minima at the subtropics which coincides with the descending arm of the Hadley cell. The seasonal variations of the pattern are also in phase with the position of the sun. Significant differences occur at the high latitudes, where the polar descending flow would result in lower RH; the winter polar region is overestimated while the summer polar region is underestimated. A possible explanation of this difference for the Northern Hemisphere is that London (1957) only provided RH data up to the tropopause, so that the upper level data are unavailable in these regions and in the high latitude the tropopause is lower than 12km. Therefore in January, Thompson and Warren's (TW) calculation does not have relative humidity input between the tropopause and 12km in the high latitude region. As the result, their RH values at these regions are lower. However, in the July case the mixing ratio of the lower atmosphere in the Northern Hemisphere is much higher than that

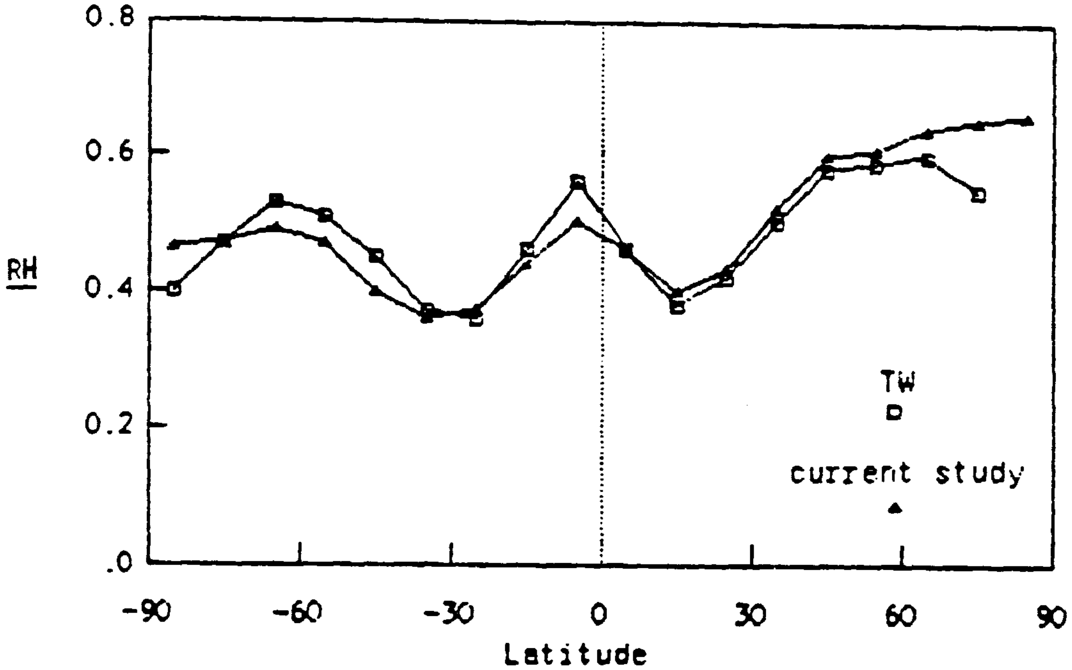

Figure 4.5 Zonally averaged RH for January.

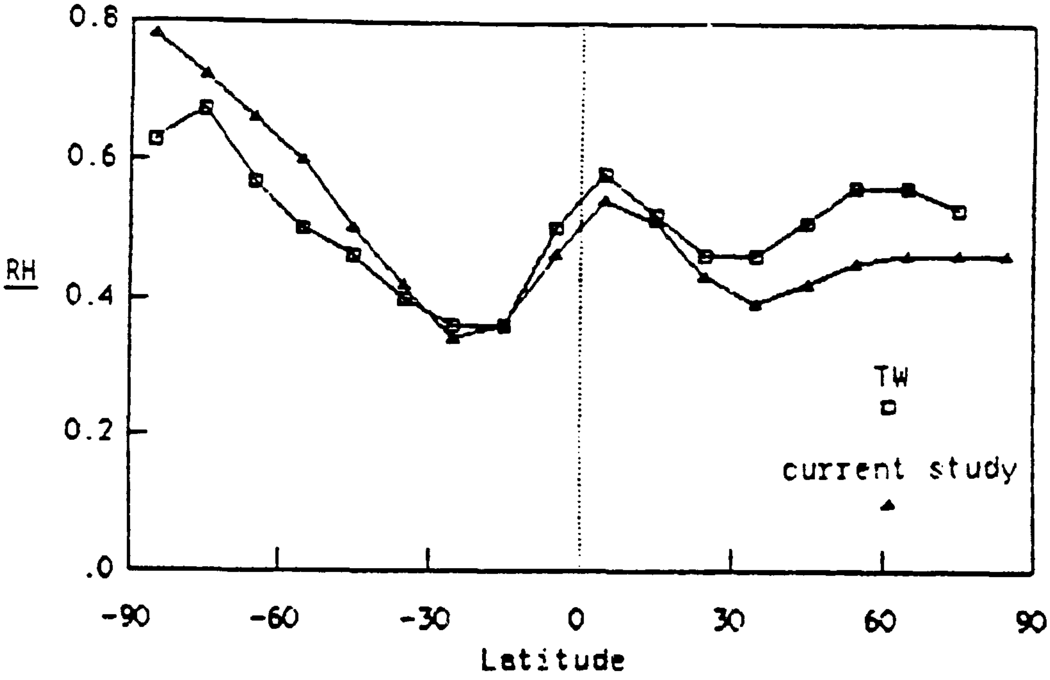

Figure 4.6 Zonally averaged RH for July.

Table 4.2 Comparison of mixing ratio between (1) Oort & Rasmusson (1971) and (2) drived from current work; the upper number in each box is from (1) and the lower number is from (2) except those of 1000mb is from (1) and those of surface is from (2).

	-15	-5	5°	15°	25°	35°	45°	55°	65°	75°	85°
100	.26E-5	.29E-5	.30E-5	.29E-5	.27E-5	.24E-5	.21E-5	.18E-5	.15E-5	.12E-5	.10E-5
200	.33E-4	.39E-4	.39E-4	.35E-4	.29E-4	.22E-4	.16E-4	.11E-4	.91E-5	.75E-5	.63E-5
300	.23E-3	.3E-3 .28E-3	.2E-3 .26E-3	.1E-3 .22E-3	.1E-3 .17E-3	.1E-3 .12E-3	.1E-3 .72E-4	.1E-3 .45E-4	.1E-3 .36E-4	0 .29E-4	.25E-4
500	.16E-2	.24E-2 .19E-2	-18E-2 .16E-2	.11E-2 .11E-2	.9E-3 .80E-3	.6E-3 .52E-3	.4E-3 .32E-3	.3E-3 .20E-3	.2E-3 .15E-3	.2E-3 .11E-3	.91E-4
700	.52E-2	.60E-2 .58E-2	.53E-2 .49E-2	.34E-2 .35E-2	.25E-2 .25E-2	.18E-2 .15E-2	1.3E-3 .99E-3	.9E-3 .64E-3	.7E-3 .47E-3	-5E-3 .32E-3	.23E-3
850	.98E-2	.11E-1 .11E-1	.10E-1 .98E-2	.77E-2 .74E-2	.51E-2 .51E-2	.35E-2 .33E-2	.23E-2 .20E-2	.16E-2 .12E-2	1.1E-3 .77E-3	.7E-3 .47E-3	.31E-3
1000 mb		.17E-1	.17E-1	.14E-1	.92E-2	.62E-2	.38E-2	.23E-2	1.2E-3	.6E-3	
Surface	.16E-1	.17E-1	.16E-1	.13E-1	.89E-2	.55E-2	.31E-2	.17E-2	.80E-3	.39E-3	.16E-3

Table 4.3 As Table 4.2 but for July.

	-15	-5°	5°	15°	25°	35°	45°	55°	65°	75°	85°
100 mb	.26E-5	.29E-5	.30E-5	.29E-5	.27E-5	.24E-5	.21E-5	.18E-5	.15E-5	.12E-5	.10E-5
200	.29E-4	.37E-4	.41E-4	.40E-4	.34E-4	.27E-4	.21E-4	.15E-4	.13E-4	.11E-4	.96E-5
300	.17E-3	.2E-3 .24E-3	.3E-3 .29E-3	.3E-3 .29E-3	.3E-3 .24E-3	.3E-3 .18E-3	.2E-3 .13E-3	.2E-3 .88E-4	.2E-3 .73E-4	.2E-3 .59E-4	.51E-4
500	.83E-3	.17E-2 .15E-2	.23E-2 .21E-2	.23-2 .22E-2	.21E-2 .19E-2	.18E-2 .17E-2	.14E-2 .11E-2	1.1E-3 .88E-3	.9E-3 .69E-3	.7E-3 .53E-3	.45E-3
700	.32E-2	.54E-2 .49E-2	.63E-2 .61E-2	.58E-2 .50E-2	.54E-2 .51E-2	.50E-2 .44E-2	.40E-2 .38E-2	.34E-2 .32E-2	.28E-2 .24E-2	.22E-2 .18E-2	.15E-2
850	.71E-2	.98E-2 .93E-2	.11E-1 .11E-1	.11E-1 .11E-1	.96E-2 .92E-2	.81E-2 .77E-2	.68E-2 .65E-2	.58E-2 .55E-2	.46E-2 .44E-2	.36E-2 .34E-2	.29E-2
1000 mb		.14E-1	.15E-1	.15E-1	.15E-1	.13E-1	.95E-2	.75E-2	.63E-2	.49E-2	
SFC	.12E-1	.16E-1	.17E-1	.17E-1	.15E-1	.12E-1	.94E-2	.80E-2	.63E-2	.47E-2	.36E-2

of OR. Generally speaking the OR mixing ratio is higher than the the mixing ratio derived from the data used in this study for both months (see Tables 4.2 & 4.3). This contributes to higher relative humidity, especially when compared with dew point derived relative humidity as this study has done. Another source of error is that Harries equation 4.2 does not account for seasonal variations.

Fortunately, outgoing longwave radiation is less sensitive to averaged relative humidity when the surface temperature is lower, see Figure 2.1. In other words, the polar regions can tolerate more averaged RH error than the tropics. Take the worst case, in July at 65°N, where the surface temperature is 12°C. If one varies relative humidity from 45% to 55%, clear sky outgoing longwave radiation only changes by about 5 W/m^2. Under cloudy sky conditions the error would be smaller.

4.6.2 Zonally Averaged Clear Sky Outgoing Longwave Radiation

In figures 4.7 and 4.8, the zonally averaged clear sky outgoing longwave (LW) radiation is compared with the calculation by Warren and Thompson (1983) for January and July. The excellent agreement between these calculations is obvious. The differences for most latitudes are smaller than $3W/m^2$. The zonally averaged surface temperature is also plotted on the same figures so that the relation between surface temperature and outgoing LW can be easily seen. Outgoing LW radiation versus RH is plotted in Figures 4.19 through 4.21 for the July case. In mid and low latitudes where the surface temperature is high, it is very evident that the outgoing LW is

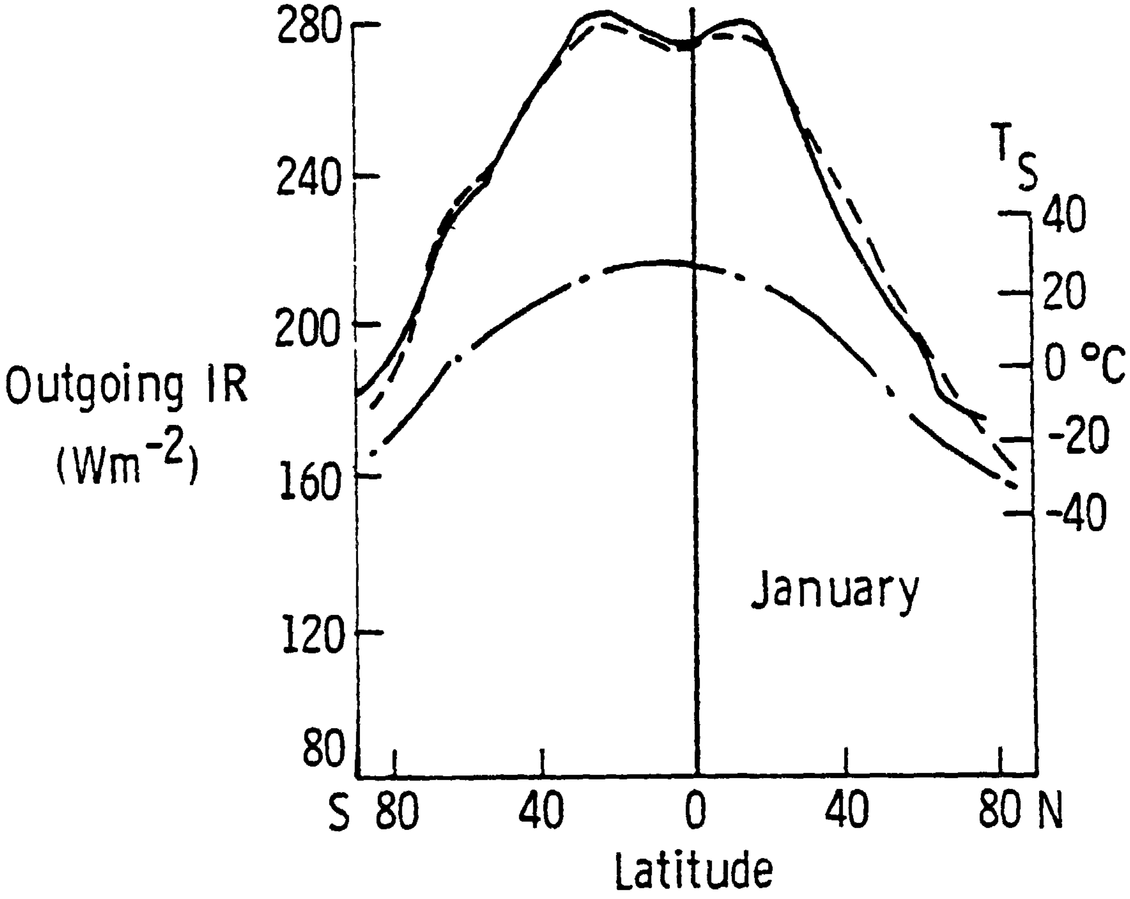

Figure 4.7 Zonally averaged clear sky OLWR and T_s for January. The solid line is calculated from current study; dash line is from TW and dash-dot line is T_s.

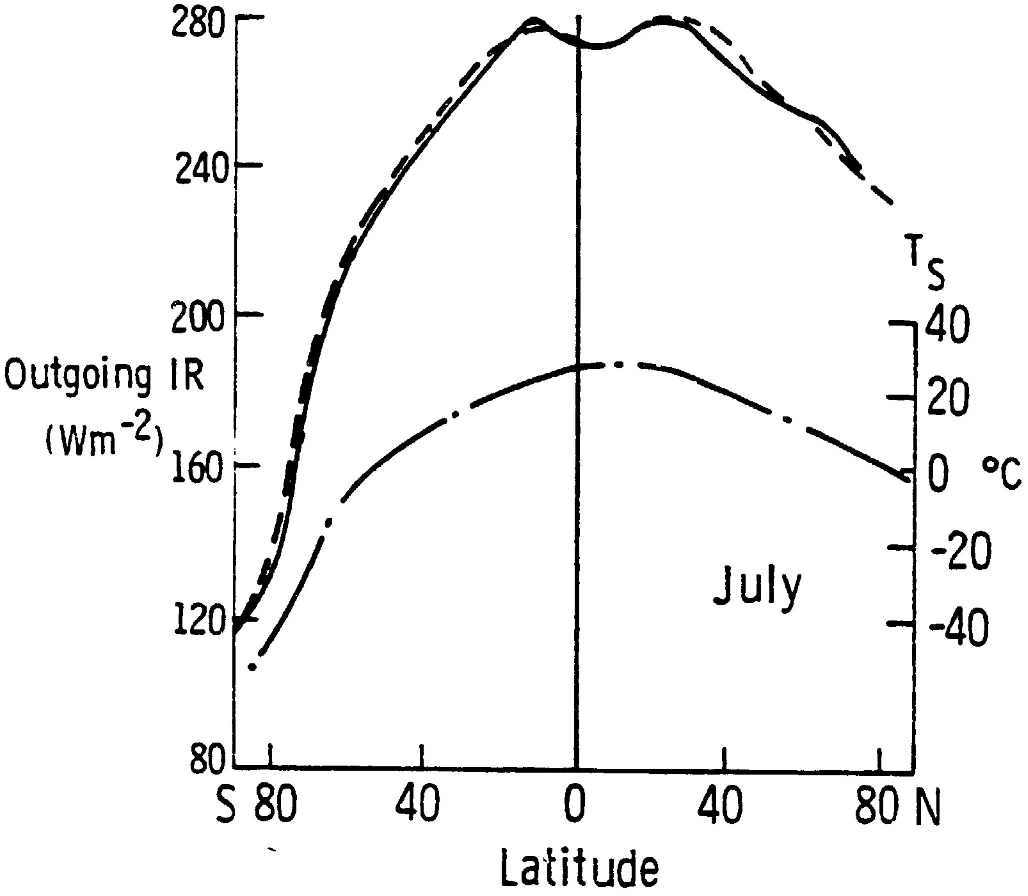

Figure 4.8 same as figure 4.7 but for July.

anticorrelated with $\underline{RH}$. At high latitude, where the surface temperature is low, outgoing LW is insensitive to averaged $\underline{RH}$ but is nearly linear with the surface temperature as discussed in the previous section.

4.6.3 Global $\underline{RH}$ Distribution

The world wide $\underline{RH}$ distributions are plotted in Figures 4.9 and 4.10 for January and July respectively. Compared with temperature contours in Figures 4.11 and 4.12, the $\underline{RH}$ contours have much higher longitudinal variations. Still, for both months the subtropical subsidences, the so called dry tongue of the Hadley cell, can be easily identified with low $\underline{RH}$ centers, as well as the high $\underline{RH}$ centers along the tropics with the Congo, Indonesia and the Amazon being the most prominent three regions. In January over the ocean, there are high $\underline{RH}$ centers on the east sides of the Pacific and the Atlantic which result from the cold temperature of the California and Canaries currents. The low $\underline{RH}$ center at the northeastern Pacific is possibly due to the warm surface temperature brought by the northern bound Kuroshio current. Over the continents, the cold temperatures at Siberia and Greenland also contribute to high $\underline{RH}$ as the water vapor in the air is conserved.

In July, the averaged $\underline{RH}$ center along the subtropic subsidence belt of the Southern Hemisphere remains fairly well defined as in the January case. However, the low averaged $\underline{RH}$ center in Australia is more clear for the reason that in the Southern Hemisphere winter land-ocean temperature differences are more pronounced. The high

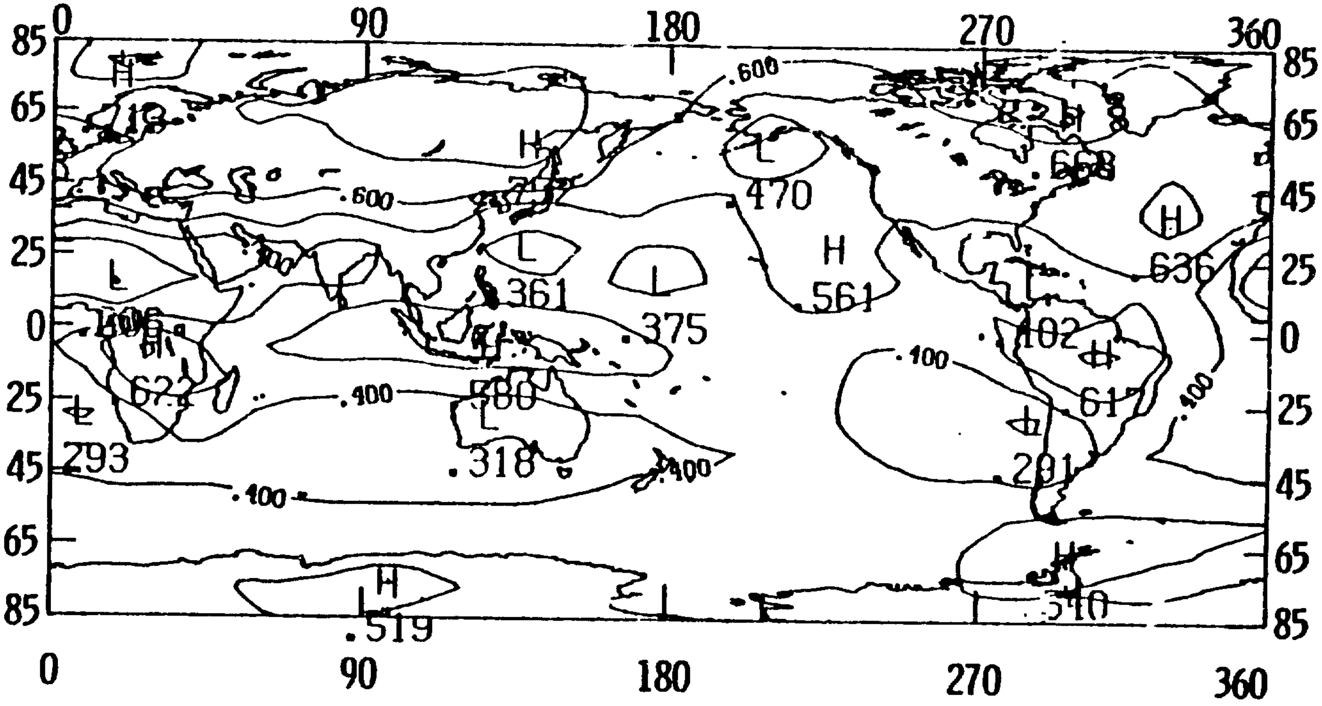

Figure 4.9 RH map for January.

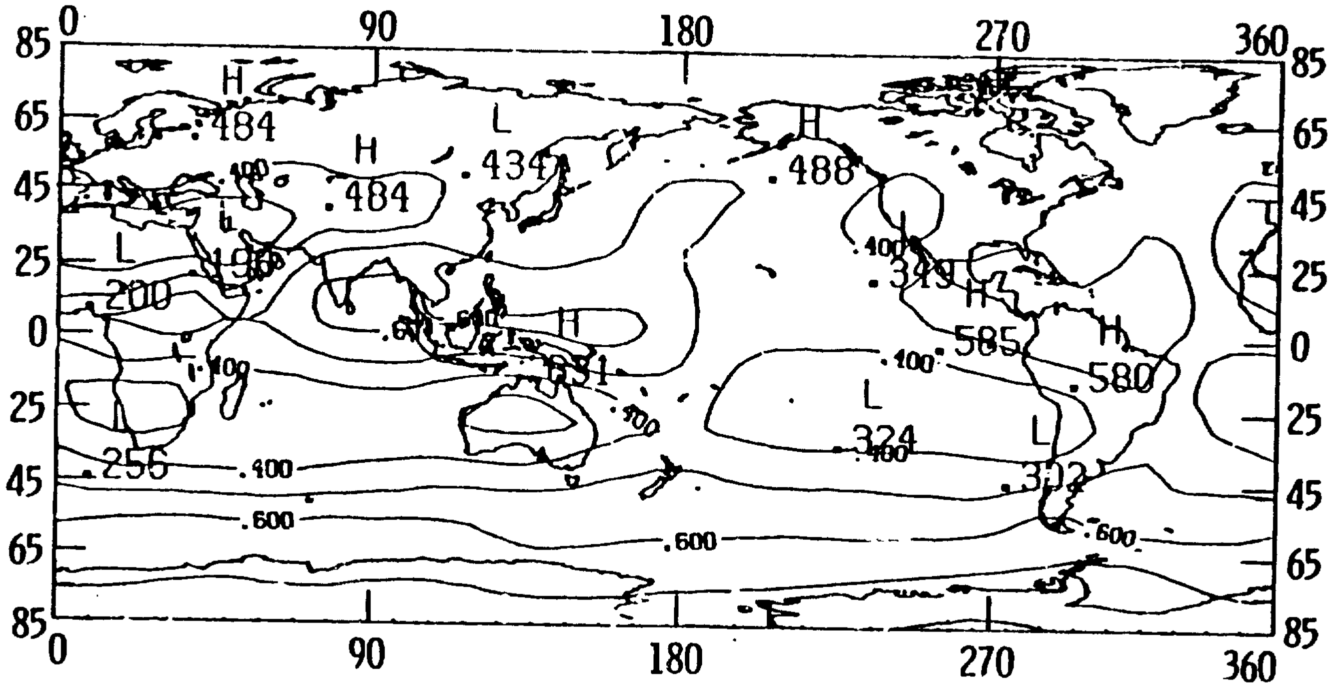

Figure 4.10 RH map for July.

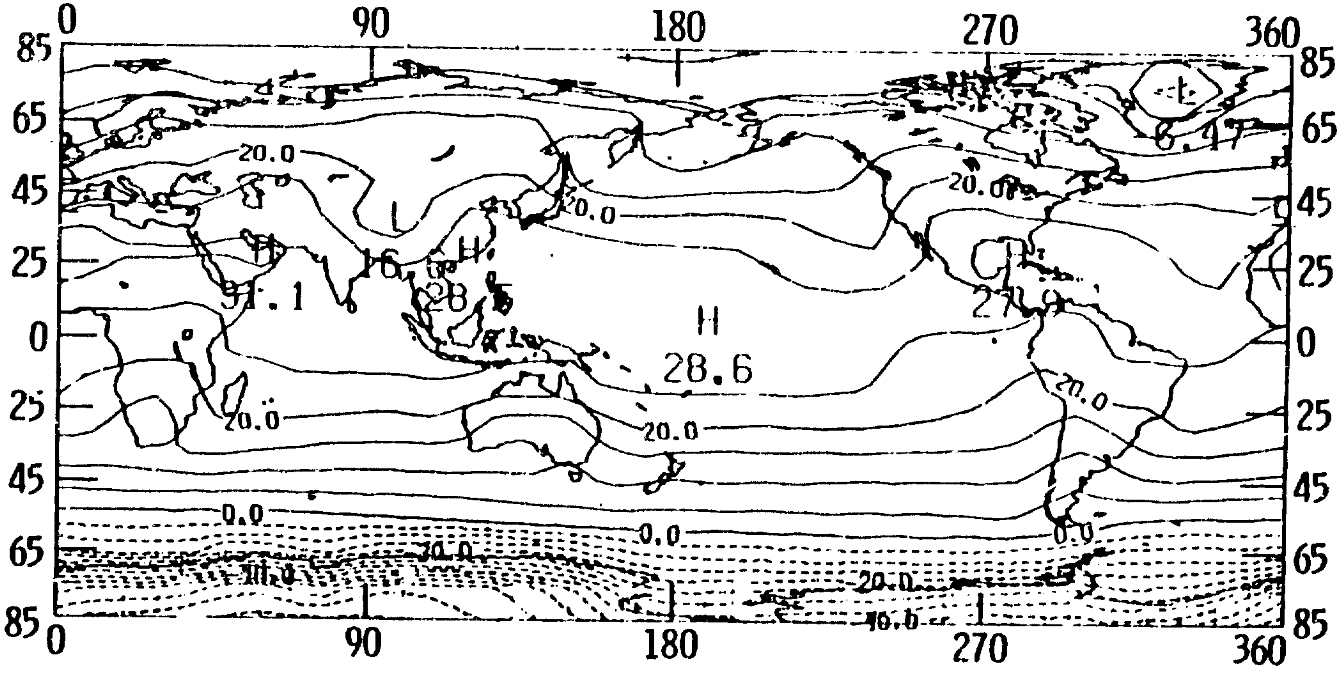

Figure 4.11 Climatological T_s map for July, in °C.

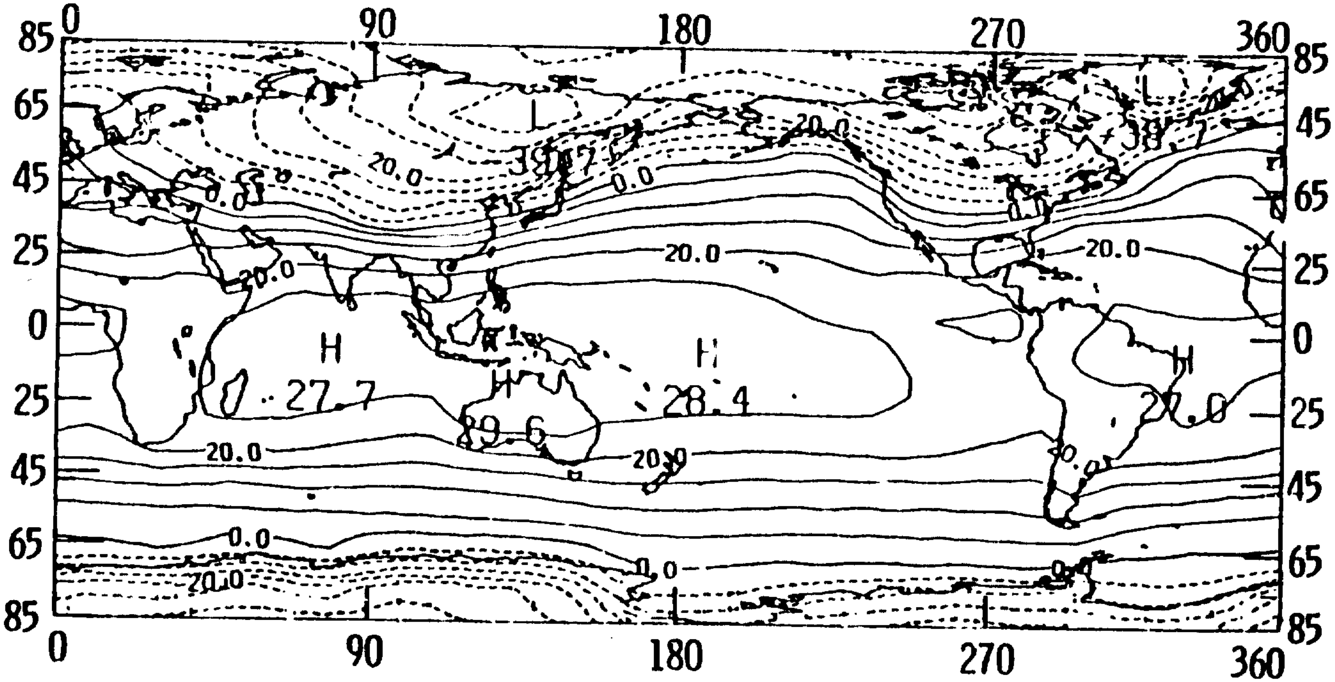

Figure 4.12 Climatological T_s map for January, in °C.

averaged RH centers along the intertropical convergence zone (ITCZ) all move northward. The region over the Amazon extends over the Caribbean sea. The low RH over the Sahara desert intensifies to cover the Middle East. The high RH center over Tibet and Central Asia weakens from a winter value of about 60% to 48% due to increasing air temperature and lack of influx of water vapor. The same applies to Siberia.

4.6.4 Global Clear Sky Outgoing Longwave Radiation Distribution

Figures 4.13 and 4.14 show the January and July clear sky outgoing longwave radiation field. It is easily seen that the winter hemisphere has a higher latitudinal LW radiation gradient than the summer hemisphere. The influence of the continents and of the ocean currents along the coasts can be easily identified. The highly longitudinal variations in the subtropics and tropics are remarkable. In this region, high LW centers are located in the central Pacific, Australia, and the southern Indian Ocean; and the low LW centers are located in Indonesia, the Congo and the Amazon, which coincides with the high averaged RH centers at those regions. These three centers move north-south according to the sun's position as well as change their intensity. Generally speaking, the high LW centers are located in the subtropics and low LW centers are located in the tropics. This agrees with the zonally averaged results discussed by Warren and Thompson (1983).

An important feature of Figures 4.13 and 4.14, which cannot be seen in the zonally averaged plots is that along the tropics the

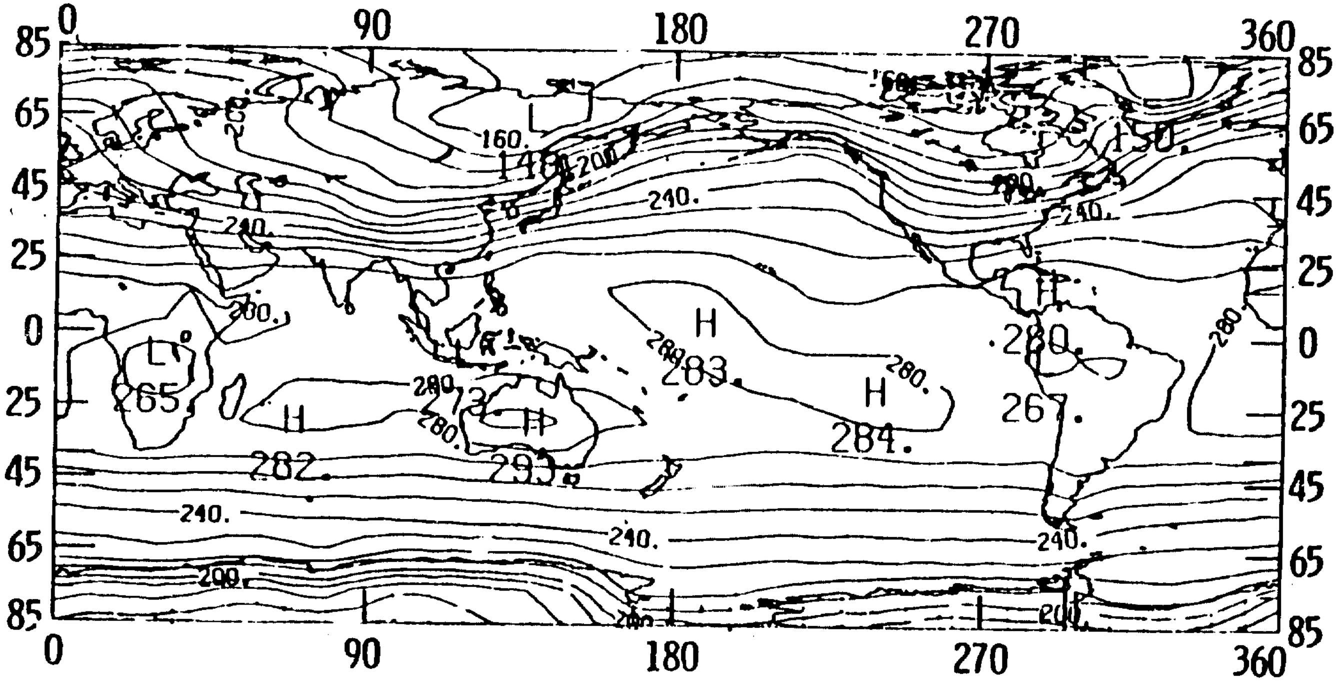

Figure 4.13 Clear sky OLWR map for January, in W/m^2.

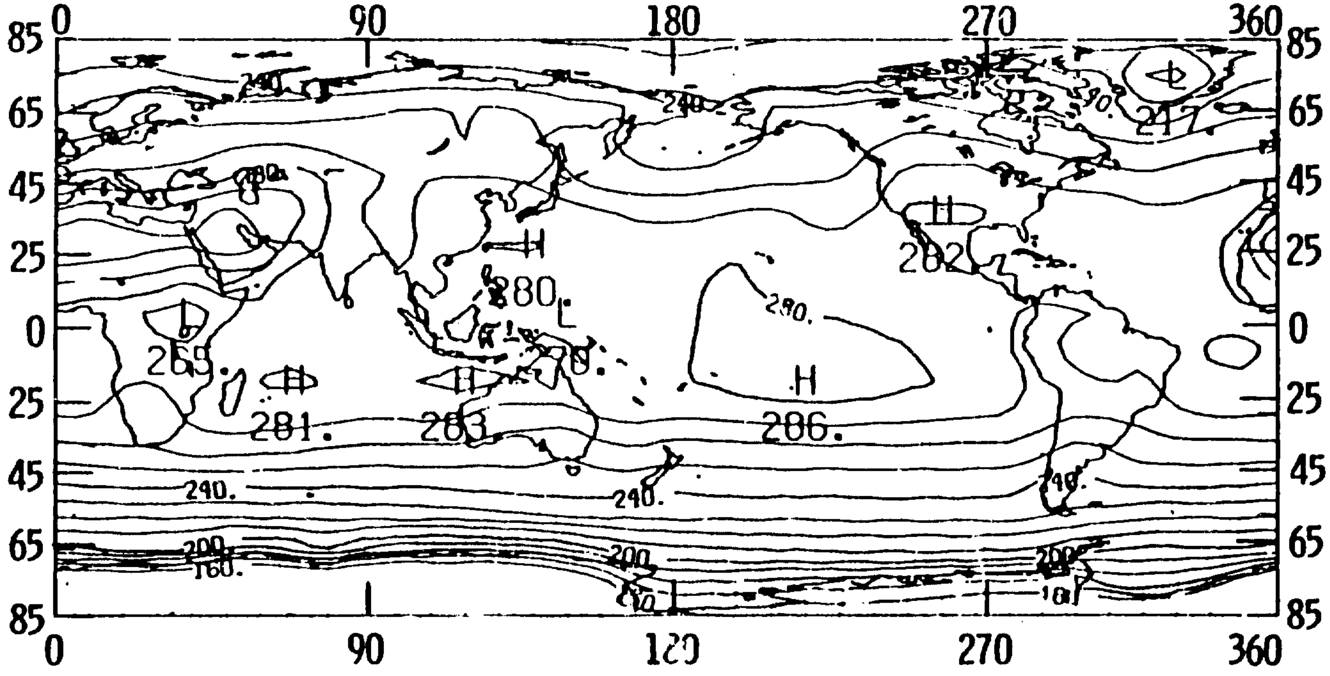

Figure 4.14 Clear sky OLWR map for July, in W/m^2.

longitudinal variations are the strongest of the entire globe. Also, the high LW radiation at the central Pacific near the date line is as strong in the tropics as in the subtropics for both January and July and the intensity over the tropical Atlantic is at the same magnitude as in the subtropics as well. It is the three huge low LW centers of the Congo, the Amazon and Indonesia that contribute to the low zonal average outgoing LW at the tropics. It is somewhat misleading to say that the outgoing LW at the tropics is relatively low compared to that of the subtropics.

Over the continents, reducing the air temperature will increase RH, so that low temperature with high relative humidity will further reduce low outgoing LW radiation. This phenomenon occurs in winter Siberia, Greenland and summer Central Asia, where the surface temperature of the high plateau is relatively low compared to adjacent regions, therefore a deep trough of LW contours occurs here.

Minnis and Harrison (1984, hereafter denoted as MH) have studied a regional clear sky outgoing longwave radiation (OLWR) of November 1978 using GOES data. The monthly mean of this region, from longitude 30°W to 125°W, latitude 45°N to 45°S with 2.5°x2.5° resolution is shown in Figure 4.15. For comparison, our calculation of climatological November clear sky outgoing LW flux is shown in Figure 4.16. Regardless of the coarser resolution of our coordinates and the different averaging time, there is good agreement between the two results. The locations of the low OLWR flux center at northwest South America, the high OLWR flux centers off-shore of Brazil, the southeast Pacific and Caribbean sea, and a shallow trough over continental United States

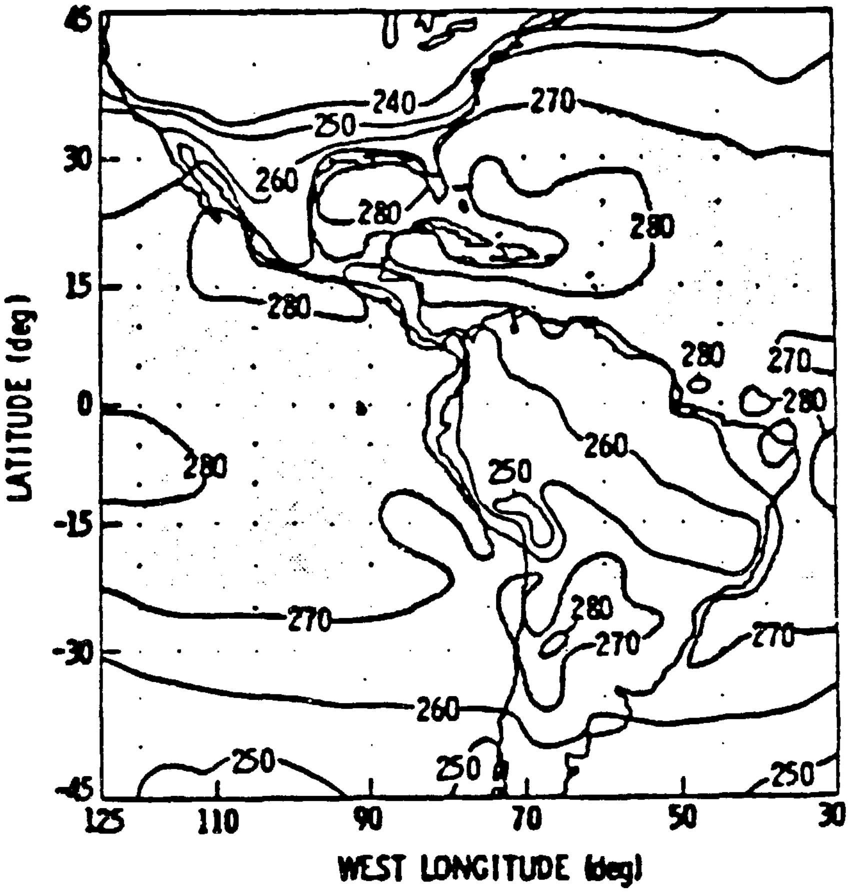

Figure 4.15 GOES regional clear sky OLWR observation for November, 1978 after Minnis and Harrison (1984), in W/m^2.

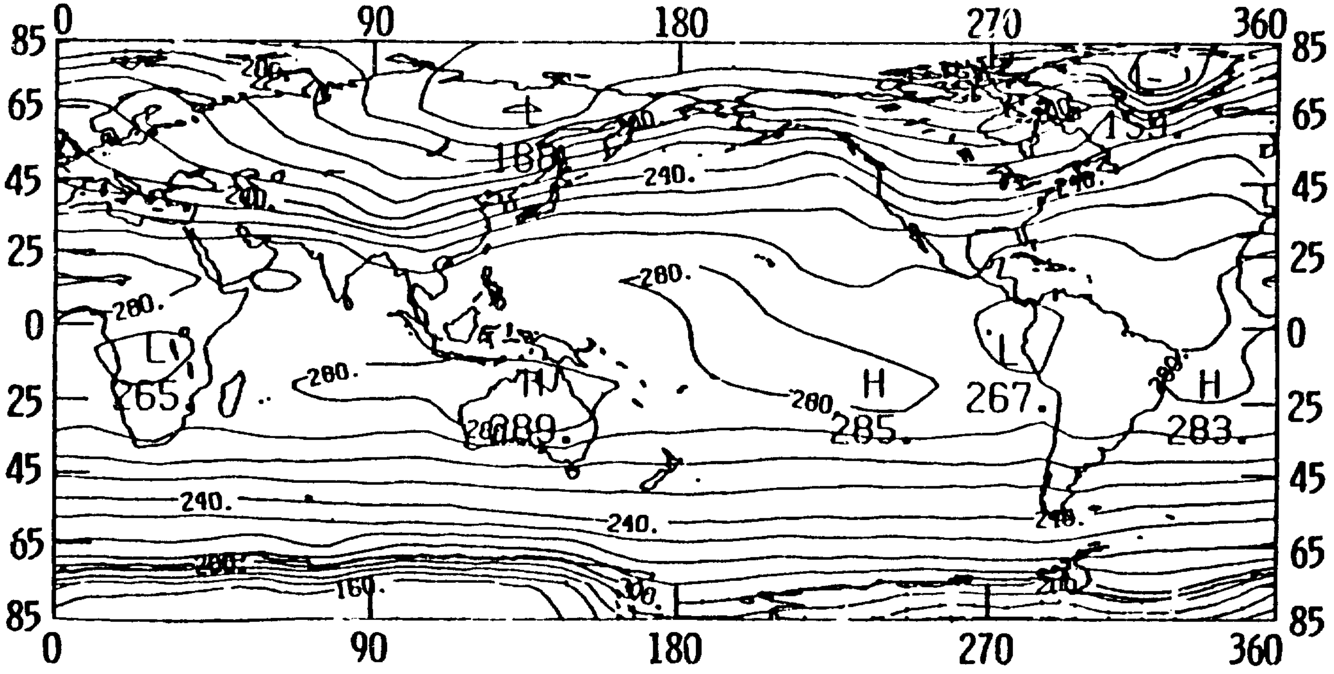

Figure 4.16 Clear sky OLWR map for November, in W/m^2.

are all well simulated. Also the intensity of OLWR flux over the oceans are in good agreement. However, over Brazil our calculation is about $10W/m^2$ overestimated. This might suggest that averaged RH is underestimated at this region, or the surface temperature of November 1978 is below normal at this region.

As one compares the OLWR field, Figure 4.16, with temperature and averaged RH fields, Figures 4.17 and 4.18, it is clear that averaged RH highly changes the OLWR flux pattern. This result indicates that water vapor is one of the dominant factors of outgoing LW flux. Even without the presence of cloud, OLWR field is modulated by water vapor distributions.

The simple Budyko-Sellers type parameterization of OLWR calculation is often used:

$$F= A+BT \qquad 4.12$$

where F is OLWR flux, T is surface temperature, and A and B are constants. The above result implies that this equation significantly biases the radiation field by omitting water vapor.

4.7 Sensitivities of the Interpolation Coefficients

As pointed out in section 4.3, some coefficients in equation 4.2 and 4.4 are rather arbitrarily chosen. These might have substantial impact on the outgoing LW radiation. In this section, we present a sensitivity analysis of coefficients to show how the outgoing LW responds and verify that the outgoing LW radiation has minimal sensitivities to the changes of these coefficients. For convenience, these two equations are repeated here, and only the results of the

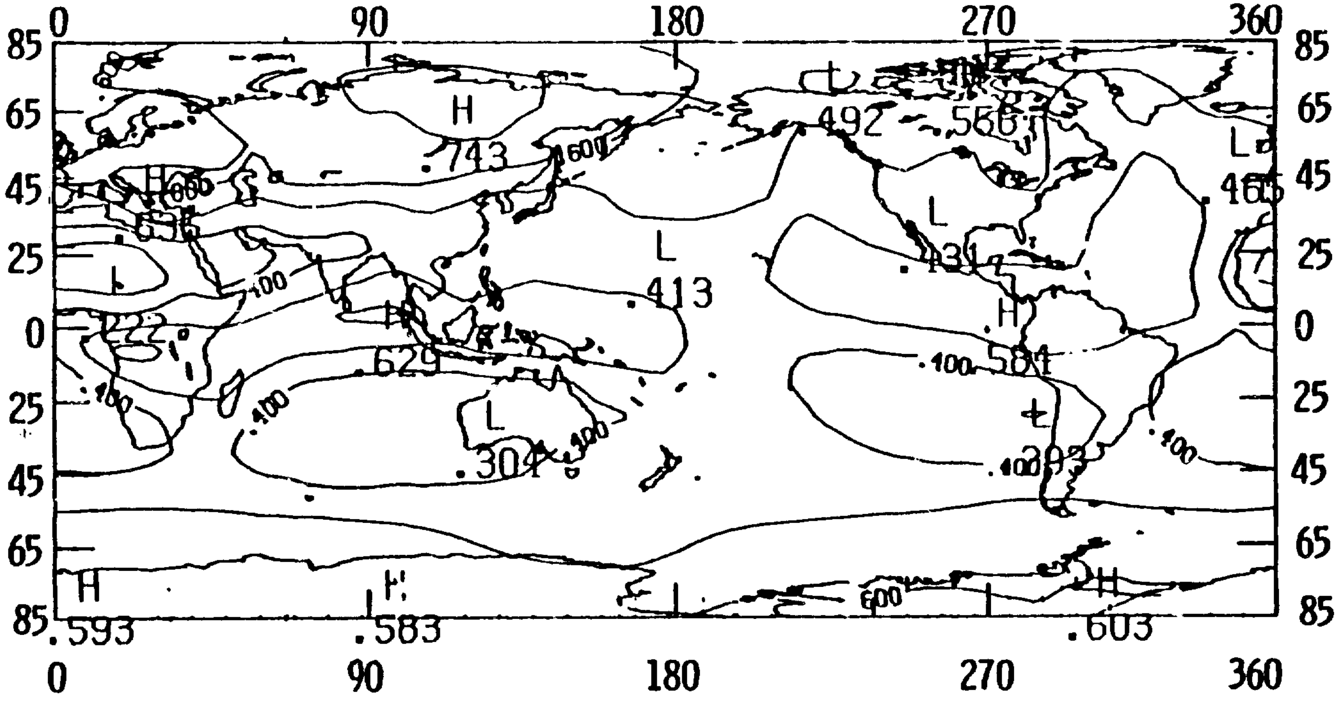

Figure 4.17 RH map for November.

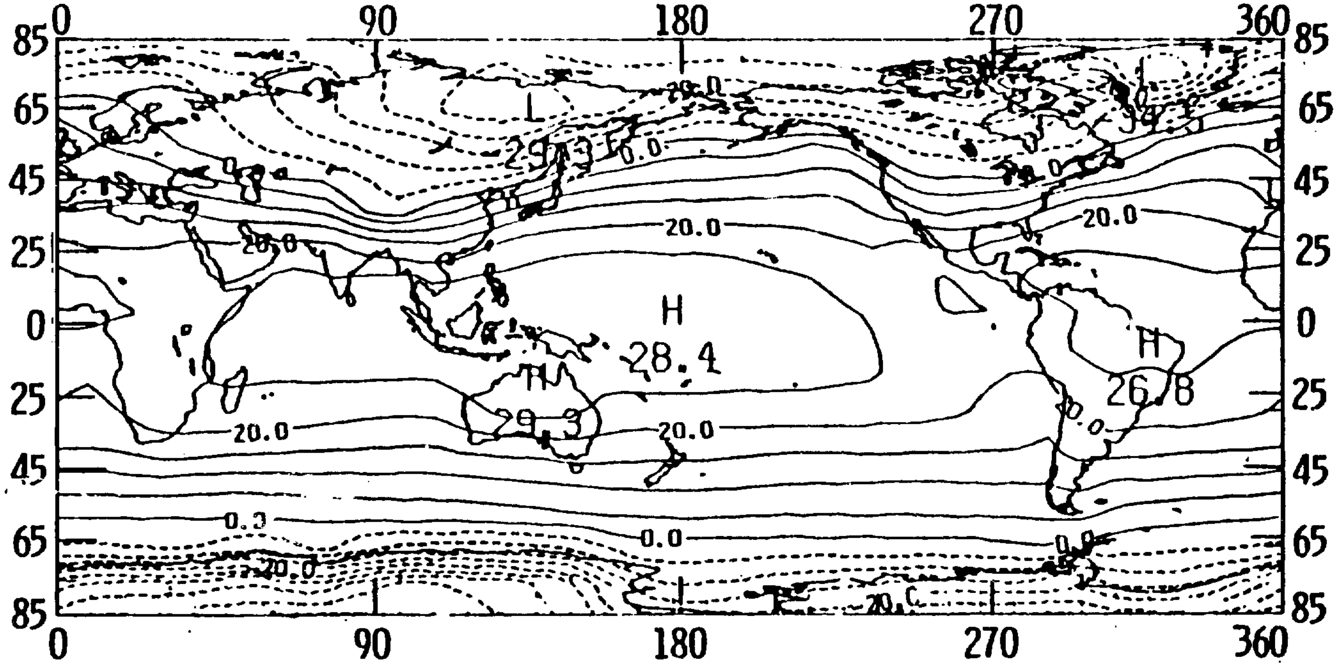

Figure 4.18 Climatological Ts map for November, in °C.

July cases are plotted. The January cases have similar results.

$$Q_{100mb}(J)=3x10^{-6}/(1+(J-20)^2/128) \qquad 4.2$$

$$n(J)=0.86x(1+(J-19)^2/1500) \qquad 4.4$$

Case A

The coefficient 0.86 in equation 4.5 is perturbed to 0.80 and 0.90. The results of the July case are plotted in Figure 4.19. As the figure shows, changing the coefficient 0.86 has more influence on the tropics and less toward the poles. Changing the coefficient from 0.86 to 0.80 increases the RH at the equator by 9% and reduces the clear sky outgoing LW by 6 W/m^2. Changing it from 0.86 to 0.90 reduces the RH at the tropics by 5% and increases the clear sky outgoing LW by $2.5W/m^2$. These differences are smaller than those from different radiative transfer models, where $8W/m^2$ variation on OLWR are not uncommon (Luther, 1983). The original number used by Briegleb and Ramanathan (1982) is 0.85. The differences between their work and this study are negligible.

Case B

Perturbing the coefficient 1500 in equation 4.5 from 1000 to 2000 only slightly influences the RH and outgoing LW at mid latitudes, as shown in Figure 4.20. This is the least influential coefficient.

Case C

In Harries' water vapor mixing ratio formula, equation 4.2, the coefficient $3x10^{-6}$ stands for the average mixing ratio measured by

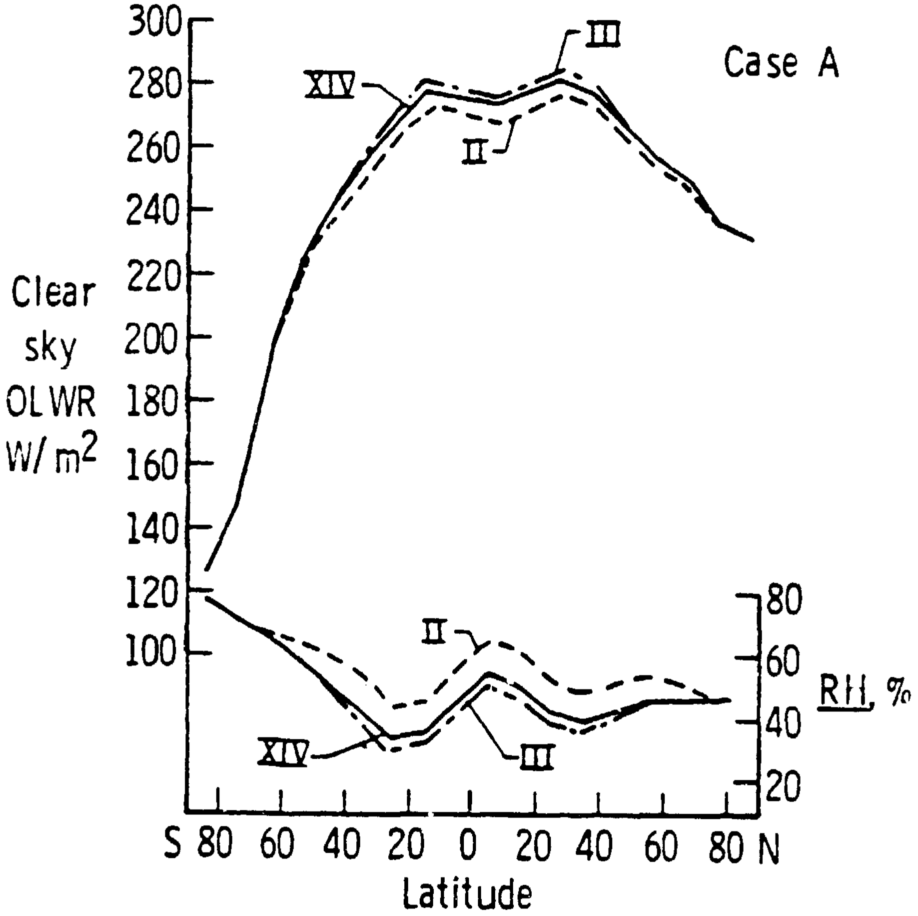

Figure 4.19 Sensitivity of RH and clear sky OLWR to the interpolation parameter, Case A. XIV is the undisturbed case; II changes 0.86 in equ. 4.5 to 0.80 and III changes 0.86 to 0.90.

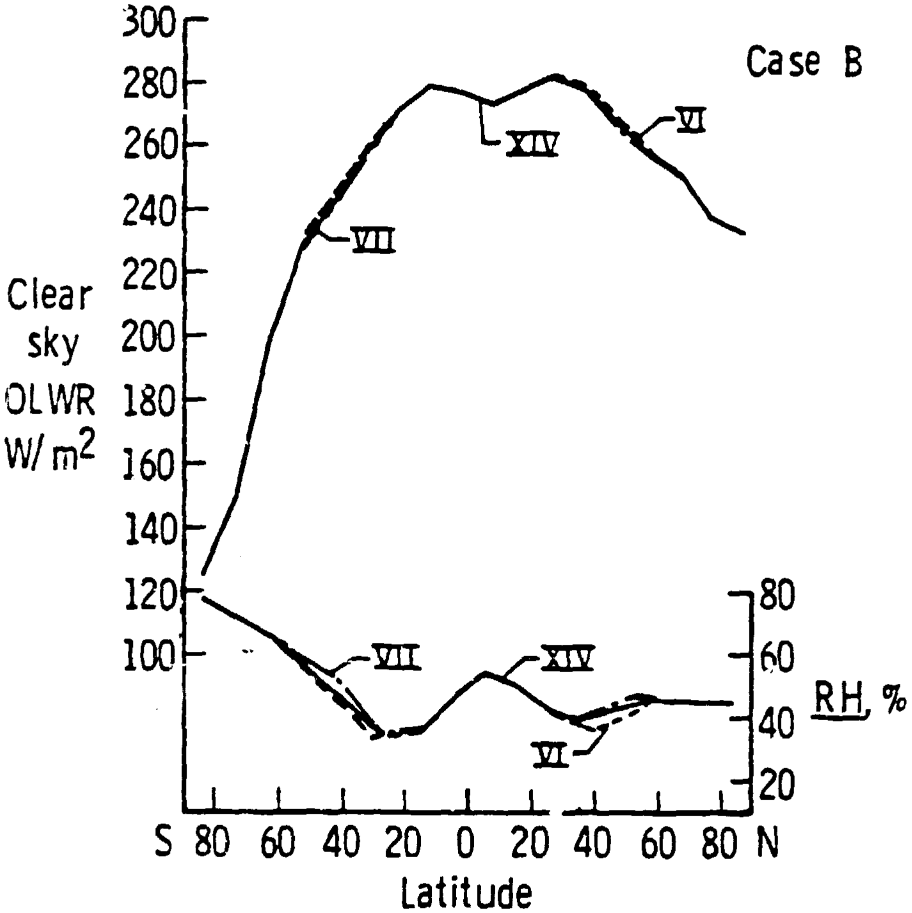

Figure 4.20 Same as figure 4.19, but for Case B. XIV is the undisturbed case; VI changes 1500 in equ. 4.15 to 2000 and VII changes 1500 to 1000.

various experiments at 100mb, see Figure 4.1. This coefficient has a linear response on the averaged RH for all the latitudes. For example, at the tropics, changing the coefficient 3×10^{-6} to 6×10^{-6}, see Figure 4.21, would increase the averaged RH from 54% to 60% and reduce clear sky outgoing longwave radiation by approximate $4W/m^2$. Changing the coefficient 3×10^{-6} to 1×10^{-6} would reduce the averaged RH from 54% to 47% and increases clear sky outgoing longwave radiation by about $5W/m^2$. Therefore, a six-fold change of mixing ratio, from 1×10^{-6} to 6×10^{-6}, would only change clear sky outgoing longwave flux by 9 W/m^2, only about a 4% variation. Thus the longwave flux calculation is insensitive to this perturbation.

In conclusion, we adapted all the coefficients chosen by other investigators except to slightly tune the coefficient 0.85 in equation 4.5 to 0.86. We found that the averaged RH profile is in good agreement with Thompson and Warren's in the low and mid latitudes, and also found very good agreement in zonal averaged clear sky OLWR profile for all latitudes. The changes in these coefficients has little effect on clear sky OLWR which would imply even less error for cloudy sky OLWR. Cloudy sky OLWR will be discussed in Chapter 6.

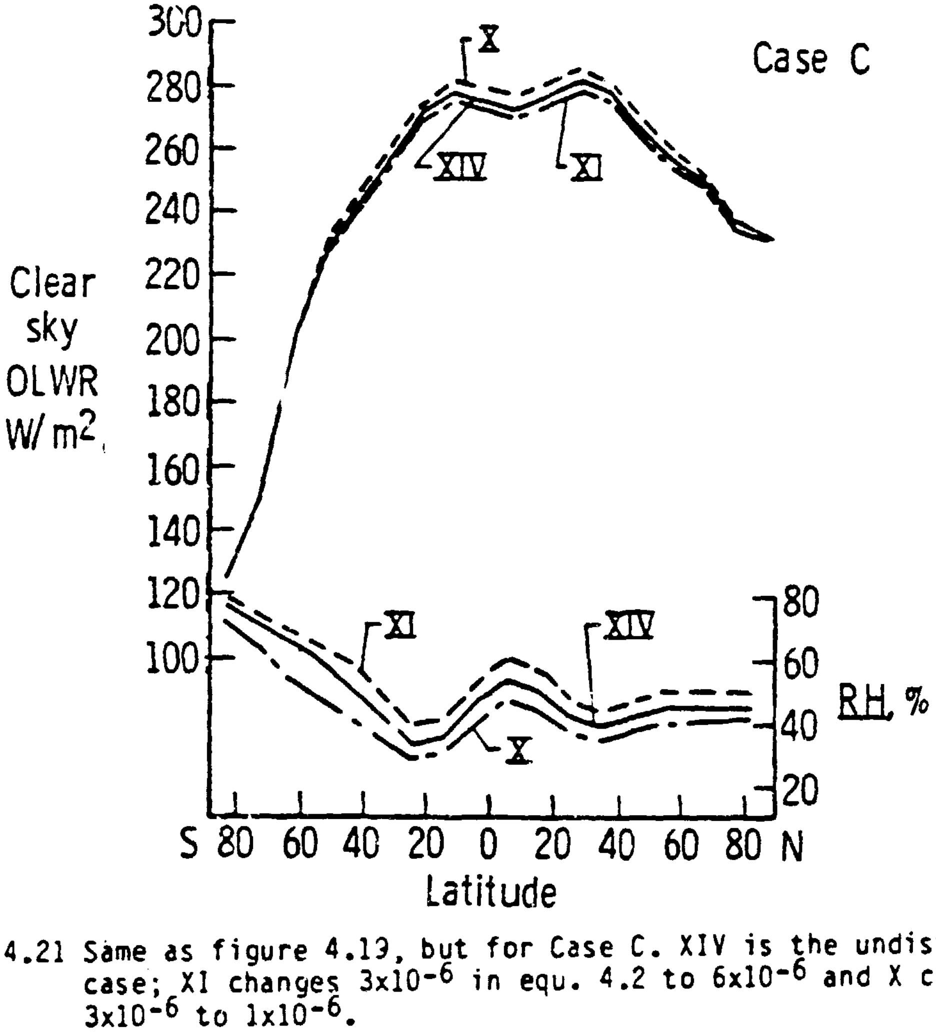

Figure 4.21 Same as figure 4.13, but for Case C. XIV is the undisturbed case; XI changes 3×10^{-6} in equ. 4.2 to 6×10^{-6} and X changes 3×10^{-6} to 1×10^{-6}.

CHAPTER 5

CLOUD AND CLOUD TOP TEMPERATURE

This Chapter is devoted to two subjects: cloud cover and cloud top temperature T_C. For the cloud cover, from section 5.1 through 5.4, the impact of cloud on climate and cloud observation is first reviewed. Then, the Sherr et al. (1968) cloud cover model, which is incorporated into the outgoing longwave radiation (OLWR) calculation, is discussed. The distribution of cloud cover follows. For the cloud top temperature T_C, in section 5.5 the techniques of the measurement are first reviewed, then a set of T_C data is compiled and compared with a region with satellite observation. A brief summary follows in section 5.6.

5.1 Cloud and Climate

Earth OLWR, unlike idealistic clear sky OLWR as discussed in the previous chapter, is highly modulated by the dynamics and thermodynamic processes of clouds. The presence of most clouds traps the higher longwave (LW) radiation from the surface and emits its own lower LW radiation to space. This process conserves earth OLWR, and is often referred to as the cloud greenhouse effect. With a theoretical model, Kuhn (1978) showed that outgoing longwave flux (OLWF) depends on cloud height, e.g. the greenhouse effect intensifies as the elevation of the cloud deck increase. However, in polar regions where the temperature inversion is strong and water vapor density is low, inserting a cloud deck would increase OLWF substantially. More recent observations by Minnis and Harrison (1983) also showed high anti-correlation between diurnal cloud cover and OLWF for a few locations in the mid latitude of the Southern Hemisphere. The multilayered clouds complicate this problem, especially high thin cirrus type clouds with less opacity. For example, it was pointed out by Heiman (1981) that sophisticated GCM's underestimated OLWR because higher LW radiation from lower warmer cloud can penetrate through overlying cirrus.

In addition to its effect on the LW radiation, cloud also has very strong influence on solar short wave (SW) radiation. Its presence reduces insolation on the surface and its albedo, which is higher than the surface, increases the reflection of SW to space, which is often referred to as cloud albedo effect.

Global surface albedo is only about 13%, while cloud albedo can range from 20% to as high as 90%. This effect competes with the greenhouse effect, so that the degree of the cloud's net impact on the climate, cloud feedback effect, is still controversial. Schneider (1972) first used an atmospheric model to analyze the relative magnitude of each component. He defined a parameter

$$\delta = \frac{\partial F}{\partial C} - \frac{\partial A}{\partial C} \qquad 5.1$$

where A is absorbed solar flux, F is OLWF, and C is cloud cover. When δ is negative, the albedo effect dominates, and when δ is positive, the greenhouse effect dominates. He found that, with the constraints of fixing other atmospheric factors, the effect of increasing global average cloud cover is to decrease the global average surface temperature due to higher albedo effect. However, Cess and Ramanathan (1978) stressed that any discussion of the radiative effect of changing global cloud amount or atmospheric transparency must consider the possibility of change in the distribution and the type of cloud as well, which is not well understood yet. One of the most difficult problems involved is the the lack of an unique definition of cloud cover. Because cloud has different characteristics for different wavelengths, effective cloud cover for incoming solar radiation might differ significantly from that of outgoing LW radiation. Ohring and Clapp (1980) and Hartman and Short (1980) used OLWF versus albedo instead of using cloud cover directly to determine the net energy budget.

$$\delta = \frac{\partial F}{\partial C} - \frac{\partial A}{\partial C} = -Q \frac{\partial \alpha}{\delta C} + \frac{\partial F}{\partial C}$$

$$= \left(- \frac{\partial F}{\partial C} \right) \times \left(Q \left(\frac{\partial F}{\partial \alpha} \right)^{-1} + 1 \right) \qquad 5.2$$

$$\text{cloud factor} = \left(Q \left(\frac{\partial F}{\partial \alpha} \right)^{-1} + 1 \right) \begin{cases} 1, & \text{Greenhouse effect only.} \\ 0, & \text{Greenhouse effect balance albedo effect exactly.} \\ -N, & \text{albedo effect is N+1 times as large as greenhouse effect.} \end{cases}$$

where α is albedo, Q is one fourth of the solar constant. This method, however, did not eliminate other atmospheric variations, such as water vapor content, lapse rate, etc.. Cess, et al. (1982) also discussed that using different satellite data would change the results substantially due to different data sampling technique. Although the effect of the cloud feedback on net radiation balance is still uncertain (Hartman, 1983), there seems to be a good agreement with the result of Schneider (1972) that cloud albedo effect dominates the greenhouse effect except for very high cirrus type cloud.

Warren, et al. (1983) used 35 years of ship observations to study cloud cover over ocean area, and found that there are statistically significant trends for different types of cloud over different areas, e.g. 1% per 10 year decrease in cumulus over most ocean areas of both hemispheres and a similar increase in stratus and stratocumulus over all ocean areas except the northwest Atlantic during all seasons and the eastern South Tropical Atlantic during Southern Hemispheric summer. It is intriguing to ask how this trend changes the climate or why this cloudiness trend appears in the data. But, the first important problem involved here is cloud observation.

5.2 Cloudiness Observation

It is redundunt to stress how subjective cloud observations, both cloud classification and cloud cover, are. A simple example is that cloud cover reported in early morning and late afternoon tend to be overestimated because high solar zenith angle will enhance the perception of the lateral area of cloud. Another problem on surface observation is the lack of stations over many remote regions, although ship observations help to fill in very sparse data over ocean. To have a global surface cloud observation network is very impractical. Despite such difficulties, London (1957) compiled a seasonal climatology of total cloud cover distribution for the Northern Hemisphere. It is still one of the most referred works, regardless of their accuracy. Later a similar work for the Southern Hemisphere was done by van Loon (1972).

Satellites provide an easier way for sampling data. Early polar orbiting TIROS satellites had limited ground coverage and limited sampling times. Clapp (1964) utilized this satellite photography and performed some nephanalyses of seasonal global cloud cover from March 1962 to February 1963. This study showed that global cloud has some characteristic patterns over seasons and concluded that the cloud distribution on large-scale must posses a certain stability or repetitiveness over the entire seasons, even in the regions of migratory cyclones and anticyclones. Clapp did not quantitize the result, such that it can not be used to verify London's (1957) previous work; nevertheless it did verify the feasibility of classification of cloud cover from space and its agreement with surface observation for zonally averaged results. Another work by Kornfield and Hasler (1969) used a multiple exposure technique for developing monthly averaged cloud cover pictures and then performing nephanalyses. Ths study clearly identified the ITCZ and some quasi-stationary waves. Still both Clapp's and Kornfield and Hasler's work were very dependent on subjective judgement of an experienced analyst.

A number of more objective methods have been proposed. Instead of using photography, different channels of radiation band are used to reconstruct cloud pictures, such as was done by Shenk and Solomonson (1972). Their threshold method for using visible channel brightness from a high resolution scanning radiometer can produce good results, if the field of view is completely filled with cloud or completely cloud free. However, if the assumed condition does not prevail, the potential error could be as high as 75%. Another method, the spatial coherence method (Coakley and Bretherton, 1982) using advanced very high resolution radiometer (AVHRR) information, can determine single-layered cloud cover or multilayered cloud cover extended over moderate layer regions. Chahine et al. (1983) used multichannel high resolution infrared scanner (HIRS) and microwave sounding unit (MSU). This method can determine the effective cloud cover under the assumption that the cloud is single-layered and non-reflective.

An effort, the International Satellite Cloud Climatology Project (ISCCP, Schiffer and Rossow, 1983) has been initiated for organizing the data collection and processing to determine temporal and spatial variability of the amount, type and radiative properites of clouds. This study will not only provide a global data set for clouds, but also lead toward a better understanding and enhance the ability of climate modeling.

5.3 Sherr et al. Cloud Model

5.3.1 The Model

Sherr et al. (1968) compiled an empirical global cloud cover mo-

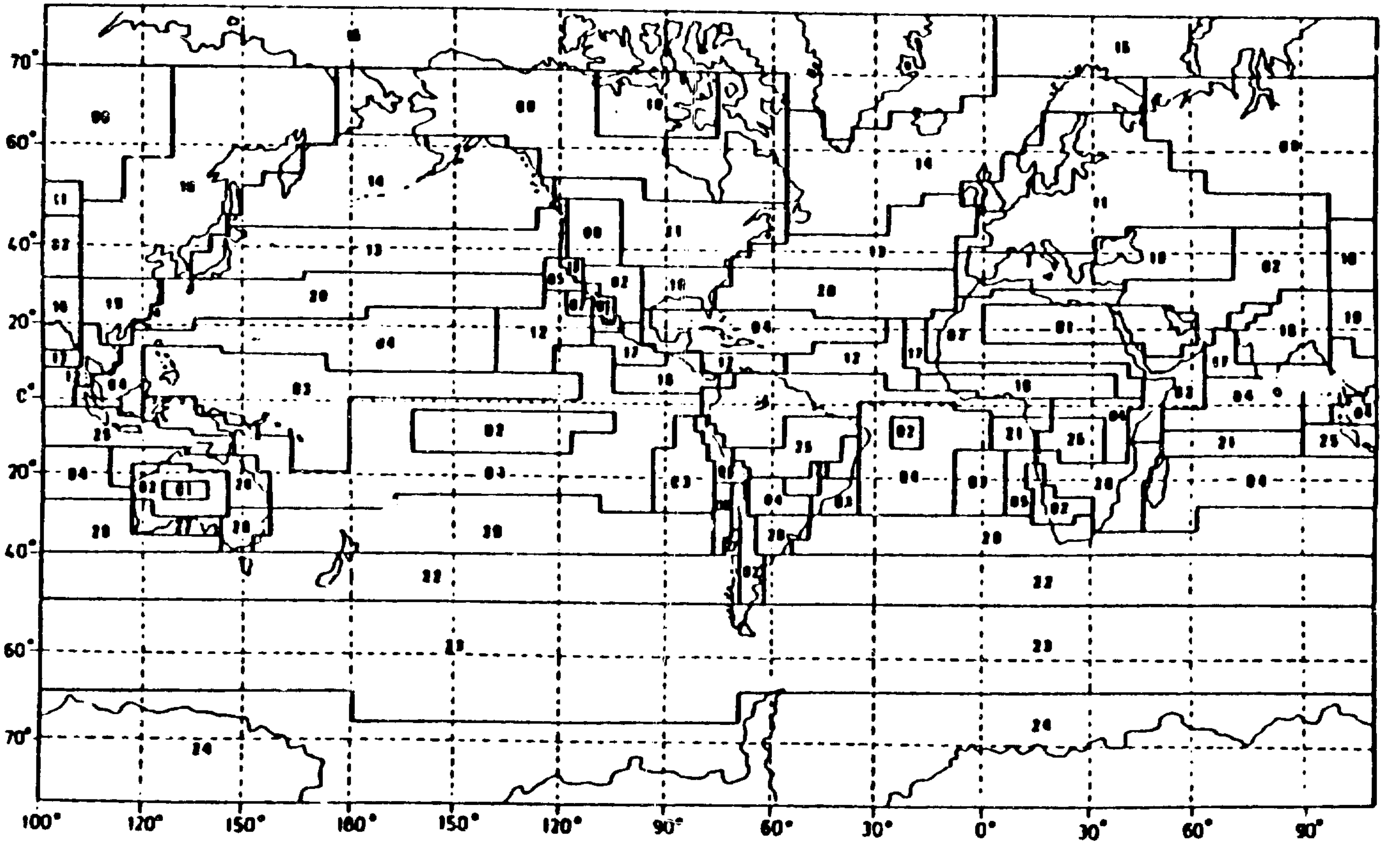

Figure 5.1 The positions of the 29 regions on the world map (after Sherr et al., 1968).

del, originally intended for simulation of the effects of cloud cover on proposed earth-viewing space missions. The surface of earth is divided into 29 cloud climatological regions as shown in Fig. 5.1. Within each region, cloud is assumed homogeneous. This feature provides the interface with the outgoing LW parameterization of Thompson and Warren (1982) used in this investigation, which requires a single deck effective cloud cover as a predictor (see Chapter 2). We adapted the model with modifications suitable for this study. A general description of the nature of the cloud in each cloud climatic region is given in Table 5.1.

In constructing the model, Sherr *et al.* (1968), the data from satellites were used to identify the regions where the cloudiness is homogeneous. Ground-based observations were used to construct cloud cover frequencies. Data from as many areas as possible were assembled and from these a representative station was identified. Data from this station were usually based on at least 10 years of observations.

5.3.2 Other Studies with Sherr et al. Model

Based on the results of Sherr *et al.*, Falls (1974) statistically analyzed the cloud cover frequency and concluded that world cloud cover behaves as a Beta probability distribution, which can describe the cloud cover field well with relevent values of two parameters.

Based on the surface classification of Sherr *et al.* model, Henderson-Sellers (1978) studied the surface type and its effect on

Table 5.1 General description of cloud climatological regions after Sherr et al. (1968).

1	2	3	4	5	6	7	8	9
Region Number	General Description	Location	Seasonal Change in Cloud Amount	Mean Monthly Cloud Amount Jun-Aug (In Percent)	Mean Monthly Cloud Amount Dec-Mar (In Percent)	Predominant Cloud Type	Diurnal Variation in Cloud Amount	Hour of Maximum Cloud Amount (Local Time)
01	Essentially Clear	Major Desert Area	Small	< 20	< 20	--	Small	----
02	Little Cloudiness	Sub-Desert Areas	Small	< 40	< 40	--	Small	----
03	Tropical Cloudy	Near Equator	Small	> 60	> 60	Convective	Large	1600
04	Tropical Moderate Cloudiness	North or South of Region 03	Small	∿ 50	∿ 50	Convective	Large	1600
05	Desert Marine	Over Ocean - off West Coasts	Small	∿ 50	∿ 50	Stratiform	Large	0800
06	Desert Marine Cloudy Winter	Over Ocean - West of Peru	Extreme	> 70	< 30	Stratiform	Large	0800
07	Desert Marine Cloudy Summer	Over Ocean - West of Baja California	Extreme	> 70	< 30	Stratiform	Large	0800
08	Mid Latitude - Clear Summer	North America	Extreme	< 40	∿ 70	Synoptic Scale	Small	----
09	High Latitude - Cloudy Summer	North America, Asia	Moderate	∿ 70	∿ 50	Synotpic Scale	Small	----
10	High Latitude - Clear Winter	Asia, North America	Extreme	∿ 70	< 30	Synoptic Scale	Small	----
11	Mid Latitude - Land	Northern Hemisphere	Moderate	∿ 50	∿ 70	Synoptic Scale	Small	----
12	Tropical - Cloudy Summer	North of Region 03	Moderate	> 60	∿ 50	Convective	Large	1600
13	Mid Latitude - Ocean	Northern Hemisphere	Moderate	∿ 60	> 70	Synoptic Scale	Small	----

Table 5.1 continued.

1	2	3	4	5	6	7	8	9
14	High Latitude - Ocean	Northern Hemisphere	Moderate	> 80	~ 70	Synoptic Scale	Small	----
15	Polar	Northern Hemisphere	Small	~ 60	~ 60	Synoptic Scale	Small	----
16	Tropical - Seasonal Change	North of Region 03	Extreme	> 70	< 40	Convective	Large	1600
17	Tropical - Clear Winter	Northern Hemisphere Near Region 16	Moderate	~ 50	< 30	Convective	Large	1600
18	Mediterranean	Northern Hemisphere Europe, Western North America	Extreme	~ 30	--	Convective	Small	----
				--	~ 60	Synoptic Scale	Small	----
19	Sub Tropical	Northern Hemisphere ~ 30N	Moderate	~ 50	--	Convective	Large	1600
				--	> 60	Synoptic Scale	Small	----
20	Sub Tropical - Ocean	Northern Hemisphere ~ 30N	Moderate	~ 50	--	Convective	Small	----
				--	> 60	Synoptic Scale	Small	----
21	Tropical - Cloudy Summer	South of Region 03	Moderate	~ 50	> 60	Convective	Large	1600
22	Mid Latitude Ocean	Southern Hemisphere	Moderate	~ 70	~ 60	Synoptic Scale	Small	----
23	High Latitude - Ocean	Southern Hemisphere	Moderate	~ 70	> 80	Synoptic Scale	Small	----
24	Polar	Southern Hemisphere	Small	~ 60	~ 60	Synoptic Scale	Small	----
25	Tropical - Seasonal Change	South of Region 03	Extreme	< 40	> 70	Convective	Large	1600
26	Tropical - Clear Winter	South of Region 25: Africa, Australia	Moderate	< 30	~ 50	Convective	Large	1600
27	Mediterranean	Southern Hemisphere Australia, Chile	Extreme	--	~ 30	Convective	Small	----
				~ 60	--	Synoptic Scale	Small	----
28	Sub Tropical Land	Southern Hemisphere ~ 30S	Moderate	--	< 50	Convective	Large	1600
				~ 60	--	Synoptic Scale	Small	----
29	Sub Tropical - Ocean	Southern Hemisphere ~ 30S	Moderate	--	~ 50	Convective	Small	----
				> 60	--	Synoptic Scale	Small	----

cloud cover. She has also found the Beta distribution useful as a model for the cloud cover frequency. Her results also imply that cloud frequency curves over land in high latitudes, mid-latitudes and subtropical latitudes are similar, while the frequency distributions of cloud cover differ (1) over land and ocean at the same latitude and (2) over ocean areas in different latitude zones.

Combining with 45 months of satellite radiation measurements, Bean and Somerville (1981) derived a Beta distribution world-wide cloud cover model. This model can describe cloud fields very concisely. However, the parameters were derived from fairly small size sample, such that statistical confidence is not achieved. Also, utilizing the model to other time period other than that the parameters were derived might cause significant error.

5.3.3 Modification of Sherr et al. Model

A version of the Sherr et al. cloud model used by Bartman (1980) in his albedo model is incorporated into this study. Since the cloud climatic region areas of Sherr et al. did not begin and end on the 10°x10° latitude-longitude lines of our models, Bartman stretched or contracted slightly the map areas in order to fit the model grid system. Table 5.2 shows the cloud climate regions used for each 10°x10° area in Bartman's model and this study.

As the result of this process, one would notice that along the latitude 65°S on table 5.2, the cloud type is alternating between type 23 and type 24. On a contour plot of cloudiness, this would produce unrealistic wavy curves along latitudes 55° to 75°. Thus,

Table 5.2 Positions of the 29 cloud cover type regions for the 10°x 10° longitude-latitude model after Bartman (1980).

36	35	34	33	32	31	30	29	28	27	26	25	24	23	22	21	20	19	18	17	16	15	14	13	12	11	10	9	8	7	6	5	4	3	2	1	J/K
15	15	15	15	15	15	15	15	15	15	15	15	15	13	15	15	15	15	15	15	15	15	15	15	15	15	15	15	15	15	15	15	15	15	15	15	1
15	15	15	15	15	15	15	15	15	15	15	15	15	15	15	15	15	15	15	15	15	15	15	15	15	15	15	15	15	15	15	15	15	15	15	15	2
14	14	11	11	9	9	9	9	9	9	9	9	10	10	10	10	10	9		9	9	9	9	9	9	10	10	10	9	9	14	15	15	14	14	14	3
11	11	11	11	11	11	9	9	9	9	9	10	10	10	10	14	14	14	14	14	14	14	14	9	9	9	9	9	9	9	14	14	14	14	14	11	4
11	11	11	18	18	18	19	2	2	2	10	10	10	10	13	13	13	13	13	13	13	13	13	13	6	11	11	11	11	11	13	13	13	13	13	11	5
18	18	18	18	18	2	2	2	2	2	10	10	10	13	17	13	20	20	20	20	20	20	20	29	2	2	19	19	20	20	20	20	20	20	20	18	6
1	1	1	1	1	1	2	16	16	16	19	19	20	23	20	20	20	20	4	4	4	4	12	12	7	2	4	4	4	4	4	4	4	20	2	2	7
2	2	2	2	2	2	17	17	16	16	12	4	3	3	4	4	4	4	4	4	4	4	12	12	4	17	17	16	17	17	12	12	12	12	2	2	8
16	16	16	4	2	2	4	4	4	12	4	4	3	3	3	3	3	3	3	3	3	3	3	3	4	16	16	4	3	3	3	3	3	3	3	16	9
21	21	25	4	2	4	4	4	4	25	25	25	4	3	3	3	3	3	4	2	2	2	2	2	2	4	4	3	3	3	25	25	4	2	4	4	10
5	25	25	4	26	21	21	21	21	4	4	26	25	25	4	4	3	3	4	4	4	4	4	4	4	4	4	3	6	25	25	21	4	4	4	3	11
3	2	26	26	4	4	4	4	4	4	4	2	1	2	26	4	4	4	4	4	29	4	4	29	4	4	3	3	5	4	4	3	4	4	4	3	12
29	29	29	29	29	29	29	24	29	29	29	29	27	27	28	25	29	29	29	29	29	29	29	29	29	29	29	29	5	28	28	29	29	29	29	29	13
22	22	22	22	22	22	22	22	22	22	22	22	22	22	22	22	22	22	22	22	22	22	22	22	22	22	22	22	22	2	22	22	22	22	22	22	14
23	23	23	23	23	23	23	23	23	23	23	23	23	23	23	23	23	23	23	23	23	23	23	23	23	23	23	23	23	23	23	23	23	23	23	23	15
23	24	24	23	24	24	23	24	24	23	24	24	23	24	24	23	24	24	23	23	24	23	23	24	23	23	24	23	23	24	23	24	24	23	24	24	16
24	24	24	24	24	24	24	24	24	24	24	24	24	24	24	24	24	24	24	24	24	24	24	24	24	24	24	24	24	24	24	24	24	24	24	24	17
24	24	24	24	24	24	24	24	24	24	24	24	24	24	24	24	24	24	24	24	24	24	24	24	24	24	24	24	24	24	24	24	24	24	24	24	18

instead of directly using the cloud cover at this region generated by the classification, we used equations 5.3 and 5.4 to smoothe the distribution portrayed in fig. 5.1.

$$f(j,16)=f(j,17)*2/3+f(j,15)*1/3 \qquad 1 < j < 7 \text{ or } 19 < j < 36 \qquad 5.3$$

$$f(j,16)=f(j,17)*1/3+f(j,15)*2/3 \qquad 8 < j < 18 \qquad 5.4$$

where j is a longitude index such that longitude is $J* 10^{\circ}-5^{\circ}$, and K is a latitude index such that latitude is $85^{\circ}-K*10^{\circ}$.

Monthly cloud cover used in this study is calculated as follows. Sherr et al. world-wide cloud cover distributions are given in five cloud cover categories, listed in table 5.3, for each of the 29 cloud climatological regions. Frequency distribution of the five possible cloud amount categories are given for eight local times at 0100, 0400, 0700,..., 2200. From the frequency distribution data and cloud cover categories, the percent cloud cover was calculated for each cloud climate region as a function of the eight different local times of the typical day for each month of the year. The monthly cloud cover is obtained by averaging the cloud covers of the eight local times.

A calculation of the global annual percent cloud cover from the above data gave a value of .60, which is much larger than the values .50 to .55 normally used, e.g. the global cloud cover of Hoyt (1976) was .532; Cess and Ramanathan (1978) suggested annual global cloud cover is between .45 to .55. Ramanathan (1976) used .45 as the effective total cloudiness for his radiative convective model.

C-2

Category	Cloud Cover in Tenths
1	0
2	1, 2, 3
3	4,5
4	6, 7, 8, 9
5	10

Table 5.3 Cloud Cover Category.

A multiplying factor GLCLC/60 has thus been incorporated into the cloud cover calculation. This factor is not only used to adjust the difference between the Sherr et al. model and the nominal value, but also accounts for the emissivity of the cloud, such that GLCLC/60x A_c equals effective cloudiness, where A_c is cloud cover from the Sherr et al. model. In the current study, GLCLC is set to 45 as by Bartman (1980, 1981).

5.4 Cloud Cover Distribution

5.4.1 Zonally Averaged Cloud Cover Distribution

Figures 5.2 and 5.3 show the zonally averaged cloud cover from (1) the modified Sherr's cloud model without the factor GLCLC and from (2) London and van Loon for January and July respectively.

Both months have general agreement between (1) and (2), i.e. maximum cloud cover in the tropics and middle latitudes and minimum cloud cover in the subtropics and polar regions. The high correlation between cloud cover and uppper air relative humidity can also be well identified (see Figures 5.4 and 5.5, taken from Telegadas and London, 1954).

However, the differences of the magnitudes between (1) and (2) are also very significant. Poleward greater difference could be possibly due to less observation frequency or higher human perception bias from larger zenith angle, or both. The verdict of better cloud cover climatology will not be issued until either Warren et al. or ISCCP results are revealed.

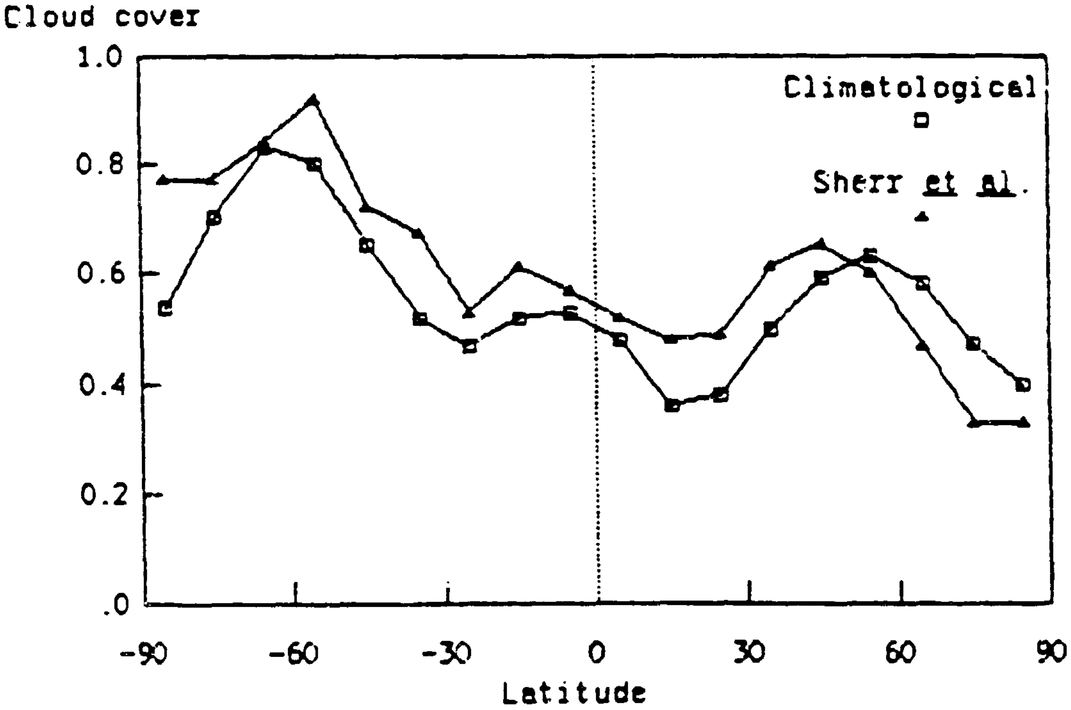

Figure 5.2 Comparison of the zonally averaged cloud cover between the climatology and Sherr *et al.* (1968), January.

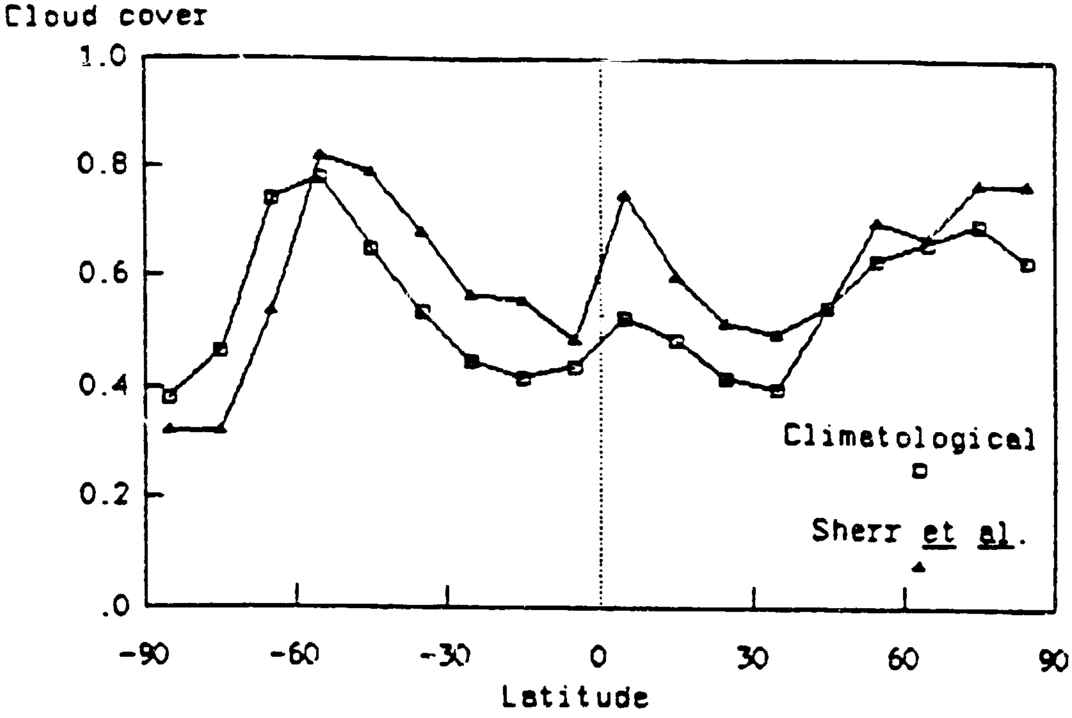

Figure 5.3 Same as figure 5.2, but for July.

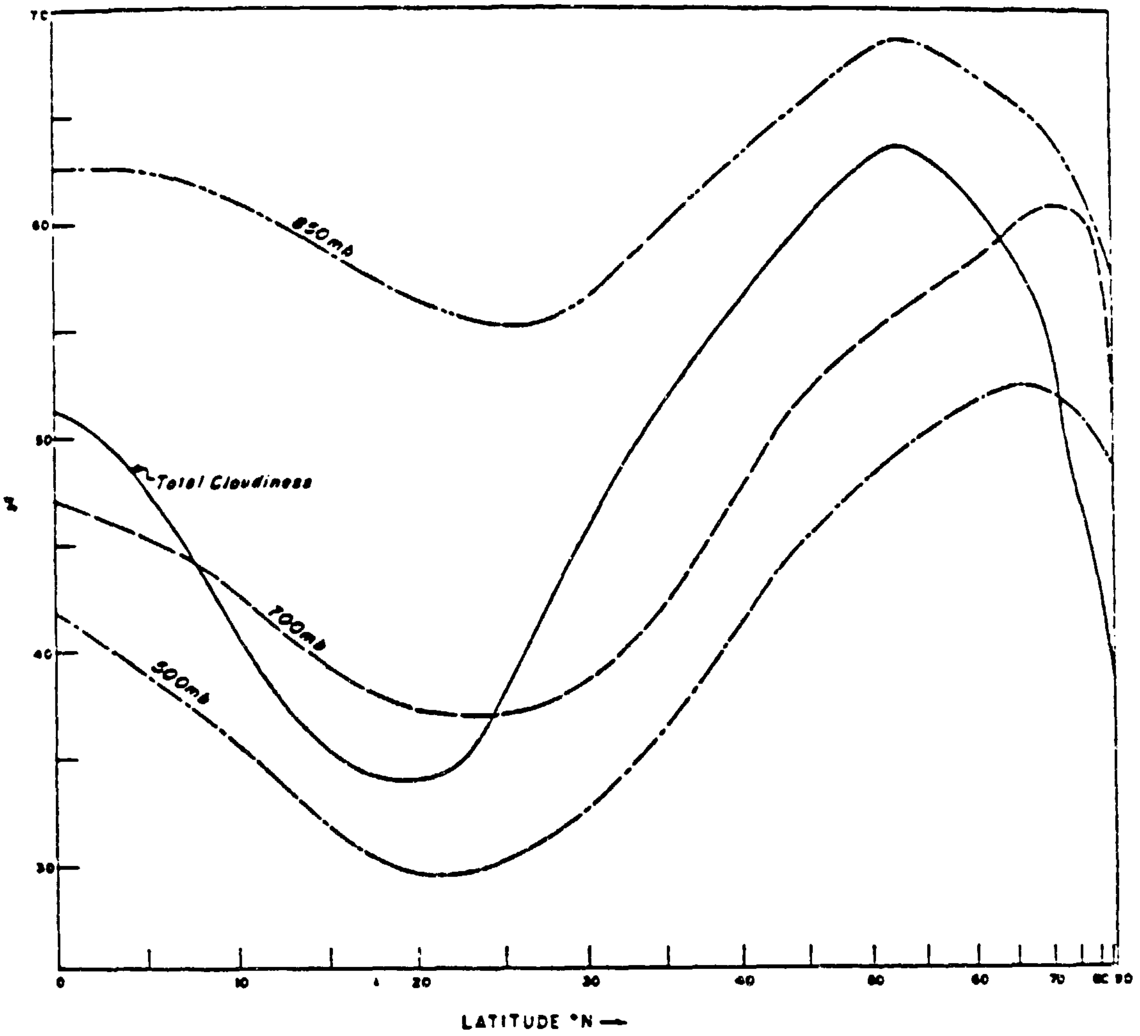

Figure 5.4 Averaged latitudinal distribution of the total cloud cover and relative humidity at the 850, 700 and 500mb---winter after Telegadas and London (1954).

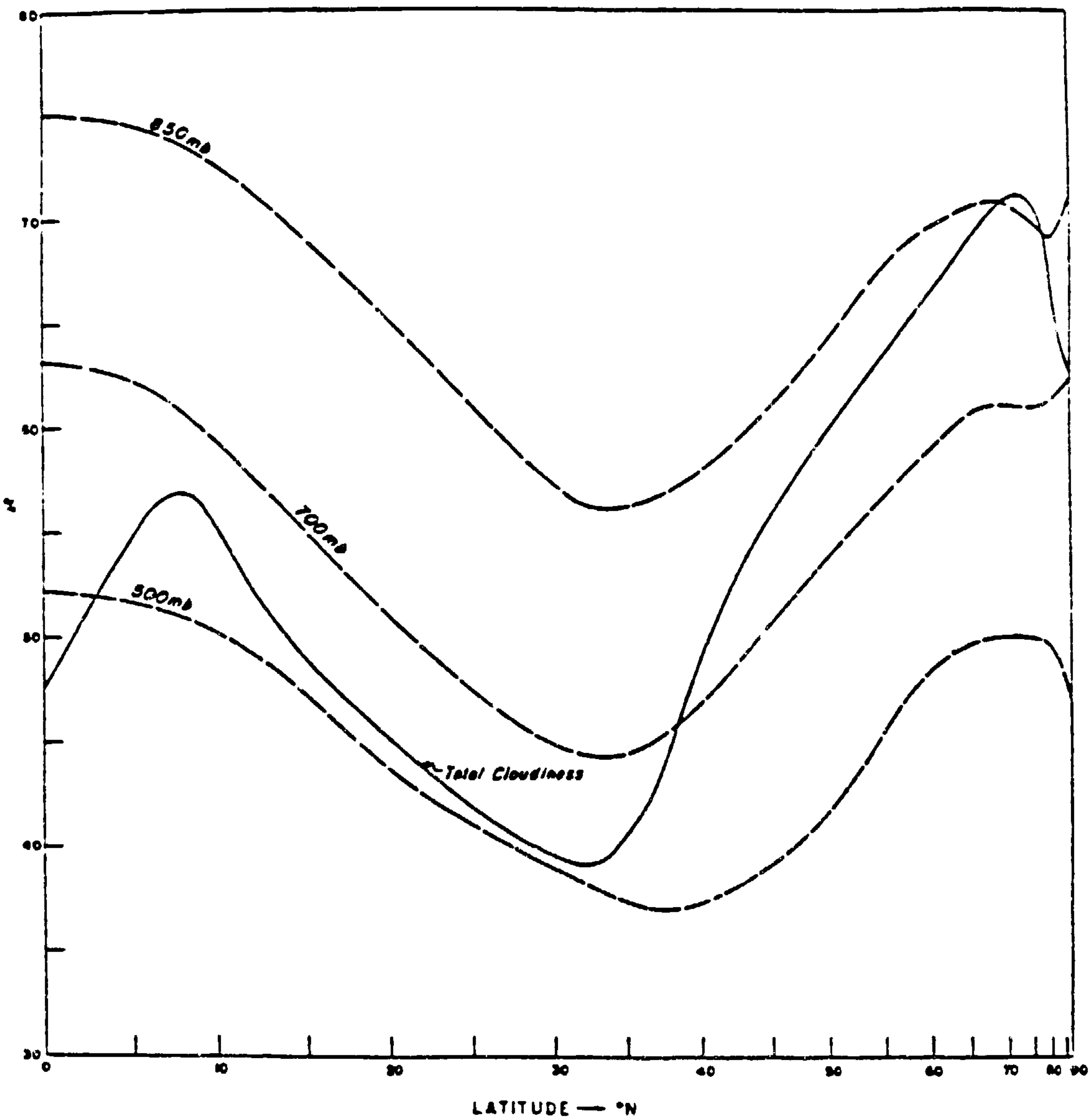

Figure 5.5 Same as figure 5.4, but for summer.

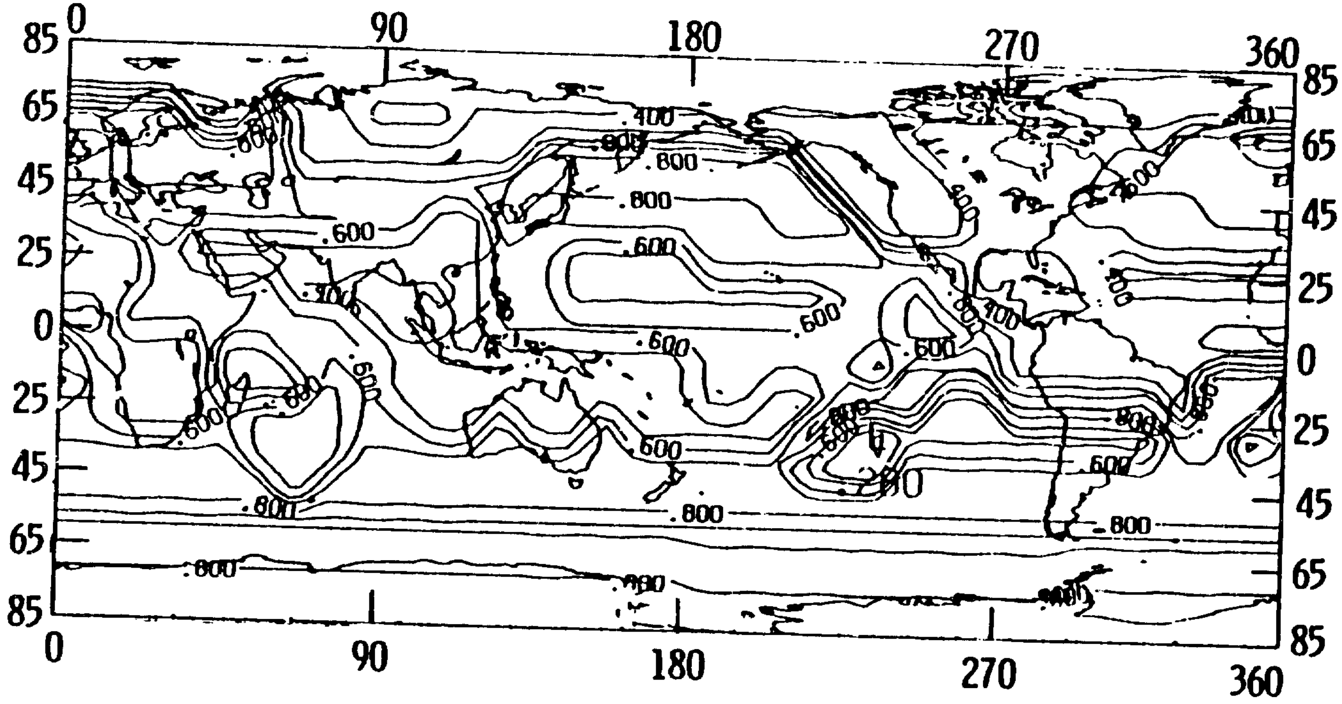

Figure 5.6 Cloud cover map for January derived from Sherr *et al*. (1968).

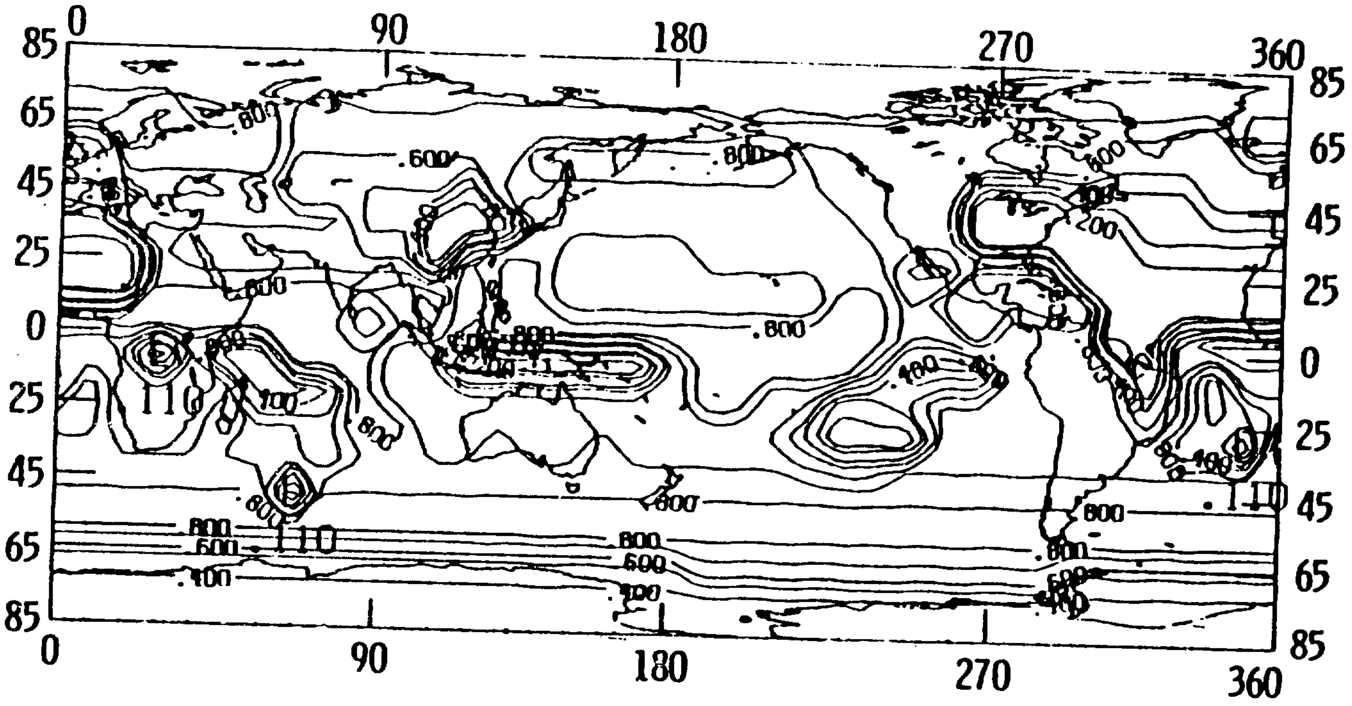

Figure 5.7 Same as Figure 5.6 but for July.

5.4.2 Global Distribution of Cloud Cover

Figure 5.6 and 5.7 are cloud cover contours from the data of Sherr *et al.* (1968) for January and July respectively.

In the Global cloud distribution, maximum cloud cover often occurs at the ITCZ, and the mid-latitude westerly zones where there is a warm moist surface region or large baroclinicity, etc., while minimum cloud cover occurs at the subtropical subsidence, high pressure centers, and polar subsidence regions. Other mechanisms, such as monsoonal circulation, also generate extreme cloud cover.

Tables 5.4 and 5.5 summarize the causes and the regions of extreme cloud cover for January and July respectively. Although for some region there might be more than one reason for the causes of extreme cloud cover, e.g. ITCZ coincides with moist surface, only the dominant reason is mentioned.

5.5 Cloud Top Temperature

5.5.1 Definition and Measurement

As pointed out both in Chapter 2 and in the previous section, the cloud cover used in this study is defined as the effective cloud cover, with emissivity equal to one. Thus, the definition of cloud top temperature refers to the temperature at the top of the effective cloud. Since not all of the cloud is black, the virtual cloud top might be lower than its physical location in order that emission at warmer level would compensate the smaller emissivity. However, in practice the exact location of the effective cloud top can not be defined using conventional radiosonde, neither can the cloud top

January	Causes	Locations
maximum cloudiness	ITCZ equatorial low	1. Maximum cloudiness along 5°S in the Indian Ocean continues into Western Pacific. 2. Eastern Pacific & Atlantic in the tropics which coincide with the strongest trade winds and cold sea surface temperature except Indian Ocean.
	Baroclinicity	1. In the Northern Hemisphere, the prevailing westerlies and their cyclonic storms are located at North America, Nortwest Europe. Northwest coast of North America, Alaska and Far East. 2. In the Southern Hemisphere are at circumpolar zone at subpolar latitudes.
	warm moist surface	1. The amazon and Congo Basin where tropical forest located. 2. Indonesia & tropical coast of Australia where warm sea surface temperatures located. This is also the region where the ascending arm of Walker circulation is located.
minimum cloudiness	subtropical high pressure	Eastern and southwestern section of subtropical high pressure in the Northern Hemisphere, eastern and northeastern section in the Southern Hemispheric high, Sahara, West Africa desert Southwest United States and Southwest South America. In the Southern Hemisphere the high pressure spread over almost all longitudes except those of the Andes mountains.
	monsoonal circulation	India under northeasterly winds.
	Polar region	North and South poles. However, it is difficult to confirm the observation during polar night. In the Northeast Siberia, Arctic and northern America, the cloudiness is highly dependent on the amount of open water.

Table 5.4 Summary of extreme cloud for January.

Siberia high pressure	Manchuria, although located in the westerly belt, cold high pressure cover this region.
Descending arm of Walker circulation	West Coast of Peru

Table 5.4 Continued.

July	Causes	Locations
maximum cloudiness	ITCZ equatorial low	1. Near equator in the Indian Ocean and an extention of cloudy band southeastward from New Guinea. 2. Northern and Central South America, Central Africa and equatorial Pacific.
	Baroclinicity	North displacement of Bermuda and Pacific high pressure centers: Principal cyclonic activities over Europe and North America is confined to the northern regions off Alaska. northern Europe, central and northern United States.
	monsoonal circulation	India
minimum cloudiness	subtropical high pressure	1. Northern Africa, southwest Asia, central Pacific and southwest United States where are on the eastern slopes of the high pressure waters. 2. South Pacific and West shore of South America, Desert Australia.
		Subpolar circumcircle over the Southern Hemisphere has less cloudiness than January.

Table 5.5 Summary of extreme cloud cover for July.

temperature be directly measured.

Cloud top temperature can be indirectly measured from satellite. As in the common single channel threshold method, cloud top temperature is the infrared equivalent blackbody temperature of cloud, which is measured by using a window band radiometer. Minnis and Harrison (1984) have analyzed a set of GOES data using this techinque.

A recent proposal by Chahine _et al_. (1983) presented a method using multichannel HIRS to retrieve both effective cloud cover and cloud top temperature independently. Under the assumption that the reflectivity of cloud in the IR region is zero and that the emissivity of the cloud at different infrared wavelengths are the same, the pressure level for the black cloud top location can be retrieved. The cloud top temperature is then assumed equal to its ambient temperature. The corresponding temperature sounding is retrieved using other channels. Although this method has been tested on NOAA weather satellite data, a global monthly average climatology is not yet available.

Since cloud top temperature is the most indefinite parameter in calculating outgoing LW radiation, it is taken as an adjusting factor, as suggested by Thompson and Warren (1982), to match the current climate.

5.5.2 Compilation of Cloud Top Height and Cloud Top Temperature

According to the cloud region classification of Sherr _et al_. (1968), section 5.3, the cloud cover of each of the 29 cloud climatological regions is homogeneous. Table 5.1 also gives the general description of the cloud type for each region. Since each cloud type has its prevailing cloud top height, one can assume that in each region all the cloud top is at the same altitude, and then take the cloud top ambient temperature as the cloud top temperature T_c as was done by Hummel and Kuhn (1983) and Chahine _et al_. (1983).

To avoid generating more uncertainty, cloud top height is only assigned to the mandatory pressure levels, where the temperature field is written on the NCAR tape (see Chapter 3). Since there is scarcely any cloud sustained at 100mb, no cloud is assigned to this level. Also, very low level clouds are assigned to the midpoint between the surface and 850mb. Thus each cloud top is at one of the following levels: near surface, 850, 700, 500, 300 and 200mb. Seasonal variation of cloud top height is considered as well. Table 5.7 shows the cloud top level of each cloud type for each month. Determination of the cloud top level for each cloud region will be discussed in the following paragraphs. The temperature at this pressure level is taken as T_c, except for the near surface cloud where the mean temperature between the surface and 850mb is used.

An atlas of monthly OLWR is compiled as the reference for determining the proper cloud top height for each cloud type given in Table 5.1. Data used are from the scanning radiometer (SR) on board of NOAA satellites measured from June 1974 to February 1978 (Abel and Gruber, 1979). These data were further processed into $10^o x 10^o$ regions by Vonder Haar _et al_. (1982). This is the longest time series of satellite measurement from one single instrument. Data of the same month from different years are averaged to generate the 'monthly

Etages	*Polar Regions*	*Temperate Regions*	*Tropical Regions*
High	3-8 km (10 000–25 000 ft)	5-13 km (16 500–45 000 ft)	6-18 km (20 000–60 000 ft)
Middle	2-4 km (6 500–13 000 ft)	2-7 km (6 500–23 000 ft)	2-8 km (6 500-25 000 ft)
Low	From the Earth's surface to 2 km (6 500 ft)	From the Earth's surface to 2 km (6 500 ft)	From the Earth's surface to 2 km (6 500 ft)

Table 5.6 Classification of cloud height.

cloud type month	1	2	3	4	5	6	7	8	9	10	11	12	13	14	15	16	17	18	19	20	21	22	23	24	25	26	27	28	29
J	3	3	5	3	3	4	3	5	1	1	3	3	3	3	1	3	1	3	4	3	4	3	3	3	6	4	3	3	3
F	3	3	5	3	3	4	2	4	2	1	3	3	4	3	1	3	1	3	3	3	4	3	3	2	6	4	3	3	3
M	2	3	5	3	3	4	3	4	2	1	3	3	3	3	1	3	1	2	3	3	4	3	3	2	5	4	3	3	3
A	2	3	5	3	2	3	3	3	2	3	3	3	3	3	1	4	1	2	4	3	3	3	3	3	4	3	3	3	3
M	1	2	4	3	2	3	3	3	2	3	2	3	4	3	1	4	3	2	4	3	3	3	3	3	4	1	3	3	3
J	1	2	4	3	2	3	1	3	3	3	3	3	4	3	2	4	4	1	5	3	1	3	3	3	3	1	2	3	3
J	1	3	4	3	3	3	2	2	3	4	3	3	3	3	3	4	4	1	6	3	1	3	3	3	2	1	2	3	3
A	1	3	4	3	3	3	1	3	3	3	3	3	3	3	3	5	3	1	6	3	2	3	3	3	3	1	2	3	3
S	1	3	4	3	3	4	2	1	3	3	3	4	4	3	3	4	4	1	4	3	3	3	3	3	4	2	3	3	3
O	1	2	4	3	3	3	1	3	3	3	3	4	4	4	3	4	3	2	4	3	3	3	3	3	5	3	3	3	3
N	1	1	4	3	3	3	1	4	3	2	3	3	4	3	3	3	3	2	3	3	3	3	3	2	5	3	3	3	3
D	3	3	4	3	3	4	2	4	3	1	3	3	3	3	2	3	1	3	3	3	4	3	3	3	6	4	2	2	3

Table 5.7 Cloud top level index. 1, near surface; 2, 850mb; 3, 700mb; 4, 500mb; 5, 300mb and 6, 200mb.

average'.

To determine the cloud top level, a rough guess was first made by using the description of Sherr et al. (1968) for each cloud type, Table 5.1, and choosing the possible corresponding cloud height level from Table 5.6 from the International Cloud Atlas (1975). Thus, T_c can be found, then the cloudy sky OLWF is calculated. This result is compared with the reference atlas, cloud region by cloud region, and the cloud top level can be adjusted to the upper level or the lower level in order to minimize the difference between the reference atlas and calculated OLWF. This procedure is iterated until the difference is minimal for each cloud region, and the best cloud top height is thus defined. Table 5.7 tabulates the pressure level where the cloud top is located, and is the result of this procedure.

Examining Table 5.7, one finds that cloud climatological regions have seasonal variation of cloud top height. The most drastic one is Region 25, located at the southern tropics over South America, Africa and Indian Ocean, where the cloud top level changes from 200mb in January to 850mb in July. The range of the seasonal variation of cloud top height is about 200mb to 300mb for most other cloud regions.

There are as well many regions where their cloud top height stays fairly constant throughout the year, such as region 3 at the tropical Pacific and the northern part of the South America; Regions 19 and 29, where subtropical oceans are located; Regions 14 and 23 of the high latitude ocean; Region 11, mid-latitude land in the Northern Hemisphere; Region 23, mid-latitude ocean in the Southern Hemisphere and Region 28, the subtropical land at the southeast parts of both Australia and South America.

Figures 5.8 and 5.9 show the contour of cloud top temperature for January and July respectively. It is clear that the cloud region classification of Sherr et al. (1968) highly modulates this result. In January, the main low cloud top temperature regions are located at the west coast of the United States, Siberia, equatorial Pacific and Atlantic, northern South America and African Congo. High cloud top temperature regions are Australia, west coast of Central America, west coast of South Africa, monsoonal India and West Europe. In July the main low cloud top temperature regions are located at the eastern United States, Caribbean Sea, southeast Pacific, East China, and monsoonal India. High cloud temperature regions are located at North and South Africa, southern Indian Ocean, west coast of the United States and eastern South America.

As mentioned in the previous section on cloud top level, the regions with strong seasonal variation are South America south of the equator, monsoonal India, and South Africa. Other regions also have seasonal variation, but nevertheless, are more moderate.

5.5.3 Comparison with Satellite Observation

As was done for the clear sky OLWR case in section 4.6, the compiled T_c is compared with satellite data analyzed by Minnis and Harrison (1984, hereafter denoted as MH) for the region from Longitude, 30°W to 125°W, latitude 45°N to 45°S for November. These results are shown in Figure 5.10 and 5.11.

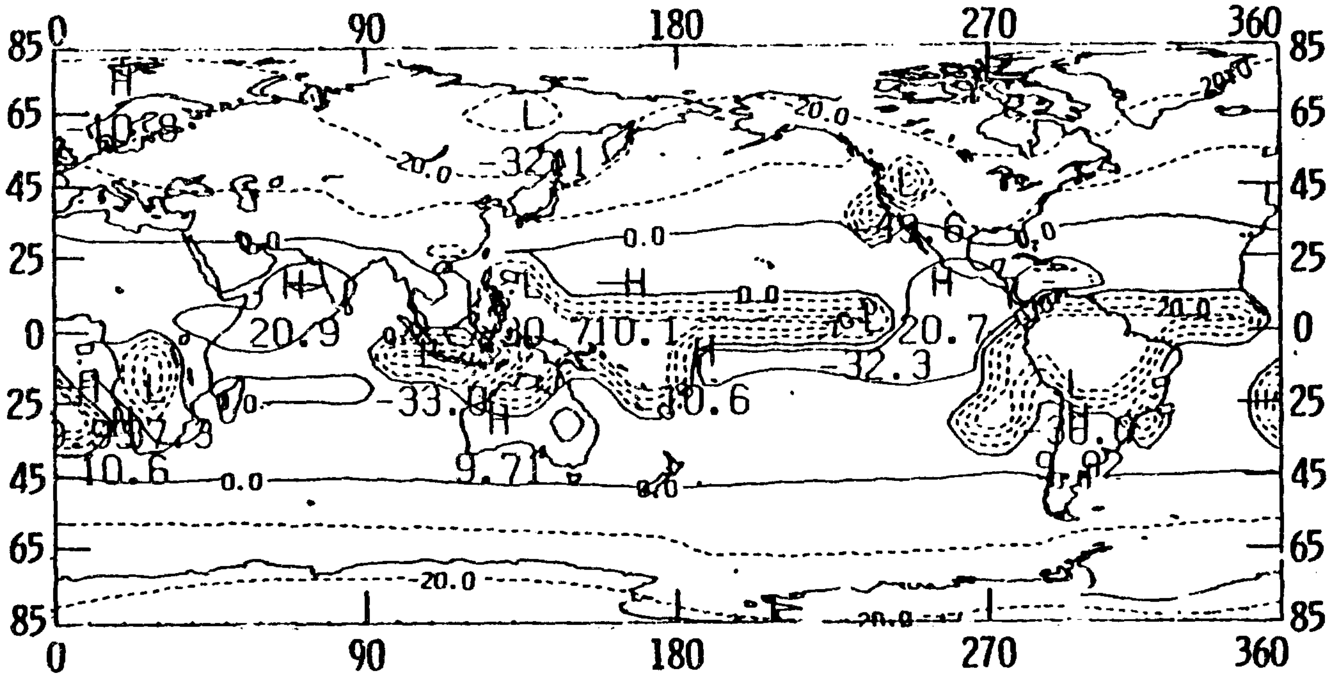

Figure 5.8 T_c map for January, in °C.

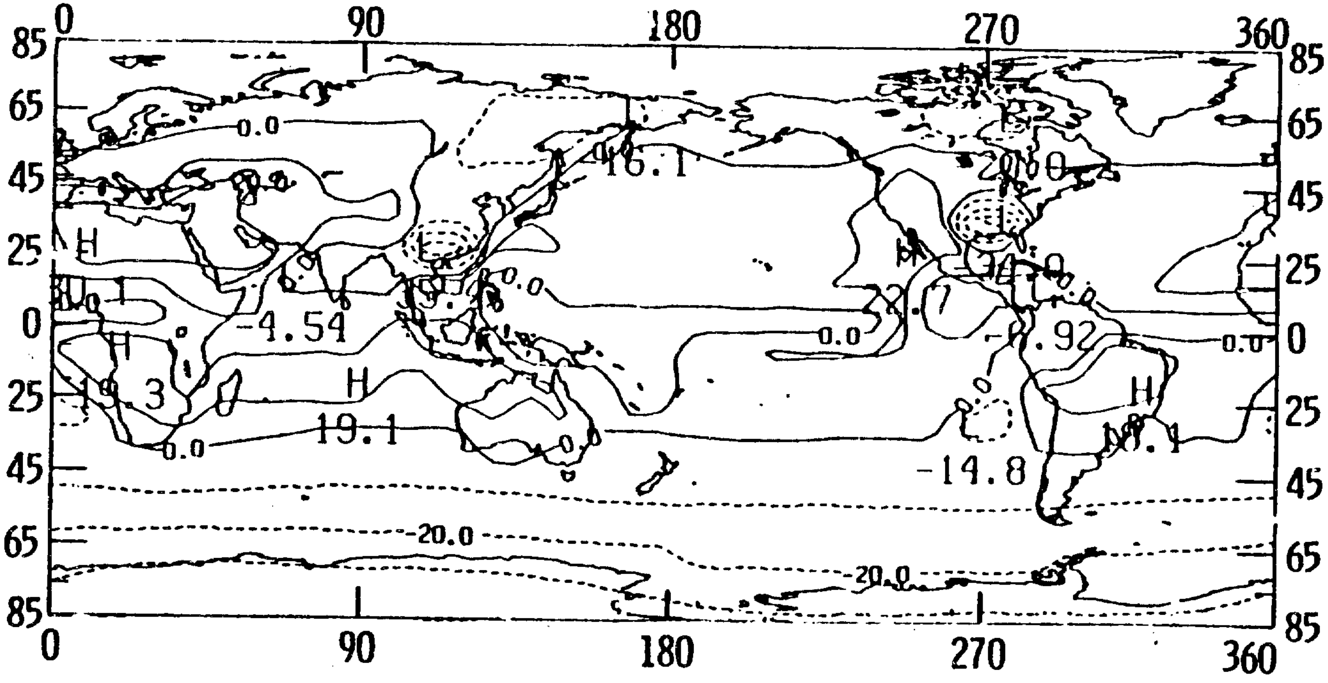

Figure 5.9 T_c map for July, in °C.

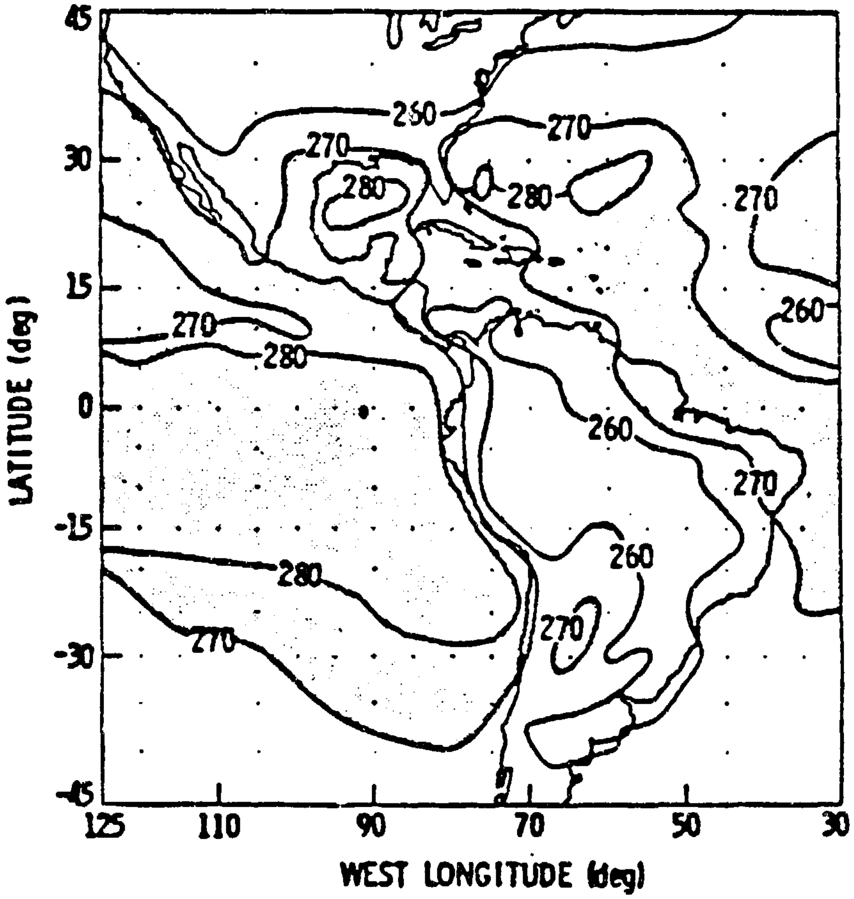

Figure 5.10 GOES regional T_c for November, 1978 after Minnis and Harrison (1984), in °K.

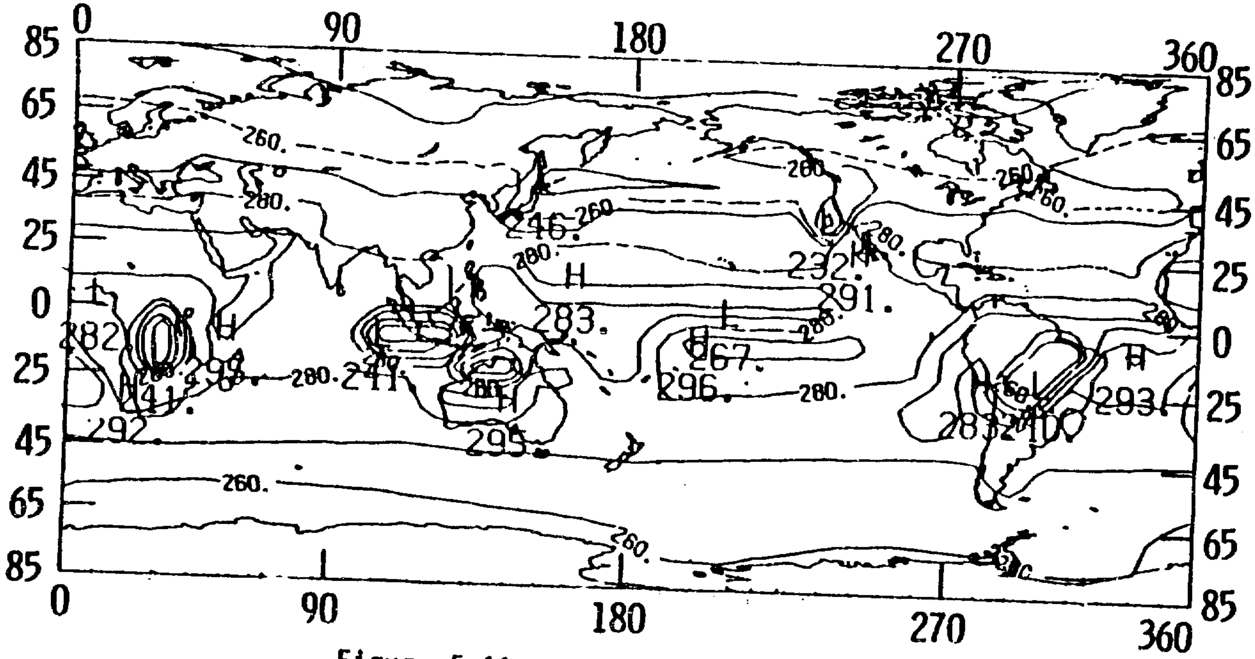

Figure 5.11 T_c map for November, in °K.

The locations of the region of the low T_c center at central South America and the adjacent high T_c regions both to the east over Atlantic and to the west over Pacific are well simulated. However, the magnitudes differ. In our compilation the maximum temperature is 294°K over the Atlantic versus 270°K of MH; the minimum is 240°K for the Central South America, while MH has 260°K. At the Atlantic coast of South America, where the compiled data are higher, the reason for the difference might be that the NOAA data has higher OLWR at this region, 282 W/m^2 vs. 270W/m^2 for MH. The other possibility is that MH measured T_c using a window channel which could be contaminated by the tropical water vapor absorption, thus underestimated. Over Central America, the compilation data is lower. This could possibly be explained as follows: our clear sky OLWR case in this region is about 10W/m^2 higher than that of MH, which means the height weighted mean relative humidity $\underline{RH}$ could have been underestimated at this region. Therefore, to fit the normal cloudy sky OLWR from NOAA data, cloud must be adjusted to higher level in order to offset the low $\underline{RH}$, thus resulting in lower T_c. Still, this magnitude is in the reasonable range. Comparing with other observations, Curran and Wu (1982) used Skylab-observed data and found T_c can be as low as 226°K in New Mexico area. This somewhat justifies our T_c compilation.

5.6 Summary

Clouds have two competing effects on climate: cloud albedo effect and greenhouse effect. Most observation shows that cloud albedo effect dominates. However, the result is sensitive to the analysis techniques and the data used. Since these cloud effects are highly dependent on the cloud type and cloud height, this problem can be very localized. Apparently, further study on this subject is needed for its great importance on the earth radiation budget. On the large scale, satellite observations show that clouds possess certain stability or repetitiveness over an entire season, which render the feasibility of constructing cloud models, such as Sherr _et al_. (1968) incorporated in this study. Some techniques of cloud observations are reviewed.

The Sherr _et al_. (1968) cloud model classifies the globe into 29 homogeneous cloud cover regions. A set of monthly cloud cover maps is derived from this model with an adjusting parameter GLCLC introduced by Bartman (1980) for fitting the nominal global annual averaged cloud cover. A value of 45 is selected for current study. The zonal averaged results are compared with London (1957) and van Loon (1972) with fair agreement. It is expected that the future result of ISCCP and Warren _et al_. would greatly improve our understanding of cloudiness.

A set of cloud top temperature maps are compiled using the cloud region classification of Sherr _et al_. (1968) and with the aid of the LW radiation measurement by NOAA scanning radiometer. A November regional result is compared with Minnis and Harrison (1984) with good agreement.

CHAPTER 6

CLOUDY SKY OUTGOING LONGWAVE RADIATION

This Chapter presents the results of the cloudy sky outgoing longwave radiation (OLWR) calculated from the scheme developed in this study as described in the previous chapters. In section 6.1, the global averaged OLWR variation with season is discussed. In section 6.2, the zonally averaged OLWR for January and July, as well as the temporal zonal variation are discussed. In section 6.3, the global distribution of OLWR for January and July are discussed in detail from region to region.

6.1 Global Average OLWR

Global monthly average cloudy sky OLWR calculated from the model (CD), clear sky OLWR (CR) and reference OLWR compiled from NOAA scanner radiometer (NOA, see section 5.5.2), are tabulated in Table 6.1. A summary of other parameters are also included.

The global average manifests the general performance of the model and also shows the mean state of the earth climate. There is good agreement between CD and NOA, with CD very slightly overestimated with an annual average of 245.6 and 244.7 W/m^2 for CD and NOA respectively. The differences are smaller than 1.5 W/m^2, about 0.6%, except for November, which differs by about 1%. The difference of the annual averages is about $0.9w/m^2$. As both cloudiness and mean relative humidity hold very steady throughout the year, at about 45% (after multiplied by GLCLC/60) for CD and and 47% for <u>RH</u>, the major parameters contributing to the seasonal variation are the change of surface temperature (T_s) and the temperature difference between the cloud top and the surface (T_s-T_c). From Table 6.1 it is clear that both of these factors contribute to the maximum OLWR at the northern hemispheric summer, June through August. However, these two parameters are also slightly out of phase; T_s has a maximum at July, while T_s-T_c has a minimum in May, with the result that June has the highest OLWR. Comparing CR with CD, on the average, clouds contribute about $10w/m^2$, or 4%, in reducing OLWR.

To illustrate the seasonal variation, CD and NOA are plotted on the climatology by Campbell and Vonder Haar (1980, denoted as CV) on Figure 6.1. The difference between CV and NOA will be discussed later. The seasonal cycle of OLWR is in phase with the season of the Northern Hemisphere with an amplitude of about 5 W/m^2. The two prime factors affecting this seasonal variation are (1) Earth-Sun distance and (2) different amounts of land-sea distribution in the Northern Hemisphere and the Southern Hemisphere. Since the Earth-Sun distance is shortest in December, in the northern hemispheric winter, the factor of the land-sea distribution must dominate in order for the OLWR variation seasonal to be in phase with the northern hemispheric seasons.

Although seasonal OLWR has a maximum in the Northern Hemisphere

Table 6.1 Global average OLWR parameters.

		JAN	FEB	MAR	APR	MAY	JUN	JLY	AUG	SPT	OCT	NOV	DEC	ANNUAL
CR	(W/m^2)	252.6	253.1	254.0	255.6	257.6	259.5	260.1	260.0	258.7	256.5	254.2	252.8	256.2
CD	(W/m^2)	240.7	241.8	243.1	244.85	248.3	249.4	249.5	249.1	247.3	245.5	244.6	242.4	245.6
NOA	(W/m^2)	239.8	240.4	242.6	244.9	247.3	249.8	249.5	248.7	246.6	244.0	242.3	240.9	244.7
T_s	(°C)	12.10	12.35	12.90	13.92	14.85	15.58	15.96	15.75	15.14	14.13	13.12	12.40	13.99
T_c	(°C)	-6.01	-5.69	-4.77	-3.71	-.17	.29	-.17	-.62	-2.03	-3.10	-1.90	-3.37	-2.58
T_s-T_c	(°C)	18.63	18.53	17.57	17.51	14.96	15.24	16.21	16.45	17.14	17.23	15.00	16.31	16.71
A_c		.60	.59	.59	.60	.61	.62	.61	.61	.61	.60	.63	.63	.60
RH		.47	.47	.47	.47	.46	.46	.47	.46	.46	.47	.47	.47	.47

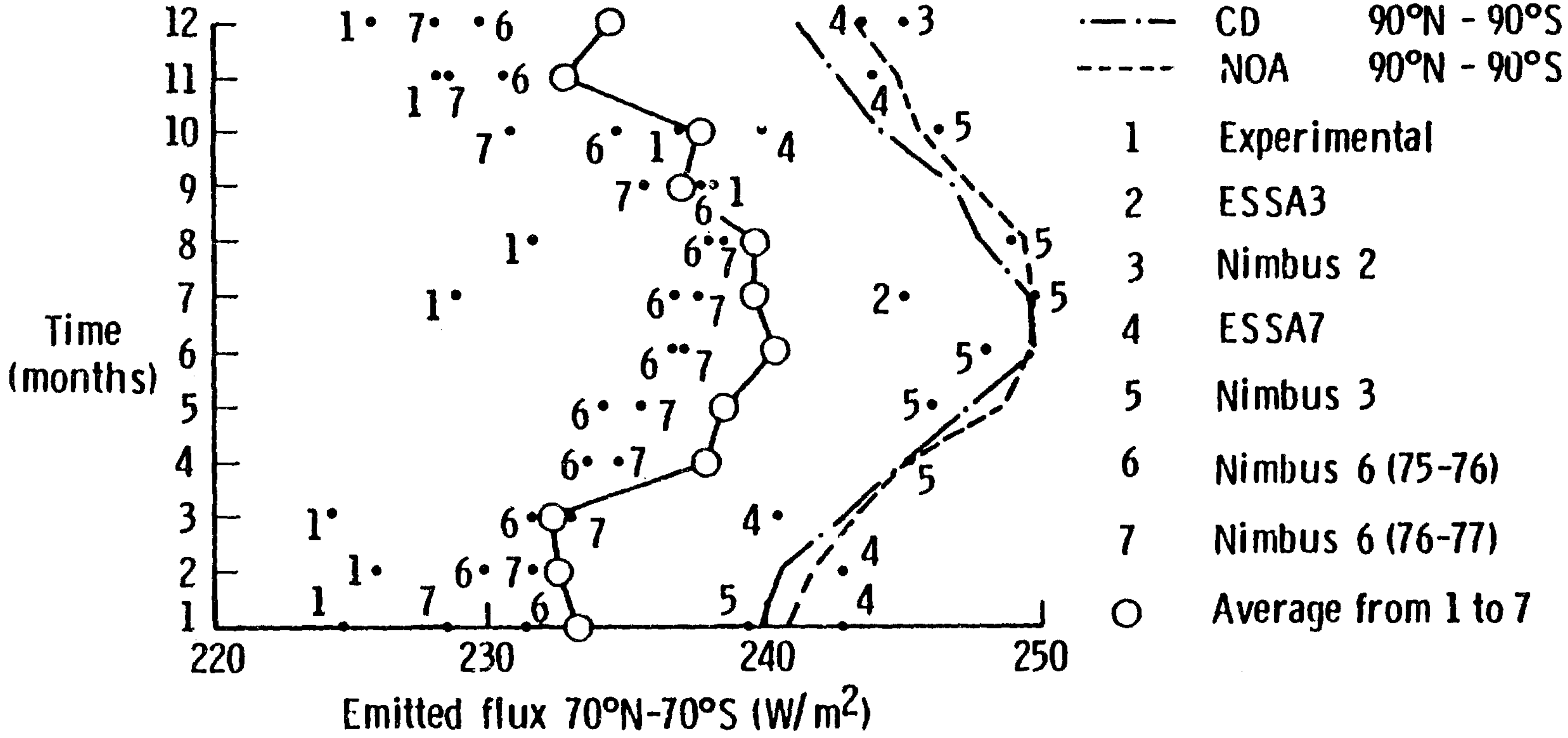

Figure 6.1 Experiment comparison of monthly global average OLWR. Experiment 1 through 7 and O are from Campbell and Vonder Haar (1980).

summer and minimum in the Northern Hemispheric winter, the exact timing of the occurence for these extremes varies very substantially from year to year. A recent observation of Nimbus 6 and Nimbus 7 from July 1975 to October 1980 by Bess (1984, personal communication) is shown on Figure 6.2. Disregarding an instrument calibration shift and missing data, the minima can occur from November to February and the maxima from July to August. NOA and CV, however, have maxima at June. The significance of this minor variation of OLWR to the climate can be interpreted in terms of net radiation, which is the difference between the two large values of OLWR and the absorbed radiation. An 1 w/m^2 net radiation flux would change the temperature of a 100m deep ocean layer about $0.1^{o}K$ each year (Campbell and Vonder Haar, 1980). Diagnosing the timing of the hemispheric mean OLWR extremes might thus provide significant clues in the long range weather forecast.

NOA is estimated by using an empirical formula which relates the observed radiance of the 10 μ m window channel to the OLWF. A theoretical radiative transfer calculation, rather than observation, is used to derive this empirical formula. A recent investigation by Ellingson and Ferraro (1983) found that this operational technique systematically overestimates OLWF when the technique is applied to the radiance from areas with partial cover of high or middle spectrally black cloud. Thus global NOA is about 8 W/m^2 higher than that of CV. For our study, this systematic over-estimation can possibly lead to an under estimation of the effect of cloud. A simple method to alleviate the difference between CD and the nominal OLWF

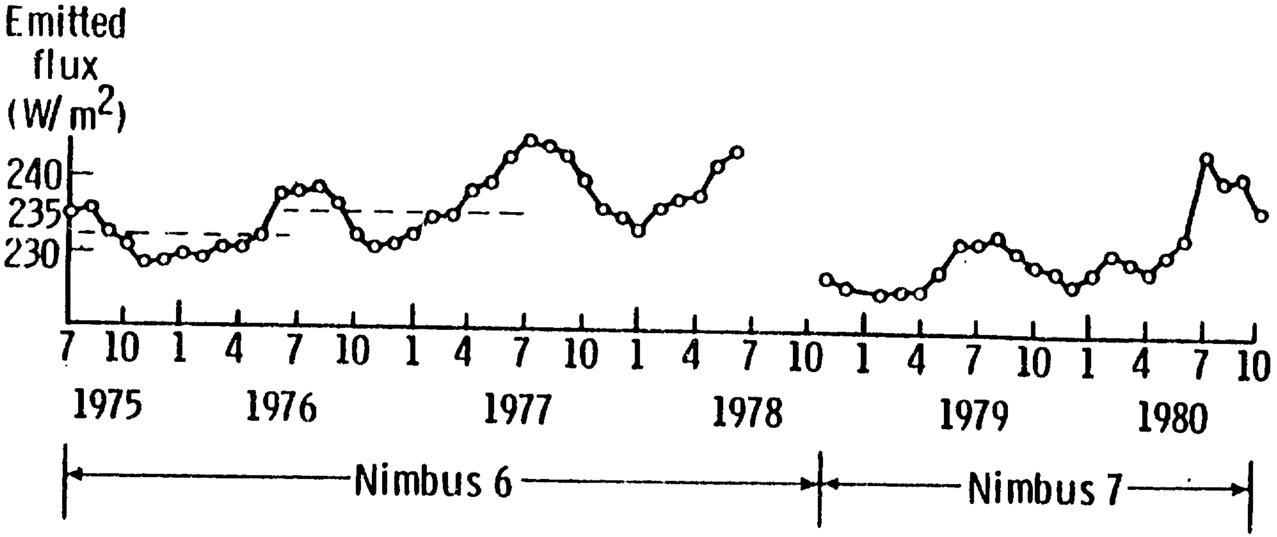

Figure 6.2 Time history of global average OLWR measured by Nimbus 6 and 7. (Courtesy of T. D. Bess)

is by adjusting GLCLC. However, for the analysis, the temporal and spacial variations, as well as CR are not influenced.

6.2 Zonally Averaged OLWR

Figures 6.3 and 6.4 show the calculated zonally averaged CD for January and July respectively. CR and NOA are also plotted on the figures for comparison.

The typical zonally averaged OLWR pattern, a minimum at the tropics and two maxima at the subtropics with negative gradient from the maximums toward the poles, are well reproduced. The general difference between NOA and CD are within 3.5% depending on the latitude, except at the antarctic and the minimum at the equator. The higher differences in these regions will be futher discussed later. The magnitude of the maximum at the subtropics is about 265 to 275 W/m^2, which is about 25 W/m^2 higher than that of the minimum at the tropics. As discussed in Chapter 4 higher water vapor concentration at the tropics is one of the major contributor to this minimum. As well, in the window region, the e-type continuum absorption is significant (Warren and Thompson, 1983). From the difference between CD and CR, it shows that cloud and *RH* make equivalent contributions to this minimum, which accounts for more than $20W/m^2$ reduction from CR. One of the major cloud regions in this latitude according to Sherr *et al.* (1968) is cloud region 3, which includes 19 out of the 36 grids at this latitudinal belt. Table 5.1 reveals that the cloud top temperature at this region is much lower than that of the adjacent subtropics. The clouds are at higher altitude, 500mb level,

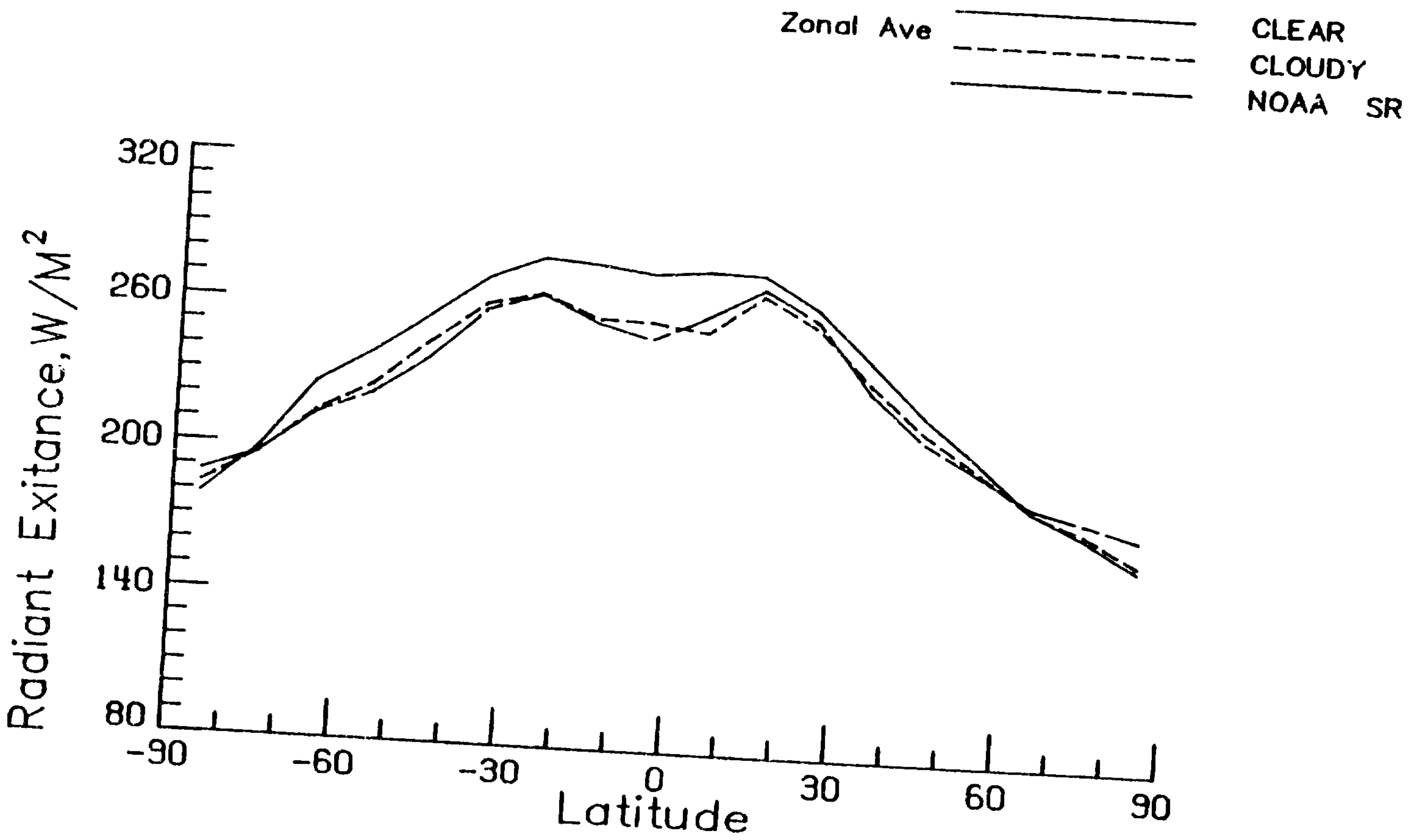

Figure 6.3 Zonally averaged CD, CR and NOA for January.

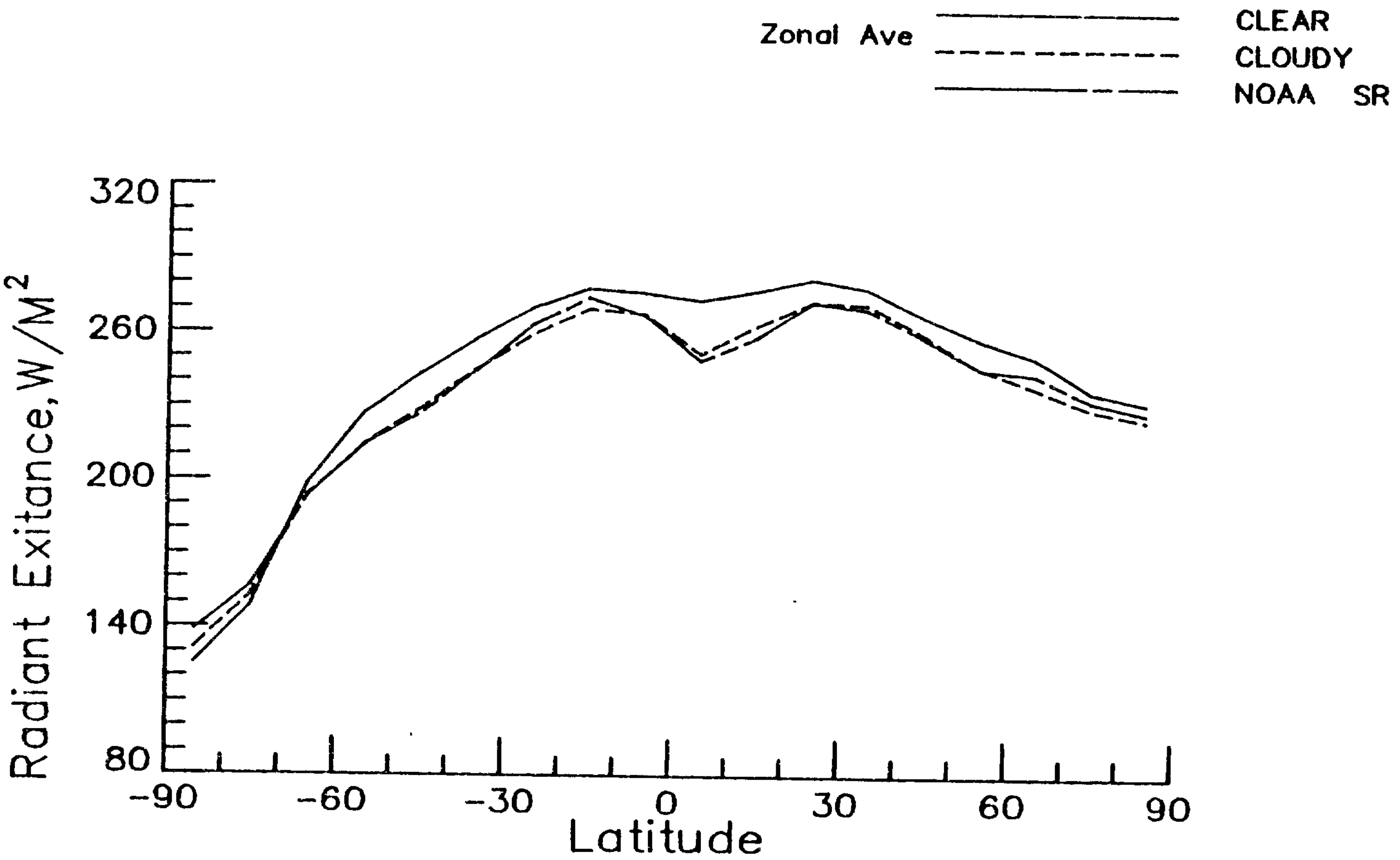

Figure 6.4 Same as figure 6.3, but for July.

compared to 700mb or lower in the neighborhood, while the cloud cover changes of the adjacent latitudes are only less than 10%, thus the dominant effect in reducing OLWR is the colder cloud top temperature and high water vapor concentration.

At the subtropical maxima, the magnitudes of OLWF are about 270 W/m^2 with the winter hemisphere slightly higher than that of the summer hemisphere, by less than 5 W/m^2. This is due to stronger convection in the summer hemisphere. The difference between NOA and CD is smaller than 2.5%, about 5 W/m^2. Both the OLWR maxima and the minima have significant seasonal variations. The locations of the maxima, which are associated with the subtropical high pressure systems oscillate about 10 to 15 degrees north-south following the sun's position. The maximum in the Southern Hemisphere has smaller displacement than that of the Northern Hemisphere. The larger ocean heat capacity in the Southern Hemisphere stablizes this variation (see Figure 6.3). The minimum, which is associated with the ITCZ, has less seasonal variation than the maximum, From the observation, the ITCZ is essentially located to the north of the equator except in January and July. Still, in the CD case, the displacement of this minimum is less than that of NOA. This discrepency is mainly due to the fixed cloud region classification of Sherr _et al_. (1968) (see Figure 5.1), which is not seasonal dependent.

There are larger differences between CD and NOA in the polar regions, about 6%, or 6 to 10 W/m^2 depending on the latitude, which is much higher than that of mid-low latitudes. Recall from the clear sky OLWR discussion in Chapter 4 that in the polar regions the temperature is much lower and the OLWR is much less sensitive to the relative humidity. From Figures 4.7 and 4.8 we show that CR compared best with the other experiments at the polar region, thus the difference in the cloudy sky case between CD and NOA is predominantly from the effect of cloudiness and cloud top temperature. Since these are the places where there are strong surface temperature inversions, extending up to higher than 700mb, the effect of inserting a cloud deck in the inversion is to increase OLWR. As shown in Figures 6.1 and 6.2, the difference between CD and NOA increases with latitude, which is opposite to the clear sky case. The reason for this feature is that to minimize the error in compiling cloud top temperature (see section 5.5), each grid value has been weighted with area, such that the globally averaged OLWR can be more accurate. In cloud Region 24, as well as region 15 at the north pole which extend from 65°S to 85°S, the weighting of 65°S is cos(65°), about .42, which is higher than the sum of the weighting of 75° and 85°, .25 and .09 respectively. Thus the cloud top temperature is predominantly determined at the latitude of 65°S, so that we have very small difference at 65°S between CD and NOA and the difference increases toward the poles where there is less weighting.

Zonal Temporal Variation

To illustrate time-space variation, a series of time-latitude contours of T_s, RH, CR, cloud cover, CD and NOA are plotted.

Figure 6.5 shows the time history of zonally averaged climatological T_s. The most significant feature is the asymmetrical seasonal

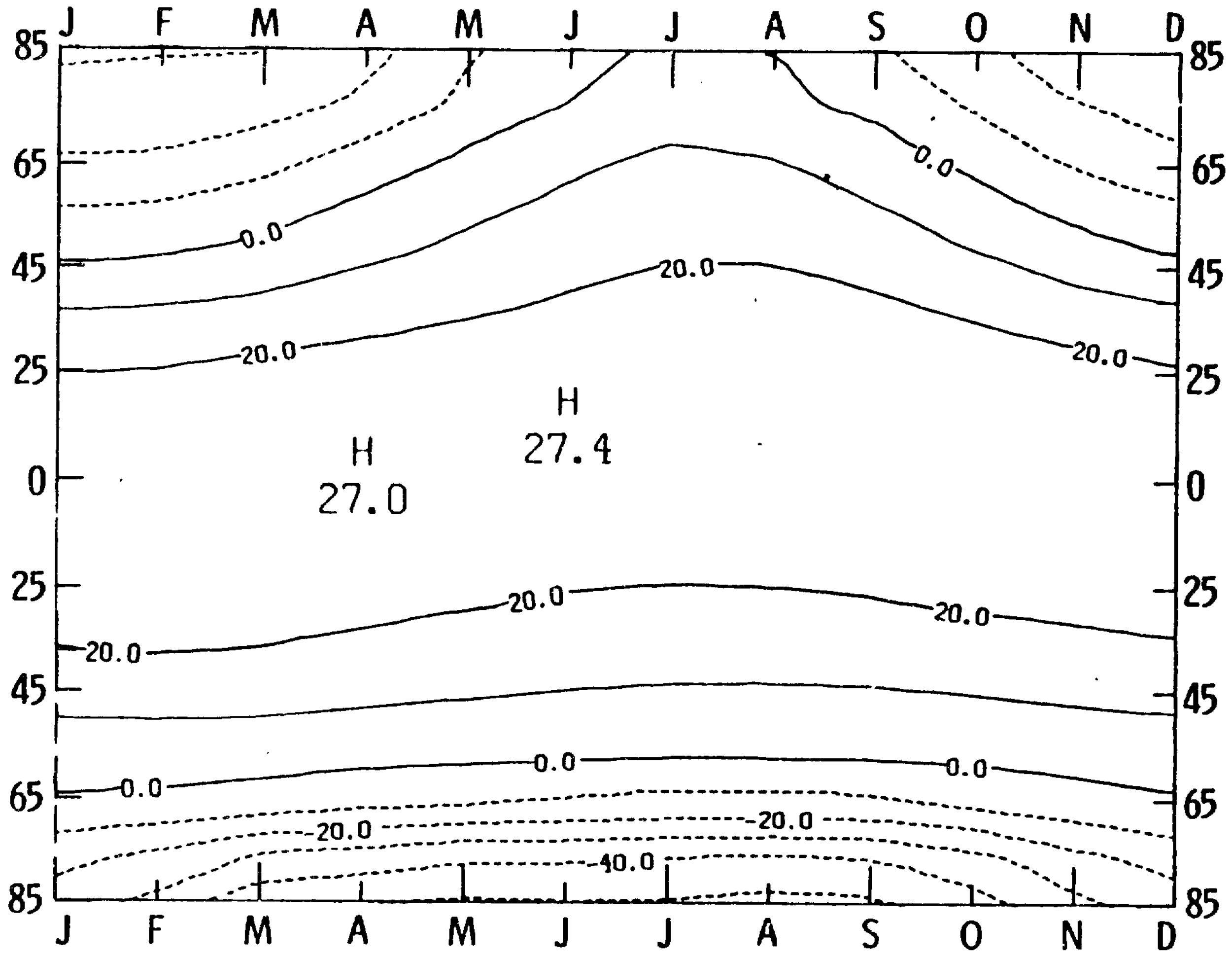

Figure 6.5 Time history of zonally averaged T_s.

variation between the two hemispheres. The strong annual cycle at the Northern Hemisphere is due to the large continent distribution which contributes rapid heating and cooling, while in the Southern Hemisphere large ocean heat capacity evens out most of the annual cycle. In the tropics, the temperature variation is basically non existent due to constant solar duration.

Figure 6.6 shows the time history of zonally averaged $\underline{RH}$. Essentially $\underline{RH}$ varies in a very small range, from 0.4 to 0.6 for most of the time and space. Higher values in the tropics and lower values in the subtropics are well defined; it is evident that the contours follow the sun's position.

Figure 6.7 shows the time history of zonally averaged CR. It is clear that CR has a pattern pretty similar to that of the T_s except in the tropics and subtropics, where the surface temperature is sufficiently high. Thus the variation of $\underline{RH}$ modulates CR in the low latitudes. The difference between the maximum in the tropics and the minimum in the subtropics is about 10 W/m^2.

Figure 6.8 shows the time history of zonally averaged cloud cover. Although there is similarity between the cloud cover and $\underline{RH}$, especially in the southern hemisphere, the cloud cover pattern is less smooth and spreads over a larger range, 0.4 to 0.8, over the globe. The very low value of 0.4 in the Antarctic winter is quite questionable.

Table 6.2 tabulates the time history of zonally averaged T_s-T_c. The corresponding figure is on Appendix A.17. The tropical regions have the highest T_s-T_c difference, due to strong convective activity.

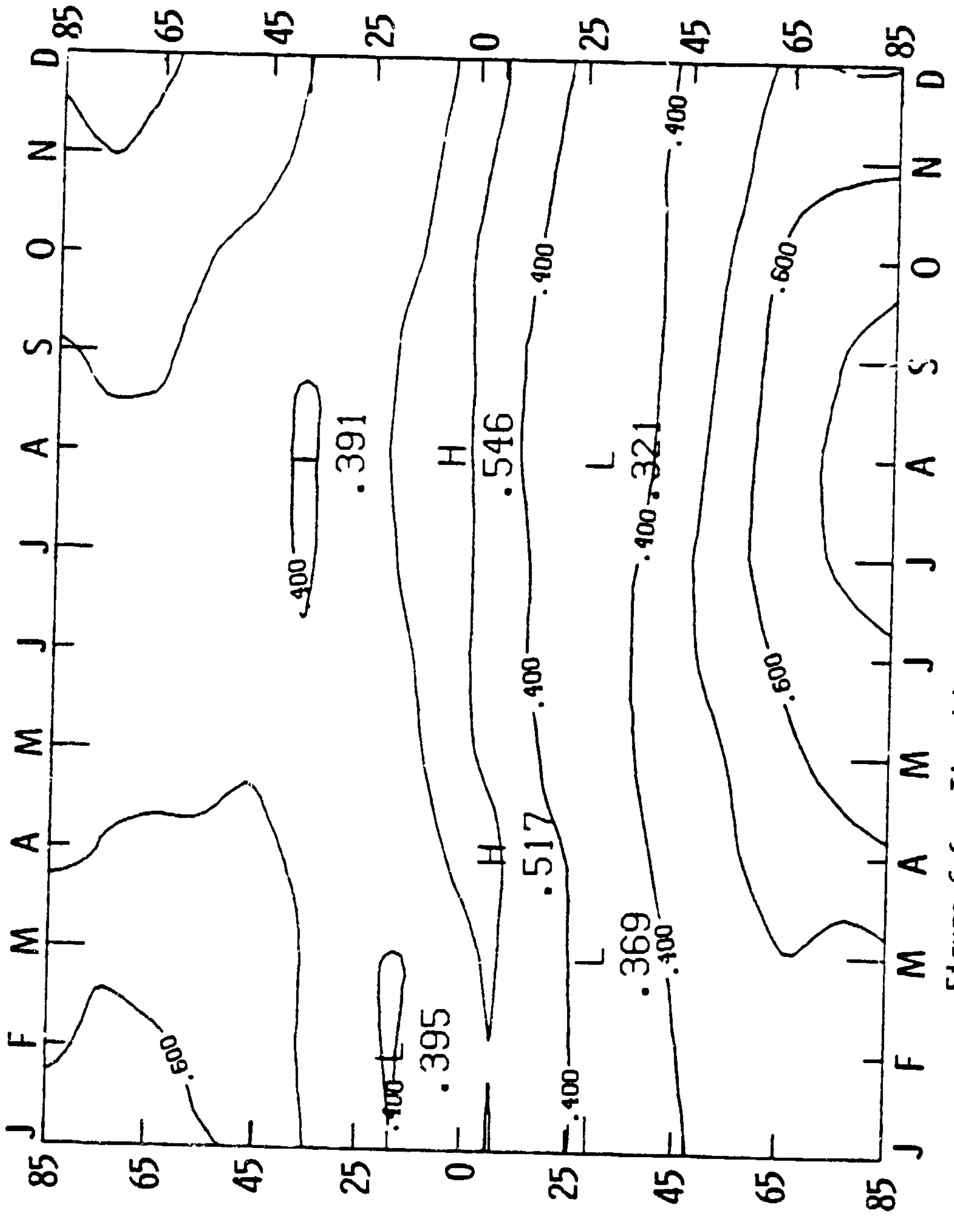

Figure 6.6 Time history of zonally averaged RH.

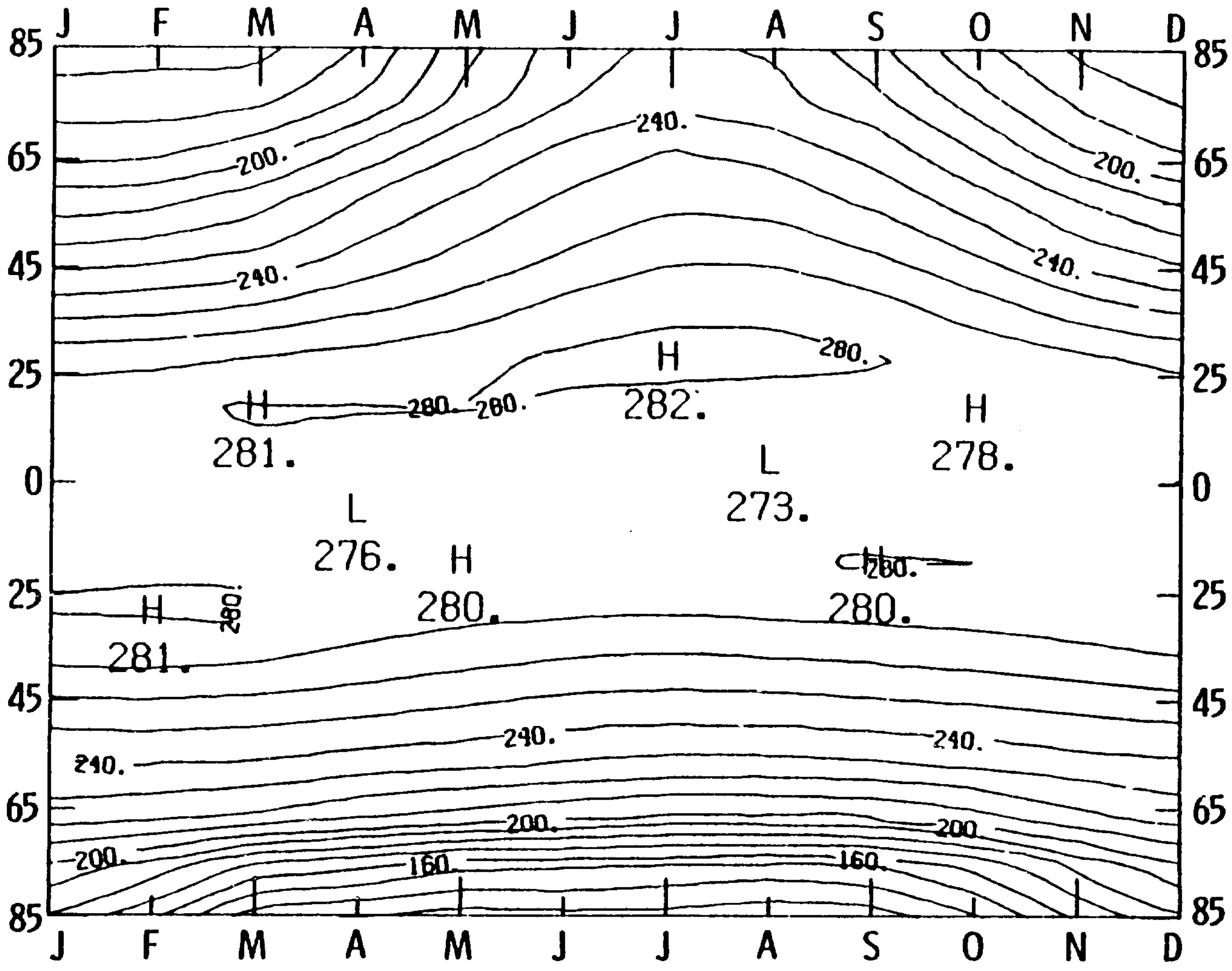

Figure 6.7 Time history of zonally averaged CR.

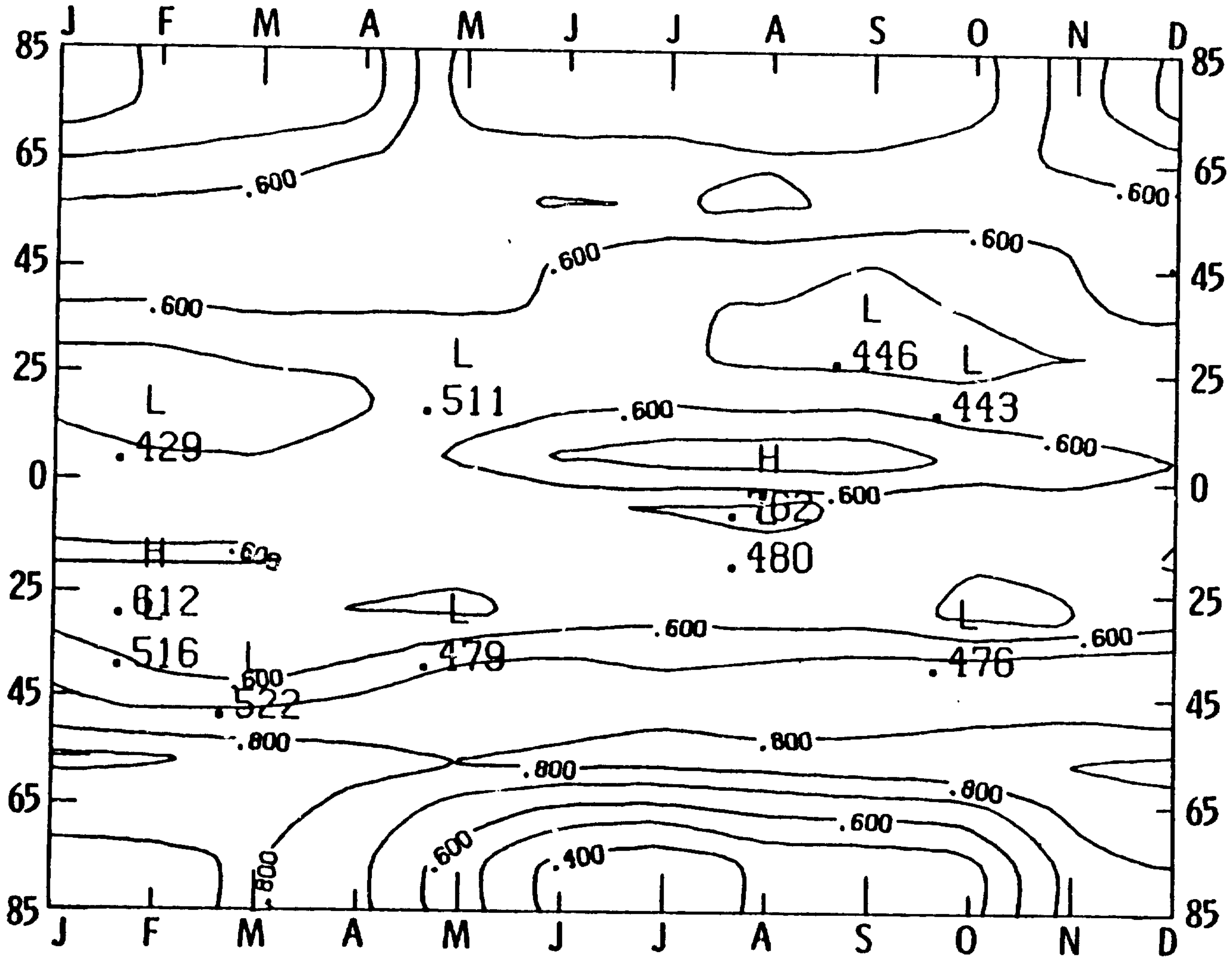

Figure 6.8 Time history of zonally averaged Ac.

LAT.	JAN	FEB	MAR	APR	MAY	JUN	JLY	AUG	SPT	OCT	NOV	DEC	LAT.
85	-4.2	-3.2	-3.3	-2.6	.4	2.9	9.1	9.1	7.8	3.7	.3	-5.2	85
75	-2.6	-2.5	-2.4	-1.2	.8	2.7	9.5	9.9	10.4	7.2	2.8	-4.0	75
65	0.10	- .7	1.7	5.9	7.8	12.9	16.8	13.6	13.1	13.3	5.0	2.2	65
55	5.5	5.2	7.6	11.0	10.0	14.3	15.9	14.3	14.1	18.4	9.7	7.1	55
45	10.5	17.1	11.2	13.0	16.4	17.6	13.7	12.6	18.6	17.8	16.8	10.1	45
35	14.6	15.2	12.7	13.8	12.8	13.2	16.8	15.7	14.8	14.0	12.1	13.6	35
25	14.6	14.0	13.4	15.6	14.3	15.2	17.8	19.7	16.4	15.1	11.4	14.0	25
15	15.3	15.7	16.3	18.1	16.4	19.1	21.8	21.0	24.8	19.7	14.4	14.5	15
5	37.7	38.1	38.2	41.1	27.1	27.2	27.6	31.5	27.8	27.5	24.2	24.4	5
-5	37.0	37.3	33.7	28.4	20.7	17.6	17.7	19.1	22.2	25.1	24.0	31.3	- 5
-15	33.5	33.6	30.7	22.7	18.4	14.3	13.4	14.9	19.1	23.4	23.6	30.6	-15
-25	23.1	23.3	23.1	21.5	16.0	15.7	16.6	16.4	16.6	16.6	16.7	19.6	-25
-35	15.0	15.0	15.2	15.5	16.2	15.9	16.5	16.2	16.2	15.7	15.5	14.1	-35
-45	14.1	13.7	13.9	14.5	15.3	16.0	16.5	16.4	16.1	15.1	14.8	14.6	-45
-55	14.0	13.5	13.8	14.2	14.5	14.7	14.7	14.6	14.9	14.6	14.8	14.1	-55
-65	12.9	7.6	7.3	6.1	5.4	8.3	7.3	7.3	8.3	9.9	7.6	12.7	-65
-75	3.9	-7.3	-10.7	-12.5	-13.4	-10.0	-10.0	-11.0	-10.3	-7.5	-7.8	3.4	-75
-85	2.7	-13.4	-18.7	-18.5	-16.2	-17.4	-15.0	-18.0	-19.3	-17.0	-12.5	-3.7	-85

Table 6.2 Monthly zonal T_s-T_c in °C.

It is also clear that the convective activity follows the position of the sun. Although the rate of change of T_s-T_c is small in the mid latitudes, where most areas are between 10 and 20 ^oK, the annual variation is strong in the Northern Hemisphere and practically nonexistant in the Southern Hemisphere. Surface temperature inversions are constant in Antarctic and polar night time.

Figure 6.9 shows the time history of zonally averaged CD, and NOA is plotted on Figure 6.10 for comparison. The model results CD agree well with satellite observation NOA, both in magnitudes and the contour pattern. Again, basically the feature of CD can be decomposed into two parts: in the high latitudes it is the same as that of T_s and CR, and in the low latitudes it is modulated by $\underline{RH}$ and cloud cover. Comparing CD and CR reveals one interesting feature that cloud reduces OLWR very homogeneously, about 10 W/m^2, for all the latitudes but the tropics, where the influence of cloud is much stronger, up to 25 W/m^2. The asymmetric seasonal variation of the two hemisphere is not influenced by introducing cloud. Table 6.4 shows the global averaged OLWR reduced by increasing GLCLC from .45 to .60 for July case. As for water vapor, cloud has strongest reducing effect of OLWR in the tropics. Still only the magnitude of OLWR is reduced, the pattern of the contour from CR to CD is not significantly changed.

This feature again stress the importance of the water vapor in modulating OLWR, especially in the tropics. Also this suggests a new LW parameterization of the type $F = a + bT_s + c\,\underline{RH}$ as relative humidity is highly correlated with cloudiness. A parameterization of

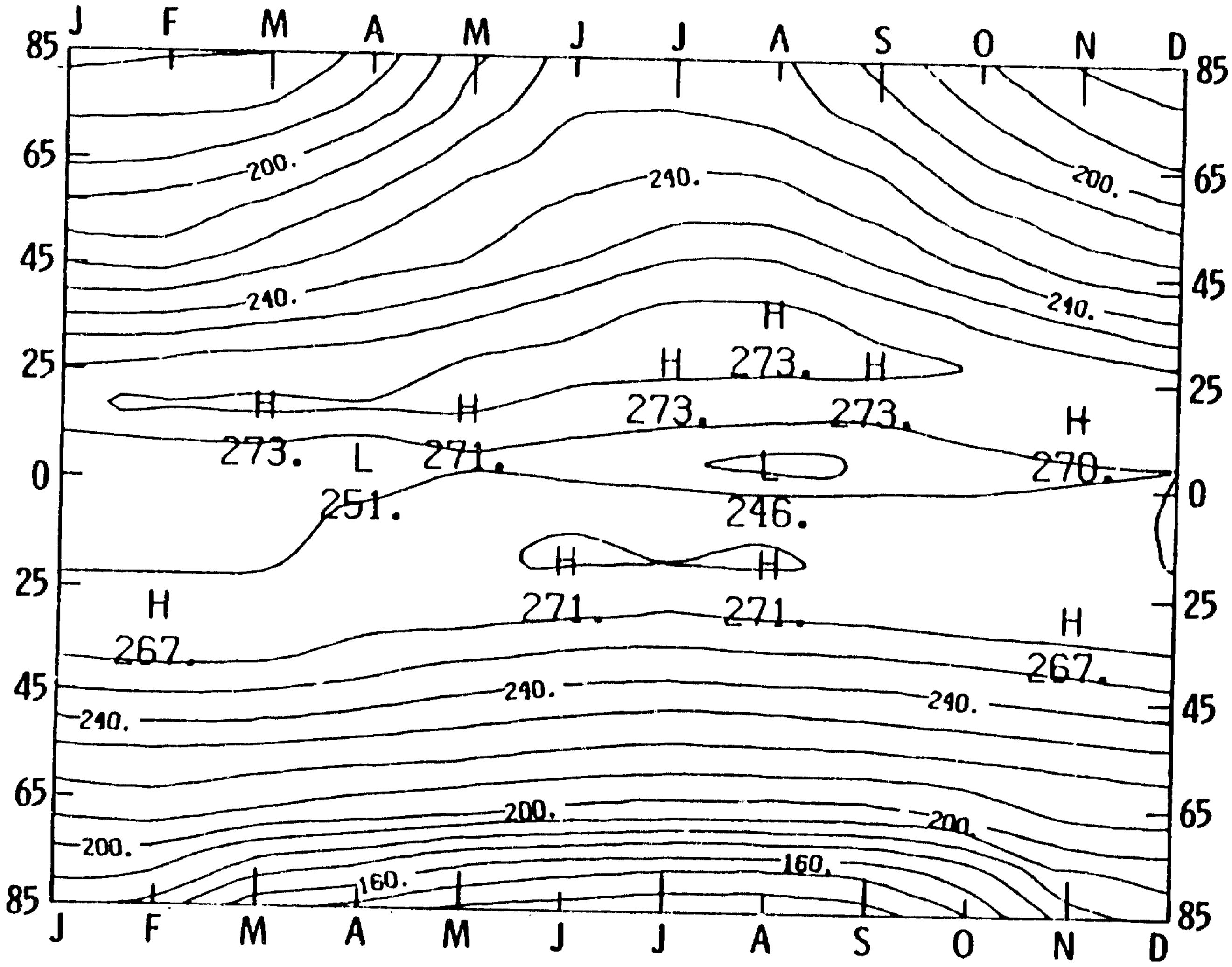

Figure 6. 9 Time history of zonally averaged CD.

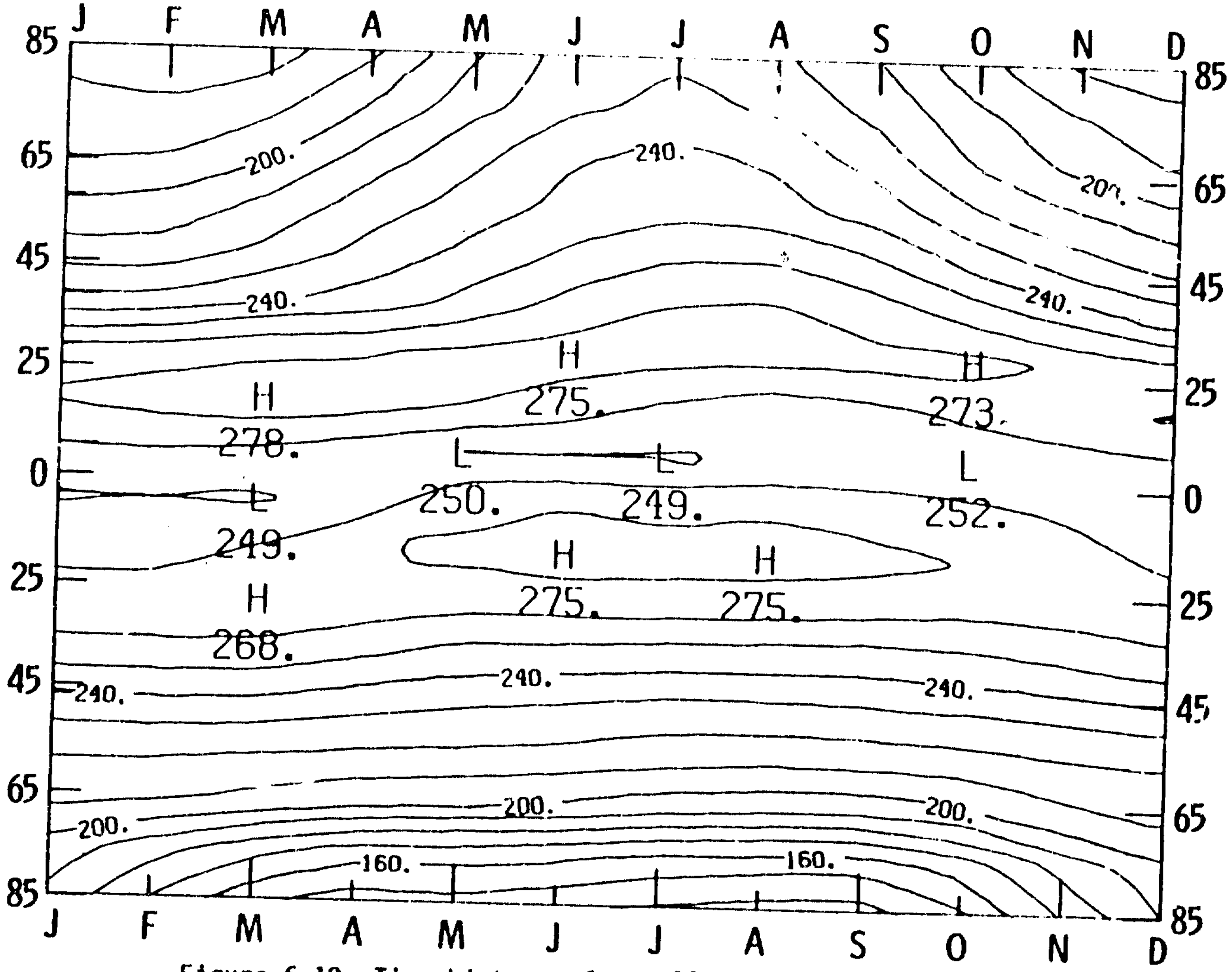

Figure 6.10 Time history of zonally averaged NOA.

	CD w/m^2			
	GLCLC		Difference	Percentage Difference
Latitude	0.45	0.60	w/m^2	%
85	225.53	223.26	-2.2	-1.0
75	229.94	227.59	-2.4	-1.0
65	238.56	234.46	-4.1	-1.7
55	246.27	242.44	-3	-1.2
45	260.03	256.92	-2.5	-1.0
35	272.32	267.15	-2.7	-1.0
25	273.43	269.73	-3	-1.1
15	263.27	259.91	-4.3	-1.6
5	251.96	245.08	-7.1	-2.8
- 5	268.06	264.93	-2.8	-1.0
-15	270.09	267.75	-2.6	-1.0
-25	259.37	256.14	-3.0	-1.2
-35	245.12	240.95	-4	-1.6
-45	228.95	224.25	-4.2	-1.8
-55	214.18	209.93	-4	-1.9
-65	193.72	192.20	-1.7	-0.9
-75	153.14	154.63	+1.5	+1.0
-85	131.54	133.49	+2.1	+1.6

Table 6.3 Zonally averaged July CD with GLCLC equal .45 and .60.

this type may improve the performance of a North-type climate model in the tropical region.

6.3 Global Distribution of OLWR

CD for January and July are shown in Figures 6.11 and 6.12. Also, for comparison NOA results for January and July are shown in Figures 6.13 and 6.14 respectively. The direction of the discussion on the OLWR features will start from the north polar region at the zero degree longitude and going west for each latitudinal zone.

There is good agreement between CD and NOA. The major synoptic scale OLWR are well simulated except for a few features, namely in January the low OLWR center located off the western shore of Mexico is located too far north. The main reason for this error is from the Sherr et al. cloud classification. The cloudiness given by Sherr et al. for this region is .28, which is substantially lower than expected. In general, this region has stratus cloud resulting from the cold north Pacific current. T_s-T_c ranges from 44^oK to 69^oK. These values are larger than in adjacent areas, which are around 15^oK. A similar problem occurs at the west coast of South America, where the off shore low OLWR center belongs to cloud region 3, see Figure 5.1. The cloud cover of this region is .80 which is much higher than others in its neighborhood of .45 to .60. Examining the RH field, figure 4.9, one would find that it is a low RH region, which is not in phase with the cloud cover. Apparently, there is an error due to cloudiness. One possibility is that the diurnal cycle of cloud cover in this region with maximum stratus in the morning is not well

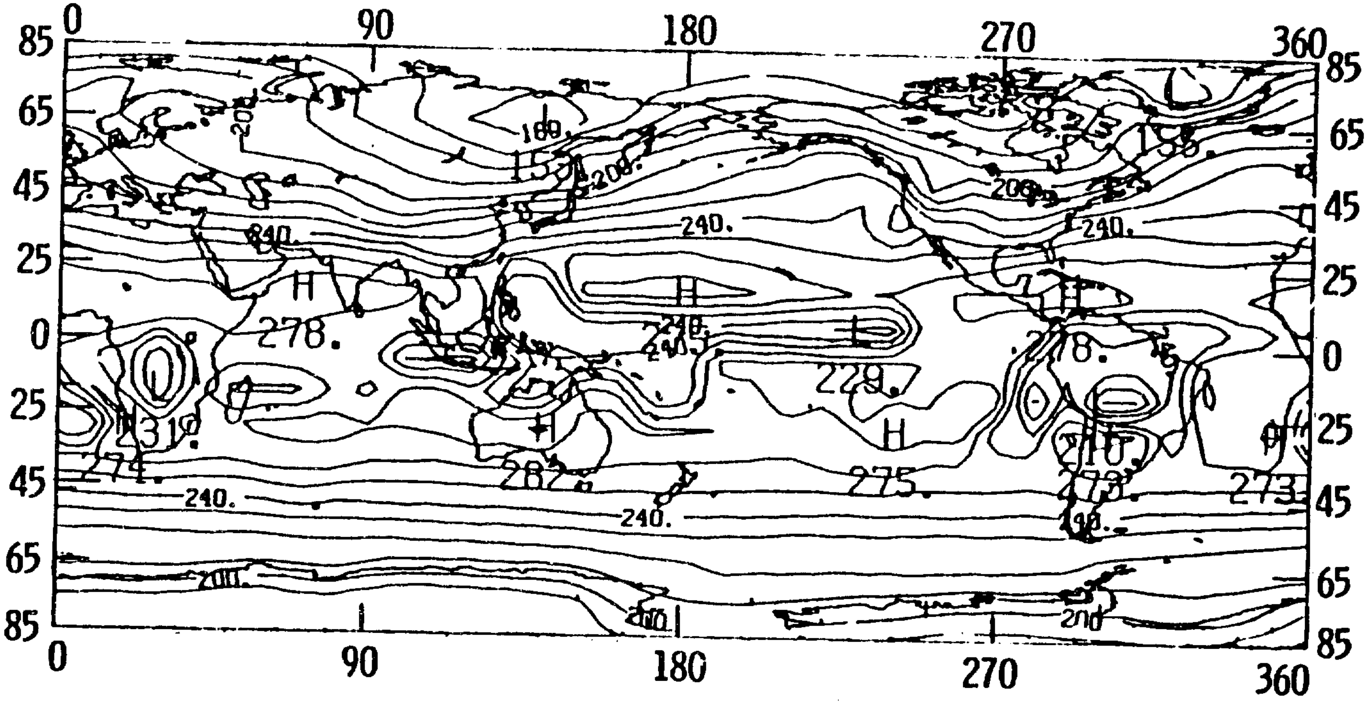

Figure 6.11 CD map for January, in W/m^2.

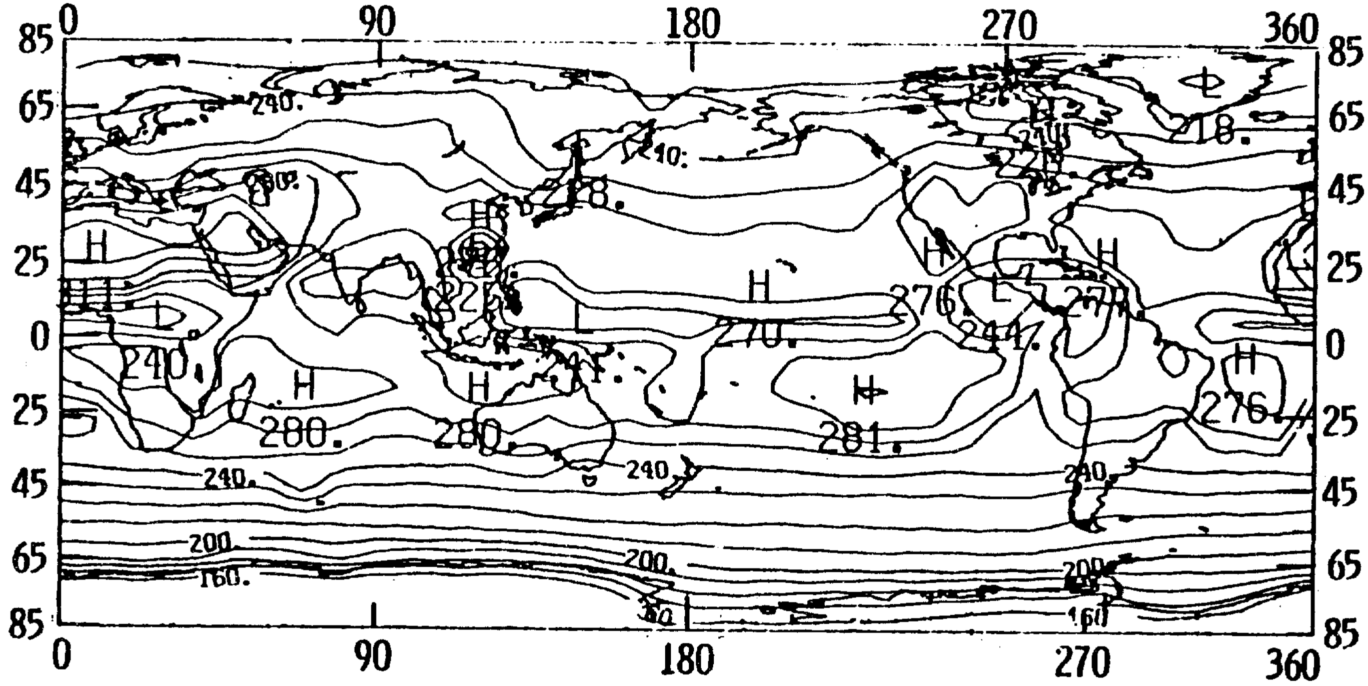

Figure 6.12 CD map for July, in W/m^2.

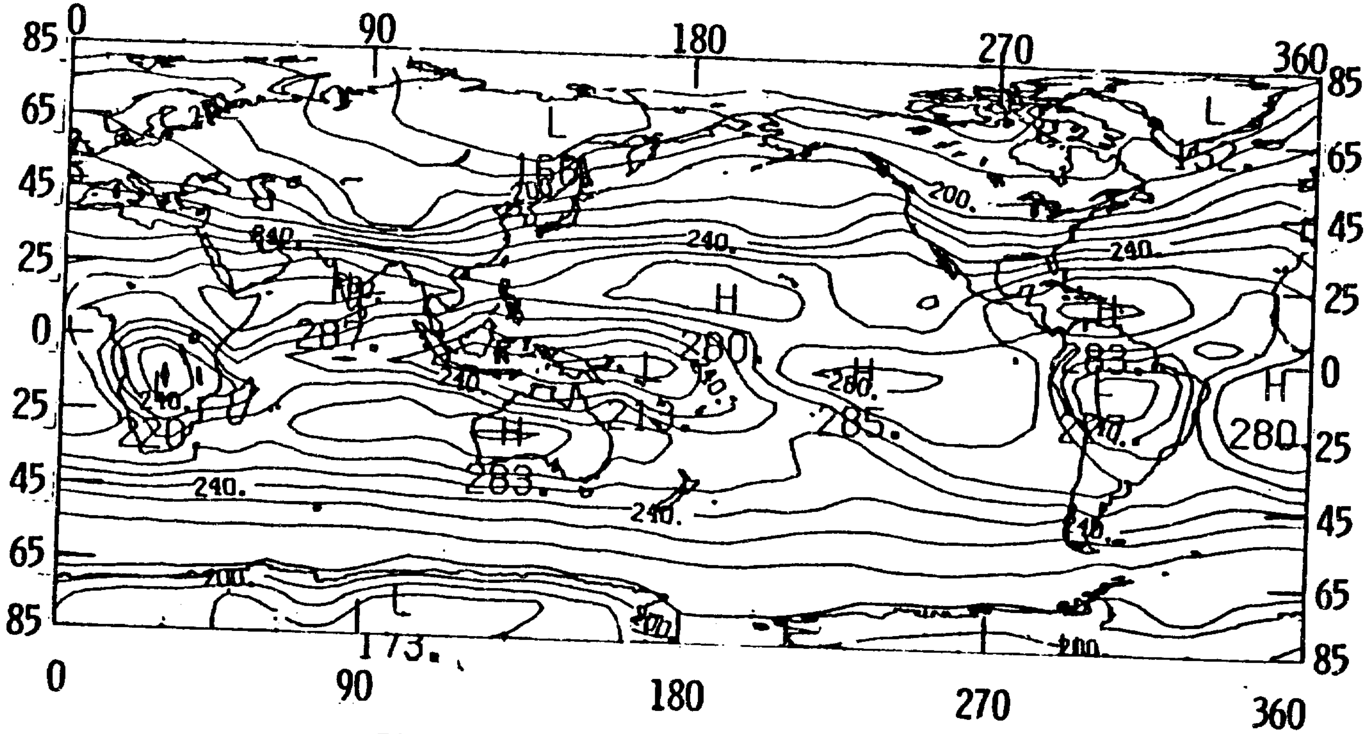

Figure 6.13 NOA map for January, in W/m^2.

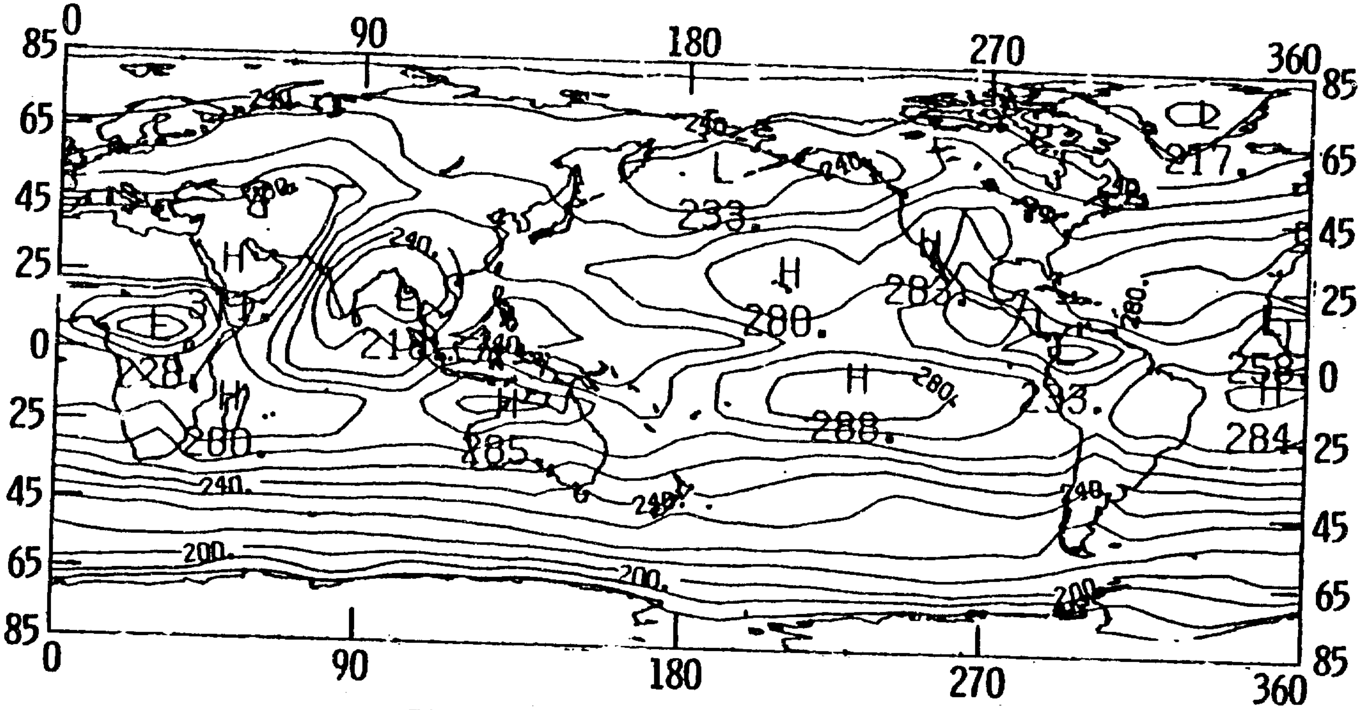

Figure 6.14 NOA map for July, in W/m^2.

simulated in the Sherr et al. model. We will have some words on the diurnal cycle at the end of this Chapter. Another problem occurs at the central Pacific low OLWR center, which extends too far east for both months. Other than these regions, most of the features are well simulated both in magnitude and in location. Since it is beyond the scope of this study to rework the cloud region classification, we will keep it as is, and discuss the the radiative transfer process of the majority of the regions which are well simulated.

Mid and High Latitude of the Northern Hemisphere

In January the major low OLWF centers at the high latitudes of the Northern Hemisphere are at Greenland and Siberia, with low OLWR at about 150 W/m^2, which are due to large surface snow-ice cover at this season. With these centers a wave pattern is formed along these latitudes. A strong ridge is located at Davis Strait and Baffin Bay region east of northern Canada. This is from the effect of warmer sea surface temperature relative to the adjacent continent, see Figure 4.12. The temperature diffference between the ocean and the continent is about 10°K. The similar feature with much larger scale occurs along the coast of both North America and Eurasia continents. Europe has a very mild meridional gradient due to the North Atlantic current extending beyond Scandinavia to the Barents Sea. Although located at 75°N, OLWR at this region is as strong as that of 55°N part of Siberia. In the Northern Pacific, the Kuroshio current also enhances the ridge at Alaska and Eastern Siberia. Comparison of CD with CR, Figure 4.13, shows that cloud's influence on these high latitudes is less than 10 W/m^2 and very homogeneous. Essentially, the contour pattern does not change when clouds are introduced; they only reduce the magnitude by approximately 10 W/m^2. Since the temperature is fairly low at this region, OLWR is insensitive to the moisture. Also, T_S-T_C is not large, being less than 5°K in most regions, and the OLWR is mainly from the surface. In July, this wave pattern due to continentality and ocean current is completely reversed except for the small section from Greenland to Scandinavia. Greenland is still a trough due to its icy surface and the Scandinavia area is very zonal and the intensity is increased to about 230 W/m^2. Again, in July, higher than 40°N the influence of cloud is fairly homogeneous and is about 10 W/m^2, except at eastern Siberia and Manchuria regions where T_S-T_C is about 30°K, much larger than in adjacent areas where it is less than 10°K. This area belongs to cloud region 10 which has very high seasonal cloud amount change. Figure 4.14 shows in July, the cloud cover is about .70, while at January is about .30.

Subtropics of the Both Hemispheres

In January, the strong OLWR in the subtropical high pressure regions, which coincide the descending leg of the Hadley Cell, can be found along the latitude circle of 15°N. The strength of this high is more than 270 W/m^2. This feature is interrupted in the Phillipines region, by the tropical ITCZ in the central Pacific. The OLWR here is less than 240 W/m^2. In the Southern Hemisphere, there is a counterpart of this high located along 30°S, with fairly equivalent strength.

This feature is highly modified by the ocean current and topography. On the coasts of South America, the stratus is formed by the cold ocean current at both sides of South Africa. This contributes to the low OLWR. The high at the west side of South Africa is due to the Kalahari Desert. This high can not be seen in CR, but in CD, it merely decreases by 5 W/m^2 from CR, much smaller than the decreases from CR to CD in the adjoining areas, where there is more than 30 W/m^2 decrease from cold cloud top temperature and higher cloudiness. Over the desert, T_s-T_c is about 10^{o}K and A_c is about .47, while in the southern part of the Congo Basin, T_s-T_c and A_c are more than 30^{o}K and .60 respectively. As the months change to July, these two subtropical high belts move northward with the sun. The northern component now covers a much larger area from 20^o to about 40^{o}N, depending on the longitude. Over the oceans, it is located about 10^o further south than over the continent. At North Africa, the Sahara Desert at low latitudes also enhance its strength to 310 W/m^2, which is the highest of the world. The southern component is located about 15^{o}S. However, its continuity is interrupted by some of the expansion of the tropical low OLWR center, such as the Andes of South America, eastern Indonesia and the southern part of the Congo. The strength is about 270 W/m^2, comparable to its northern counterpart.

Tropics

At the tropics, the pattern is the least zonal. First, in January there are three major low OLWR regions: the Amazon, Indonesia and the Congo. Second, Madagascar is a weak low OLWR region. Westward from

Central Africa the Amazon has very low OLWR, about 230 W/m^2. At the southeast Pacific Ocean, it increases to more than 270 W/m^2 then at Indonesia, it decreases to about 240w/m^2. Westward at the Indian Ocean monsoonal circulation OLWR increases to more than 275 W/m^2 in the clear season. At the African Congo, OLWR decreases to 240 W/m^2, and at the Southern Atlantic Ocean, it increases to more than 260 W/m^2 again. Here, basically the strength is equivalent to the subtropical high OLWR region, which is also true on the southeast Pacific. In the Indian Ocean, south of the monsoonal circulation, the OLWR is only up to 260 W/m^2, slightly less than that of the other two large oceans. As we have discussed in the sections on the humidity field and cloud cover field, the longitudinal variation is strongest in the tropical zone. This argument can also be applied to the July case, where this region is located north to that described above, with some feature changes. It is very clear that in July this low belt moves northward following the sun. The India monsoonal region is relatively cloudless, and Madagascar becomes a high OLWR center. The three lows along the tropics move northward. It is not uncommon that T_S-T_C is higher than 55^{o}K in the tropics. For cloud region 3, the tropical convective cloud amount for both January and July are higher than 60% and has little seasonal variation. The influence of ocean current along the continent in the Southern Hemisphere is still detectable. Southeast China is under southeast flow from the Pacific high, which brings in ocean moisture. This moist air is lifted by the low plateau to create the rain season, and thus a low OLWR center. As in the zonally averaged case, the minimum of OLWR in ITCZ region stays north of the equator except January and February when the cloudiness of the three major lows shift to the South. Over the open ocean the cloudiness associated with the ITCZ generally remains north of the equator.

At the Amazon, OLWR decreases from about 267w/m^2 for CR to less than 210 W/m^2 for CD. At this region, there is very strong diurnal variation with extreme convectivity. T_s-T_c at this region can reach more than 75^{o}K, with T_c less than -35^{o}C. At the peak of this diurnal cycle, the T_s-T_c can be even larger, T_c colder and OLWR below 180 W/m^2. A similar argument can be applied to the Congo, although it is less extreme, 265 W/m^2 for CR to 231 W/m^2 for CD. Also the case for Indonesia is less extreme 273 W/m^2 for CR to 239 W/m^2. Another feature is that the Amazon has more seasonal variation than the other two low OLWR centers. It is believed that over Indonesia, the cloud formation due to ITCZ has less diurnal cycles, which is not very clear in Sherr's cloud model. The ascending leg of the east-west Walker circulation coinciding with this convective region causes each cloud cluster to last for a few days. This can explain the reason why there is less seasonal variation at this region. One very interesting feature is that in July, the southern hemispheric winter, there is less convectivity over the Amazon and the Congo, thus OLWR is higher than that of January by about 10 W/m^2; over the Congo the difference is even larger. Over the strong OLWR region at the tropics, seasonal variation is not as prominent as the low OLWR regions; both southeast Pacific and central Pacific highs stay fairly constant.

Mid and High Latitudes of the Southern Hemisphere

South of the southern component of subtropical high OLWR band, from 40° to 70°S, the feature is very zonal due the fact that only ocean is present here. The average gradient of OLWR with the latitude is about 1.5 and 1.7 W/m^2 per degree latitude for January and July respectively, which is more moderate than that of the Northern Hemisphere with 1.8 and 1.1 W/m^2 per degree latitude for January and July respectively. At Antarctic, the OLWR contour is deformed by the orography.

Longitudinal Deviation

To demonstrate the longitudinal variability, we reconstruct an annual longitudinal OLWR deviation contour by calculating:

$$\underline{F}_{dv}(j,k)=\underline{F}_{an}(j,k)-\underline{F}_{az}(k) \qquad 6.1$$

where $\underline{F}_{dv}$ is the annual zonal OLWR deviation for the grid point of latitude k, longitude j, $\underline{F}_{an}$ is the annual average OLWR, and $\underline{F}_{az}$ is the annual zonally averaged OLWR for the latitude k. This is shown on Figure 6.15. One would easily identify that the highest deviation are between 5°N and 20°S, with three dipoles of about $\pm$ 25 W/m^2. Other regions that have strong deviation are Tibet, Mideast, and Greenland.

6.4 Error Statistics

The percentage difference between NOA and CD is discretized by rounding off to the nearest integer for every grid box. Figures

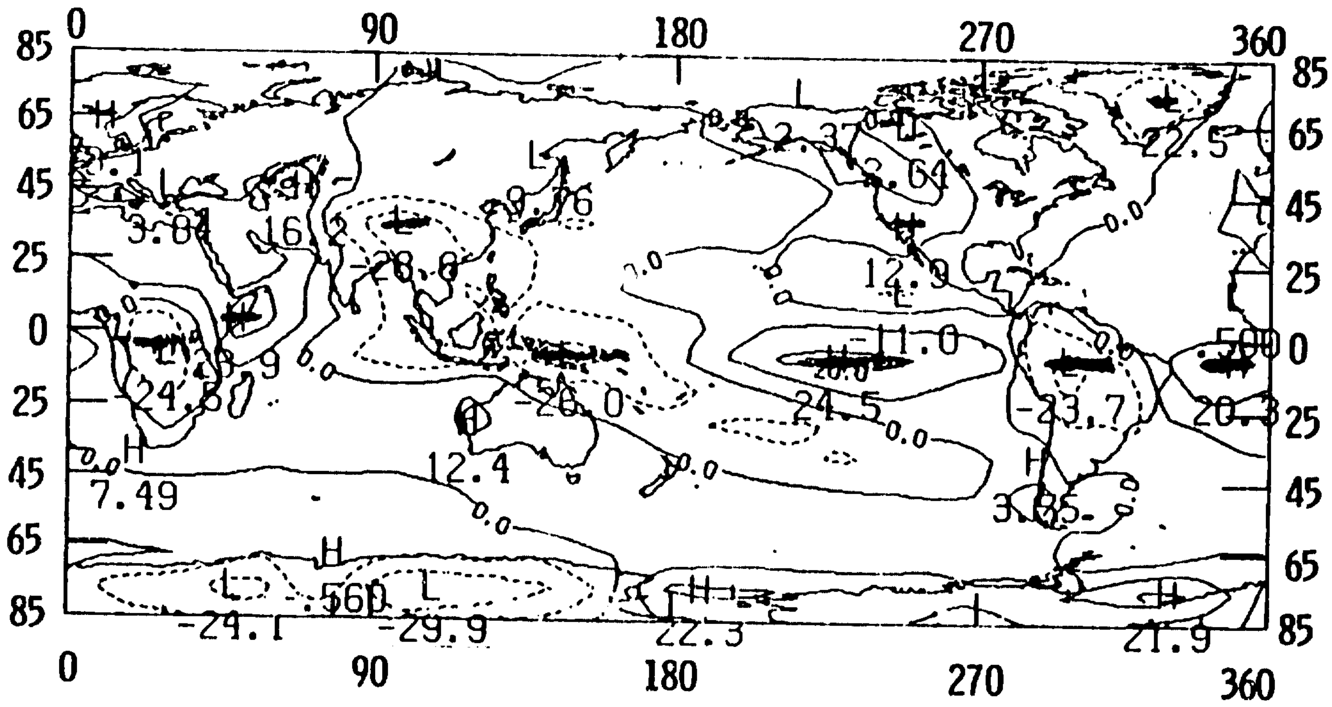

Figure 6.15 Longitudinal OLWF deviation for annual CD, in W/m^2.

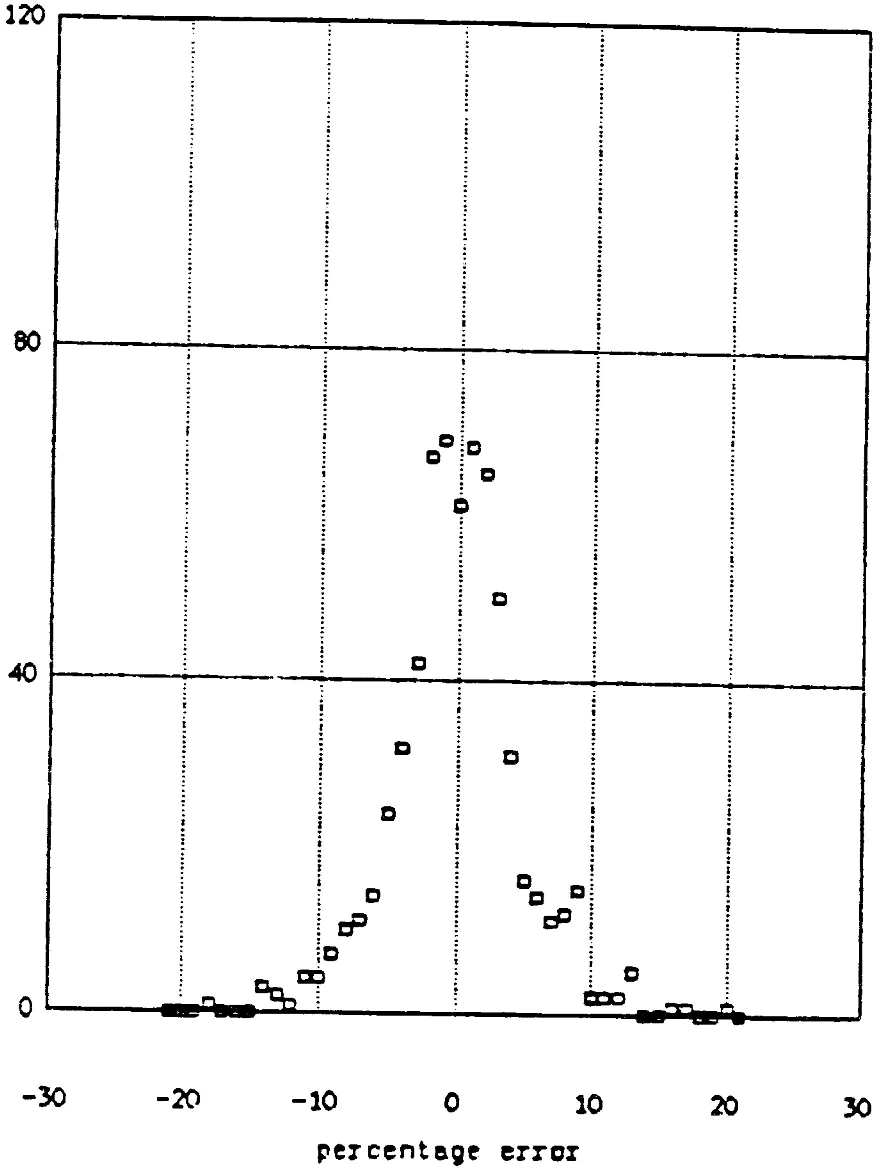

Figure 6.16 Histogram of error for January, σ=4.6%.

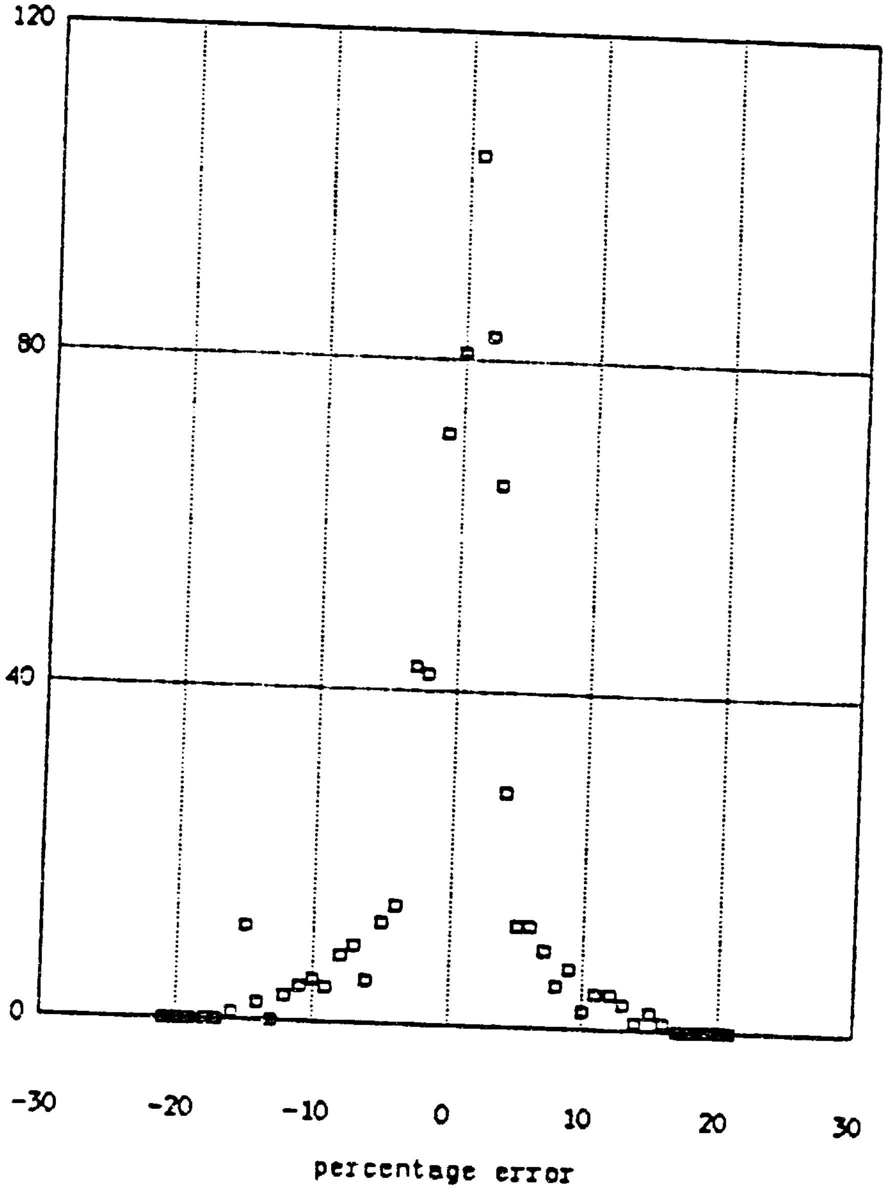

Figure 6.17 Histogram of error for July, σ=4.1%.

6.16 and 6.17 are scatter plot histograms of the discretized percentage difference versus numbers of grid boxes for January and July respectively. For both cases, the distributions are quite normal with standard deviations of 4.6 for January and 4.1% for July. Note that the total number of grid boxes is 648. These histograms manifest the reasonably good performance of this model. Table 6.4 tabulates the global standard deviation for each cloud type region for each month of the model year. Although there is some difference between the highest standard deviation, i.e. 4.6% for January and February, and the lowest, 3.4% for September, October and November, there is no apparent seasonal dependence.

To study in detail how the difference is distributed in longitude and latitude, Tables 6.5 and 6.6 tabulate January and July percentage difference on grid box coordinates accompanied by the Sherr et al. (1968) cloud region classification for easy identification. One can find with ease that for most cloud regions there are both positive and negative differences in each cloud block. Although these differences can be from the deviation of any radiative parameter, the largest error is possibly from the variability of cloudiness. As discussed in Chapter 2, our grid box has a size of 10^ox10^o. Practically, homogeneous cloud can not extend more than a few grid boxes of such a size. With mixed clouds in a cloud block, using a single cloud top level to specify cloud top temperature is bound to introduce error. What is striking is that for most regions, the error is within 5%. As one would guess, the highest error occurs at the tropics with its strong convectivity, where the errors are higher

cloud type	1	2	3	4	5	6	7	8	9	10	11	12	13	14	15	16	17	18	19	20	21	22	23	24	25	26	27	28	29	global std. dev
no. grids	7	36	38	79	3	1	1	1	30	19	18	10	18	19	74	12	6	10	4	21	7	35	52	92	12	6	2	3	32	
JAN	2	4	10	5	2	2	1	3	3	4	3	4	4	4	6	3	2	2	2	3	4	3	2	2	6	3	1	1	3	4.6
FEB	1	3	9	5	2	2	1	2	3	4	2	3	4	4	5	5	2	1	2	3	5	3	2	5	7	3	1	1	3	4.6
MAR	2	3	9	4	1	2	0	1	2	4	2	3	3	3	4	7	3	1	2	3	5	3	2	4	7	3	0	1	3	4.3
APR	2	3	9	4	1	0	0	2	3	6	2	4	3	2	4	8	2	3	3	3	5	3	2	4	7	2	1	2	3	4.2
MAY	2	4	5	4	2	0	0	2	3	4	2	5	4	2	2	5	2	2	3	2	3	2	1	4	4	1	0	3	3	3.5
JUN	2	4	6	4	2	0	1	1	2	5	3	6	4	2	1	5	5	2	5	4	2	2	1	4	4	1	1	3	3	3.8
JLY	1	5	6	4	2	0	0	2	3	6	2	6	3	2	2	8	8	2	8	3	2	2	1	4	4	1	0	3	3	4.1
AUG	1	5	6	4	1	1	1	1	2	4	3	7	2	3	1	1	6	2	8	4	2	2	2	3	4	1	1	3	3	3.9
SPT	2	5	5	4	1	2	0	1	2	3	4	5	3	3	3	4	5	2	4	2	2	2	2	3	6	2	1	1	3	3.4
OCT	2	3	5	4	1	2	1	2	4	2	3	5	3	6	2	5	2	2	2	2	5	2	2	3	7	3	1	0	3	3.4
NOV	2	3	5	4	1	3	2	1	2	2	2	4	4	4	3	4	2	1	2	2	6	2	2	3	7	4	1	2	4	3.4
DEC	2	4	6	5	2	3	1	2	2	3	2	3	4	3	4	3	2	2	2	3	6	3	1	2	5	2	1	2	3	3.6
ANU	1.7	3.8	6.8	4.3	1.5	1.5	0.7	1.7	2.6	4.0	2.5	4.6	3.4	3.2	3.0	4.8	3.4	1.8	3.6	2.8	4.0	2.4	1.7	3.4	5.4	2.2	0.8	1.8	3.1	4.2

Table 6.4 RMS error in percentage for each cloud type and global standard deviation for each month in percentage. Number of grid box for each cloud type is also shown.

PERCENTAGE ERROR MAP

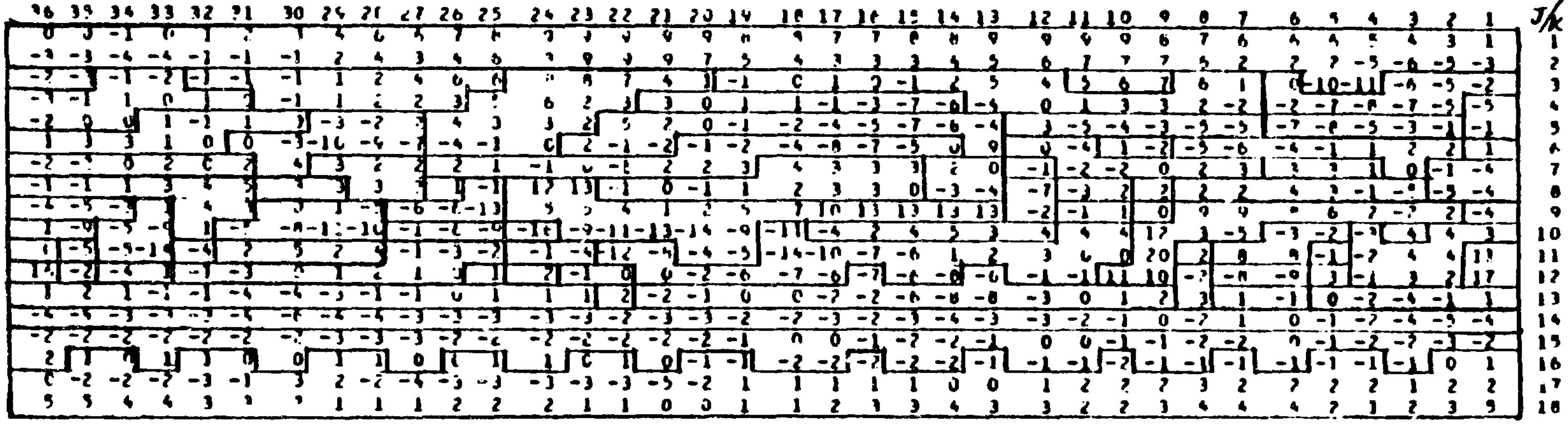

36	35	34	33	32	31	30	29	28	27	26	25	24	23	22	21	20	19	18	17	16	15	14	13	12	11	10	9	8	7	6	5	4	3	2	1	J/K
0	3	-1	0	1	2	1	4	6	5	7	8	9	9	9	9	9	8	9	7	7	8	8	9	9	9	9	6	7	6	4	4	5	4	3	1	1
-3	-3	-4	-4	-3	-1	-1	2	4	3	4	6	9	9	9	9	7	5	4	3	3	3	4	5	6	7	7	7	5	2	2	2	-5	-6	-5	-3	2
-2	-3	-1	-2	-3	-1	-1	1	2	4	6	6	8	8	7	4	3	-1	0	1	2	-1	2	5	4	5	6	7	6	1	0	-10	-11	-6	-5	-2	3
-1	-1	1	0	1	2	-1	1	2	2	3	2	6	2	3	3	0	1	1	-1	-3	-7	-6	-5	0	1	3	3	2	-2	-2	-7	-8	-7	-5	-5	4
-2	0	0	1	-1	1	1	-3	-2	3	4	3	3	2	5	2	0	-1	-2	-4	-5	-7	-6	-4	3	-5	-4	-3	-5	-5	-7	-8	-5	-3	-1	-1	5
1	3	3	1	0	0	-3	-10	-5	-7	-4	-1	0	2	-1	-2	-1	-2	-4	-8	-7	-5	0	9	0	-4	1	-2	-5	-6	-4	-1	1	2	2	1	6
-2	-5	0	2	0	2	4	3	2	2	2	1	-1	0	-1	2	2	3	4	3	3	3	2	0	-1	-2	-2	0	2	3	3	3	1	0	-1	-4	7
-1	-1	1	3	4	5	4	3	3	3	1	-1	12	13	-1	0	-1	1	2	3	3	0	-3	-4	-7	-3	2	2	2	2	4	3	-1	-8	-5	-4	8
-4	-5	-3	3	4	1	3	1	-1	-6	-6	-13	5	5	4	1	2	5	7	10	13	13	13	13	-2	-1	1	0	9	9	8	6	7	-7	2	-4	9
1	-8	-5	-9	1	-7	-8	-1	-10	-1	-6	-9	-16	-9	-11	-13	-14	-9	-11	-4	2	4	5	3	4	4	4	17	3	-5	-3	-2	-3	4	4	3	10
1	-5	-5	-14	-4	2	5	2	4	-1	-3	-2	-1	-4	-12	-5	-4	-5	-14	-10	-7	-6	1	2	3	6	0	20	2	8	9	-1	-2	4	4	11	11
14	-2	-4	1	-1	-3	[illegible]	1	2	1	3	1	2	-1	0	0	-2	-6	-7	-6	-7	-6	-8	-6	-1	-1	11	10	-7	-8	-9	3	-1	3	2	17	12
1	2	1	-1	-1	-4	-4	-3	-1	-1	0	1	1	1	2	-2	-1	0	0	-2	-2	-6	-8	-8	-3	0	1	2	3	1	-1	0	-2	-4	-1	1	13
-4	-5	-3	-1	-3	-5	-6	-4	-4	-3	-3	-3	-1	-3	-2	-3	-3	-2	-7	-3	-2	-3	-4	-3	-3	-2	-1	0	-7	1	0	-1	-7	-4	-5	-4	14
-2	-2	-2	-2	-2	-2	-2	-3	-3	-3	-2	-2	-2	-2	-2	-2	-2	-1	0	0	-1	-2	-2	-1	0	0	-1	-1	-2	-2	0	-1	-2	-2	-3	-2	15
2	1	0	1	1	0	0	1	1	0	1	1	1	0	1	0	-1	-1	-2	-2	-2	-2	-2	-1	-1	-1	-2	-1	-1	-1	-1	-1	-1	-1	0	1	16
0	-2	-2	-2	-3	-1	3	2	-2	-4	-3	-3	-3	-3	-3	-5	-2	1	1	1	1	1	0	0	1	2	2	2	3	2	2	2	2	1	2	2	17
5	5	4	4	3	3	3	1	1	1	2	2	2	1	1	0	0	1	1	2	3	3	4	3	3	2	2	3	4	4	4	2	1	2	3	5	18

CLOUD CLIMATOLOGY MAP....SHERR

36	35	34	33	32	31	30	29	28	27	26	25	24	23	22	21	20	19	18	17	16	15	14	13	12	11	10	9	8	7	6	5	4	3	2	1	J/K
15	15	15	15	15	15	15	15	15	15	15	15	15	15	15	15	15	15	15	15	15	15	15	15	15	15	15	15	15	15	15	15	15	15	15	15	1
15	15	15	15	15	15	15	15	15	15	15	15	15	15	15	15	15	15	15	15	15	15	15	15	15	15	15	15	15	15	15	15	15	15	15	15	2
14	14	11	11	9	9	9	9	9	9	9	9	10	10	10	10	10	9	9	9	9	9	9	9	9	10	10	10	9	9	14	15	15	14	14	14	3
11	11	11	11	11	11	9	9	9	9	9	10	10	10	10	14	14	14	14	14	14	14	14	9	9	9	9	9	9	9	14	14	14	14	14	11	4
11	11	11	18	18	18	18	2	2	2	10	10	10	10	13	13	13	13	13	13	13	13	13	13	8	11	11	11	11	11	13	13	13	13	13	11	5
18	19	18	18	18	2	2	2	2	2	10	10	10	13	13	13	20	20	20	20	20	20	20	25	2	2	19	19	20	20	20	20	20	20	20	18	6
1	1	1	1	1	1	2	16	16	16	19	19	20	20	20	20	20	20	4	4	4	4	12	12	7	2	4	4	4	4	4	4	4	20	2	2	7
2	2	2	2	2	2	17	17	16	16	12	4	3	3	4	4	4	4	4	4	4	4	12	12	4	17	17	16	17	17	17	17	17	12	2	2	8
16	16	16	4	2	2	4	4	4	12	4	4	3	3	3	3	3	3	3	3	3	3	3	3	4	16	16	4	3	3	3	3	3	3	3	16	9
21	21	25	4	2	4	4	4	4	25	25	25	4	3	3	3	3	3	4	2	2	2	2	2	2	4	4	3	3	3	25	25	4	2	4	4	10
5	26	25	4	26	21	21	21	21	4	4	26	25	25	4	4	3	3	4	4	4	4	4	4	4	4	4	3	6	25	25	21	4	4	4	3	11
3	2	26	26	4	4	4	4	4	4	4	2	1	2	26	4	4	4	4	4	29	4	4	29	4	4	3	3	5	4	4	3	4	4	4	3	12
29	29	29	29	29	29	27	29	24	24	29	29	27	27	28	29	29	29	29	29	29	29	29	24	29	24	29	29	5	28	28	29	29	29	29	29	13
22	22	22	22	22	22	22	22	22	22	22	22	22	22	22	22	22	22	22	22	22	22	22	22	22	22	22	22	22	2	22	22	22	22	22	22	14
23	23	23	23	23	23	23	23	23	23	23	23	23	23	23	23	23	23	23	23	23	23	23	23	23	23	23	23	23	23	23	23	23	23	23	23	15
23	24	24	23	24	24	23	24	24	23	24	24	23	24	24	23	24	24	23	23	24	23	23	24	23	23	24	23	23	24	23	24	24	23	24	24	16
24	24	24	24	24	24	24	24	24	24	24	24	24	24	24	24	24	24	24	24	24	24	24	24	24	24	24	24	24	24	24	24	24	24	24	24	17
24	24	24	24	24	24	24	24	24	24	24	24	24	24	24	24	24	24	24	24	24	24	24	24	24	24	24	24	24	24	24	24	24	24	24	24	18

Table 6.5 January percentage OLWR difference, (NOA-CD)/NOA, tabulated on grid coordinate. $J \times 10^{\circ}$ is west longitude, $85^{\circ}-(k-1) \times 10^{\circ}$ is latitude. Regions are separated according to Sherr *et al*. (1968) cloud region classification tabulated below.

PERCENTAGE ERROR MAP

36	35	34	33	32	31	30	29	28	27	26	25	24	23	22	21	20	19	18	17	16	15	14	13	12	11	10	9	8	7	6	5	4	3	2	1	J/K
1	1	1	1	1	1	1	1	1	1	1	1	1	2	2	2	2	2	2	2	2	2	2	1	1	1	0	0	0	1	1	1	1	2	1	1	1
1	0	0	1	2	2	2	2	1	1	1	1	1	1	1	2	3	3	3	3	3	2	2	3	3	2	2	1	1	0	-1	-1	-1	2	2	2	2
1	1	1	1	4	5	3	3	3	-1	-2	-1	4	4	3	6	7	4	2	3	2	1	6	6	3	6	8	6	0	-1	-1	-1	-1	-1	1	2	3
0	3	2	2	3	3	3	3	3	-2	-4	3	2	7	7	-1	-1	-1	-2	-2	0	-1	-1	-5	-2	1	0	-2	-2	-3	-3	-3	-3	-3	-3	-2	4
1	3	3	0	-2	0	1	4	6	6	1	-2	3	2	-3	-2	-3	-4	-3	-3	-2	-2	-1	1	-2	2	-1	-3	-4	-3	-1	-1	-1	0	0	1	5
-1	1	1	1	2	5	8	-4	-7	-12	-11	-11	-8	-5	-2	-3	-3	-2	2	3	4	4	1	0	1	-2	0	-3	-5	-4	-1	1	4	2	2	0	6
-2	3	2	2	1	1	0	-7	-10	-14	-14	4	-3	-4	-3	-2	6	0	4	5	6	5	3	3	0	-6	1	2	1	0	3	4	4	1	0	-1	7
-10	-9	-2	-4	1	4	5	-11	-9	-12	-15	-8	-4	-3	-6	-3	-1	-1	0	1	2	2	2	-1	-5	6	0	4	9	11	3	4	2	-1	-9	-11	8
3	-3	-5	-5	3	1	-6	-10	-8	-10	-8	-10	-2	-3	-1	0	1	-1	-1	1	4	6	7	6	-3	6	2	-7	-7	-4	-5	-1	4	4	4	7	9
1	-1	-1	2	1	-6	-7	-7	-6	-10	-4	-3	-9	-8	-3	-12	-8	3	1	2	4	6	6	5	3	3	2	8	3	4	1	2	3	2	5	4	10
3	3	1	3	1	-1	-1	-1	-2	-1	2	1	3	2	1	-2	0	2	2	3	3	3	1	1	2	3	2	7	0	-1	4	3	5	2	1	6	11
11	3	-1	1	6	3	1	3	5	4	1	3	-1	1	-1	4	2	0	-2	-3	-3	-5	-7	-5	-3	2	5	6	1	-3	2	7	3	2	0	11	12
0	1	1	3	2	0	0	1	2	2	2	2	-1	0	1	3	3	2	1	-1	-2	-4	-6	-7	-5	-2	-1	-1	0	-4	-1	-1	-1	-1	0	-1	13
-3	-3	-4	-2	-2	-1	-5	0	0	0	0	0	0	1	2	2	3	1	1	1	2	1	0	-1	-2	-2	-1	-1	-3	-3	0	-2	-3	-3	-3	-3	14
-1	5	0	1	-1	-1	-1	-1	-1	-2	0	0	0	0	0	1	2	2	1	1	1	1	1	1	1	1	0	1	0	0	-1	-1	-2	-3	-2	-2	15
2	1	0	0	0	0	0	0	2	1	1	2	2	0	0	-1	-2	-1	-1	-2	-2	-2	-1	0	1	1	0	-1	-1	-2	-5	-3	-2	0	2	4	16
7	4	3	3	9	9	12	10	5	5	3	2	1	0	-3	-7	-1	1	2	1	1	1	0	-1	-1	0	-1	0	2	1	-2	1	3	6	9	10	17
13	14	15	16	15	13	13	12	12	11	9	7	5	4	2	1	-1	-3	-2	-2	-1	0	1	0	0	0	2	3	2	2	1	2	4	6	9	12	18

CLOUD CLIMATOLOGY MAP....SHEPR

36	35	34	33	32	31	30	29	28	27	26	25	24	23	22	21	20	19	18	17	16	15	14	13	12	11	10	9	8	7	6	5	4	3	2	1	J/K
15	15	15	15	15	15	15	15	15	15	15	15	15	15	15	15	15	15	15	15	15	15	15	15	15	15	15	15	15	15	15	15	15	15	15	15	1
15	15	15	15	15	15	15	15	15	15	15	15	15	15	15	15	15	15	15	15	15	15	15	15	15	15	15	15	15	15	15	15	15	15	15	15	2
14	14	11	11	9	9	9	9	9	9	9	9	10	10	10	10	10	9	9	9	9	9	9	9	9	10	10	10	9	9	14	15	15	14	14	14	3
11	11	11	11	11	11	9	9	9	9	9	10	10	10	10	14	14	14	14	14	14	14	14	9	9	9	9	9	9	9	14	14	14	14	14	11	4
11	11	11	18	18	18	18	2	2	2	10	10	10	10	13	13	13	13	13	13	13	13	13	13	8	11	11	11	11	11	13	13	13	13	13	11	5
18	18	18	18	18	2	2	2	2	2	10	10	10	13	13	13	20	20	20	20	20	20	20	25	2	2	19	19	20	20	20	20	20	20	20	18	6
1	1	1	1	1	1	2	16	16	16	19	19	20	20	20	20	20	20	4	4	4	4	12	12	7	2	4	4	4	4	4	4	4	20	2	2	7
2	2	2	2	2	2	17	17	16	16	12	4	3	3	4	4	4	4	4	4	4	4	12	12	4	17	17	16	17	17	12	12	12	12	2	2	8
16	15	16	4	2	2	4	4	4	12	4	4	3	3	3	3	3	3	3	3	3	3	3	3	4	16	16	4	3	3	3	3	3	3	3	16	9
21	21	25	4	2	4	4	4	4	25	25	25	4	3	3	3	3	3	4	2	2	2	2	2	2	4	4	3	3	3	25	25	4	7	4	4	10
5	26	25	4	26	21	21	21	21	4	4	26	25	25	4	4	3	3	4	4	4	4	4	4	4	4	4	3	6	25	25	21	4	4	4	3	11
3	2	26	26	4	4	4	4	4	4	4	2	1	2	26	4	4	4	4	4	29	4	4	29	4	4	3	3	5	4	4	3	4	4	4	3	12
29	29	29	29	29	29	29	29	29	29	29	29	27	27	29	29	29	29	29	29	29	29	29	29	29	29	29	29	5	28	28	29	29	29	29	29	13
22	22	22	22	22	22	22	22	22	22	22	22	22	22	22	22	22	22	22	22	22	27	22	22	22	22	22	22	22	2	27	22	27	22	22	22	14
23	23	23	23	23	23	23	23	23	23	23	23	23	23	23	23	23	23	23	23	23	23	23	23	23	23	23	23	23	23	23	23	23	23	23	23	15
23	24	24	23	24	24	23	24	24	23	24	24	23	24	24	23	24	24	23	23	24	23	23	24	23	23	24	23	23	24	23	24	24	23	24	24	16
24	24	24	24	24	24	24	24	24	24	24	24	24	24	24	24	24	24	24	24	24	24	24	24	24	24	24	24	24	24	24	24	24	24	24	24	17
24	24	24	24	24	24	24	24	24	24	24	24	24	24	24	24	24	24	24	24	24	24	24	24	24	24	24	24	24	24	24	24	24	24	24	24	18

Table 6.6 Same as table 6.5 but for July.

than 10%. The strong convectivity in the region generally generates non-stratus type cloud, which usually is less homogeneous. One example is the cloud region 3 located in the central Pacific and the northern part of South America. For the former region, the difference ranges from +13% to -14%; for the latter region, the difference ranges from +20% to -5%. No other regions have such a diverse difference within a cloud block. It is recommended that this region be further studied and possibly subdivided and reclassified. One other interesting feature is that at the polar regions, cloud region 15 for the northern one and 24 for the southern one, each one has higher error at polar night. This coincides with the error of cloud fraction shown in Figures 5.2 and 5.3. Obviously, the cloud observation in the polar night time needs to be improved.

To demonstrate the error according to each cloud type, monthly latitudinal weighted RMS errors for each cloud region are calculated and tabulated on table 6.4. This table 6.4 provides a good source for tracing the model performance based on each cloud type, and as well indicates the area for future improvement. It is intriguing to see that more than half of the cloud types have consistant and small, below 5%, errors, while some do not, such as cloud regions 3, 12, 16, 17, 19 and 25. Except for two of the four grid boxs of cloud type 19 that are located at 35^{O}N, all the rest are located in the tropics and subtropics region between 25^{O}N and 25^{O}S. This again stresses the difficulty of modeling the cloud in the tropics region. Another note is that when compared table 6.4 with the cloud top level, table 5.7, there exists no correlation. It is recalled from Chapter 5 that cloud regions 3 and 12 have very steady cloud top level throughout the year, while cloud regions 17, 19 and 25 have strong cloud top level variation.

Diurnal Cycle

Another area which should be discussed is the bias of satellite measurement due to OLWR diurnal cycle. Polar orbiting satellites are often used to measure the earth radiation budget. Since the satellite passing time is fixed at a certain local time, the diurnal cycle must be understood in order to estimate the total budget. Unfortunately, the OLWR diurnal cycle changes from region to region. Over deserts where there is little cloud, the OLWR essentially follows the surface temperature and peaks at mid-afternoon. Over rain forests where strong convectivities occur in the afternoon, the cold cloud top temperature of cumulus minimizes OLWR. Over the west coast of America, where stratus cloud forms in the early morning and dissipates later, OLWR has its minimum in the morning. Other types of topography have different characteristics. Figure 6.18 from Saunders and Hunt (1980) reveals some of the different types of OLWR diurnal cycles. Minnis and Harrison (1984), Kandel (1983) and Brook and Minnis (1984) have pioneered some of the work in this areas. Still many areas have not been investigated. It is important to explore this phenomenon further in order to justify the estimation of total radiation budget from polar orbiting satellites.

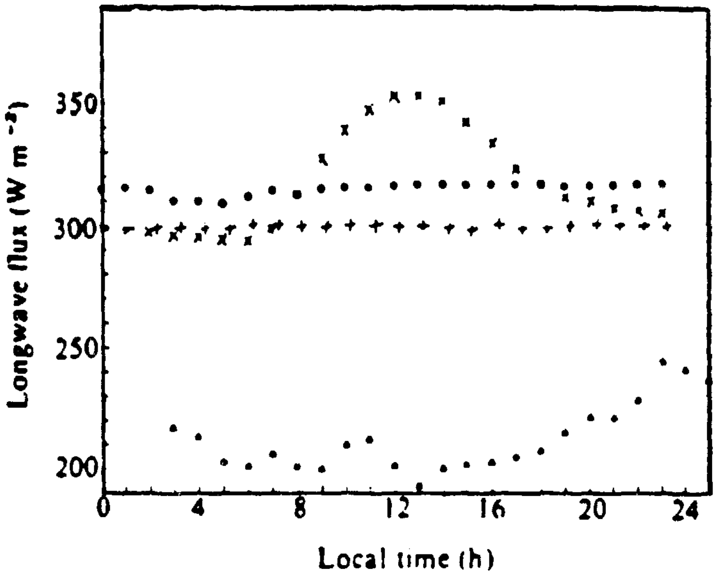

Figure 6.18 The diurnal variation of OLWR for different types of surface after Saunder and Hunt (1980). x, over land; ●, over sea; +, over low Cu cloud; ▲, over high Cu-Nb cloud.

CHAPTER 7

CONCLUSIONS AND RECOMMENDATIONS

A simple and economical earth outgoing longwave radiation climate model has been composed for radiation budget study. The model consists of the the upward radiative transfer parameterization of Thompson and Warren (1982), the cloud cover model of Sherr et al. (1968) and a monthly average climatology defined by the data from Crutcher and Meserve (1971) and Taljaard et al. (1969). Additional required information is provided by the empirical 100mb water vapor mixing ratio equation of Harries (1976) and mixing ratio interpolation scheme of Briegleb and Ramanathan (1982). Reference data from the NOAA scanning radiometer are used to compile a climatology for the cloud top temperature. Both clear sky and cloudy sky cases are calculated and discussed for global average, zonal average and global distributed cases.

The clear sky case shows that the OLWR field is highly modulated by water vapor, especially in the tropics. The strongest longitudinal variation occurs in the tropics. This variation can be mostly explained by the strong water vapor gradient. Although in the zonal average case the tropics has a minimum in OLWR, the minimum is essentially contributed by a few very low flux regions, such as the Amazon, Indonesia and the Congo. There are regions in the tropics such that their OLWR is as intense as that of the subtropics. In the high latitudes, where cold air contains less water vapor, OLWR is basically modulated by the surface temperature. Thus, the topographical heat capacity becomes a dominant factor in determing the distribution.

Clouds enhance water vapor modulation of OLWR. Tropical clouds have the coldest cloud top temperature. This again increases the longitudinal variation in the region. However, in the polar region, where a temperature inversion is prominent, the cloud top temperature is warmer than the surface. Hence, cloud has the effect of increasing OLWR. The implication of this cloud mechanism is that the latitudinal gradient of net radiation is thus further increased, and the forcing of the general atmospheric circulation is substantially different due to the increased additional available energy.

In the clear sky case, regional results of North and South America are compared with GOES data analyzed by Minnis and Harrison (1984) with reasonable agreement. The cloudy sky cases also agree well with the NOAA satellite observation. These cases minutely overestimate the global average and have less error in the mid-high latitudes, and higher errors in the tropics and the winter polar region in both of the zonally averaged and global distributed cases, with standard deviation equal to 4.6% and 4.1% for January and July respectively.

In simulating the case with clouds, the global cloud adjusting factor GLCLC defined by Bartman (1980) can be used for minor tuning. However, the OLWR field can be more effectively adjusted by changing cloud top temperature. The current compiled cloud top temperature climatology is probably overestimated due to the inversion scheme used for the NOAA scanning radiometer data. Using other satellite data as the reference would change the result.

The climatological cloud region classification by Sherr et al. (1968) is relevent for simulating the cloud distrbution in most areas except the tropical regions where the cloud region classification should be further investigated when new cloud data become available. Since many semi-annual air mass systems not only change the intensity, but also the area of coverage, seasonality of cloud region possibly needs to be included. Why the cloud cover climatology of London (1957) and von Loon (1972) significantly differ from that of the Sherr et al. (1968) in the polar night region should be addressed as well.

This study also presents a global RH climatology. Since the cloud cover is highly correlated with the water vapor distribution, and the water vapor can be more objectively measured, regardless of the fact that there still lack good measurement between 400 and 100mb, some effort should be spent on establishing the empirical relationship between the two. Thus, the more simple Budyko-Seller type longwave parameterization can be upgraded to the form $F=a+bT+c\underline{RH}$ so as to improve OLWR computation in the tropical region.

This model can be implemented to study the time-space variation of the OLWR field, as well as the sensitivity of the OLWR field to the different input parameters. One example of such a case is to overlay the current data base with the statistics of the atmospheric variability (Oort, 1983, the data tape would be available soon) as the input data. Variability of the OLWR can thus be analyzed. Another application is to study the sensitivity of the earth net radiation budget to cloudiness. Since both the Time-Variable Albedo Model of Bartman (1980) and this longwave model use the cloud model of Sherr, et al. (1968), this can be achieved first by using the albedo model to compute a solar absorbed radiation. The variation of the cloud cover to achieve global annual energy balance can then be applied to the composite of the two models. Because the absorptivity of cloud decreases as the solar zenith angle increases, one would again expect that the latitudinal net energy gradient increases due to the effect of cloud.

APPENDICES

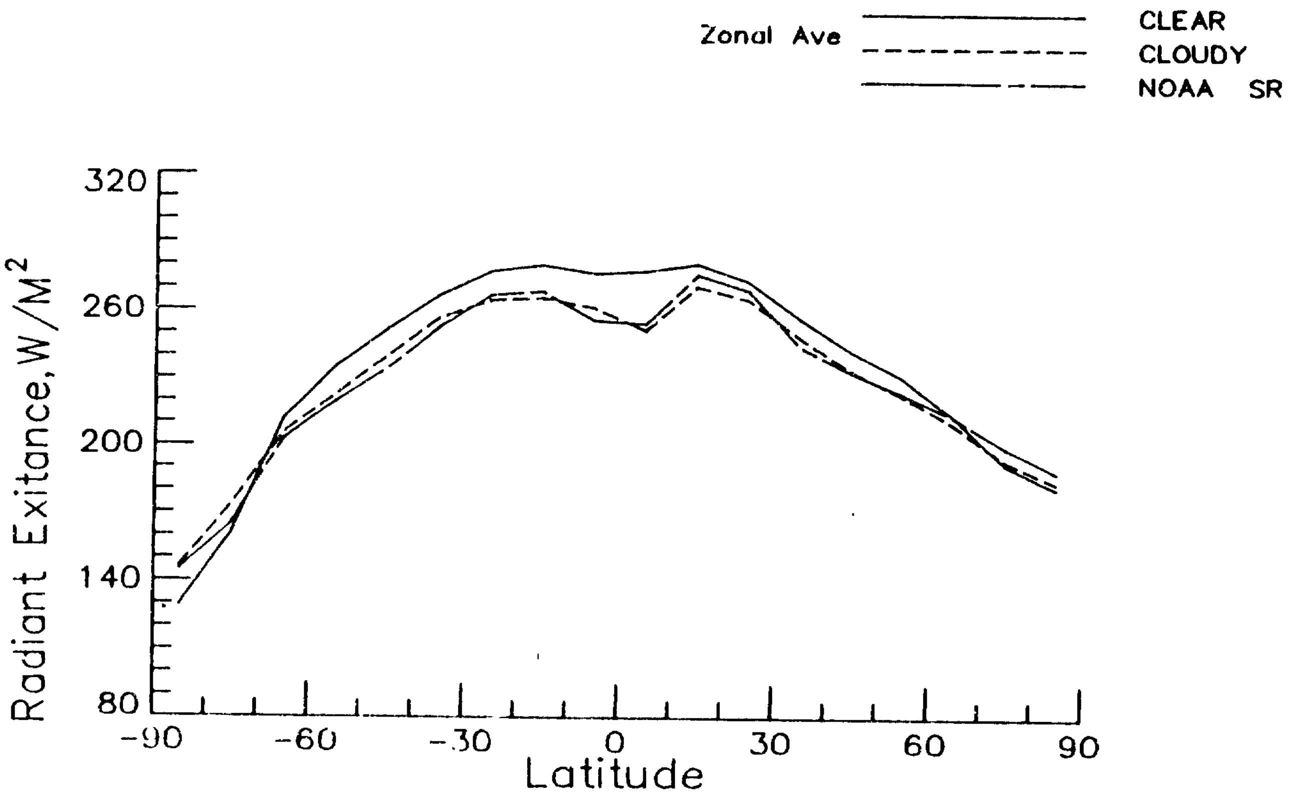

A.1 Zonally averaged CD, CR and NOA for April.

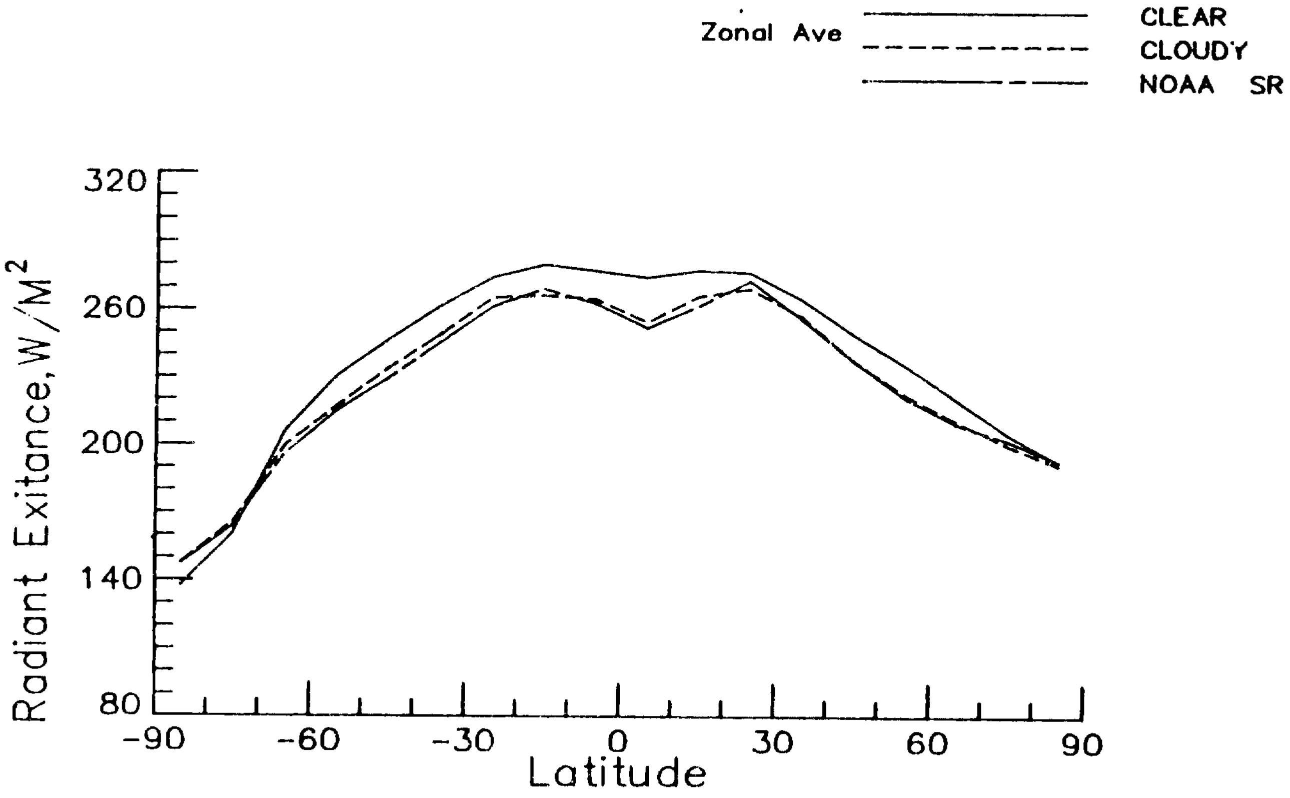

A.2 Zonally averaged CD, CR and NOA for October.

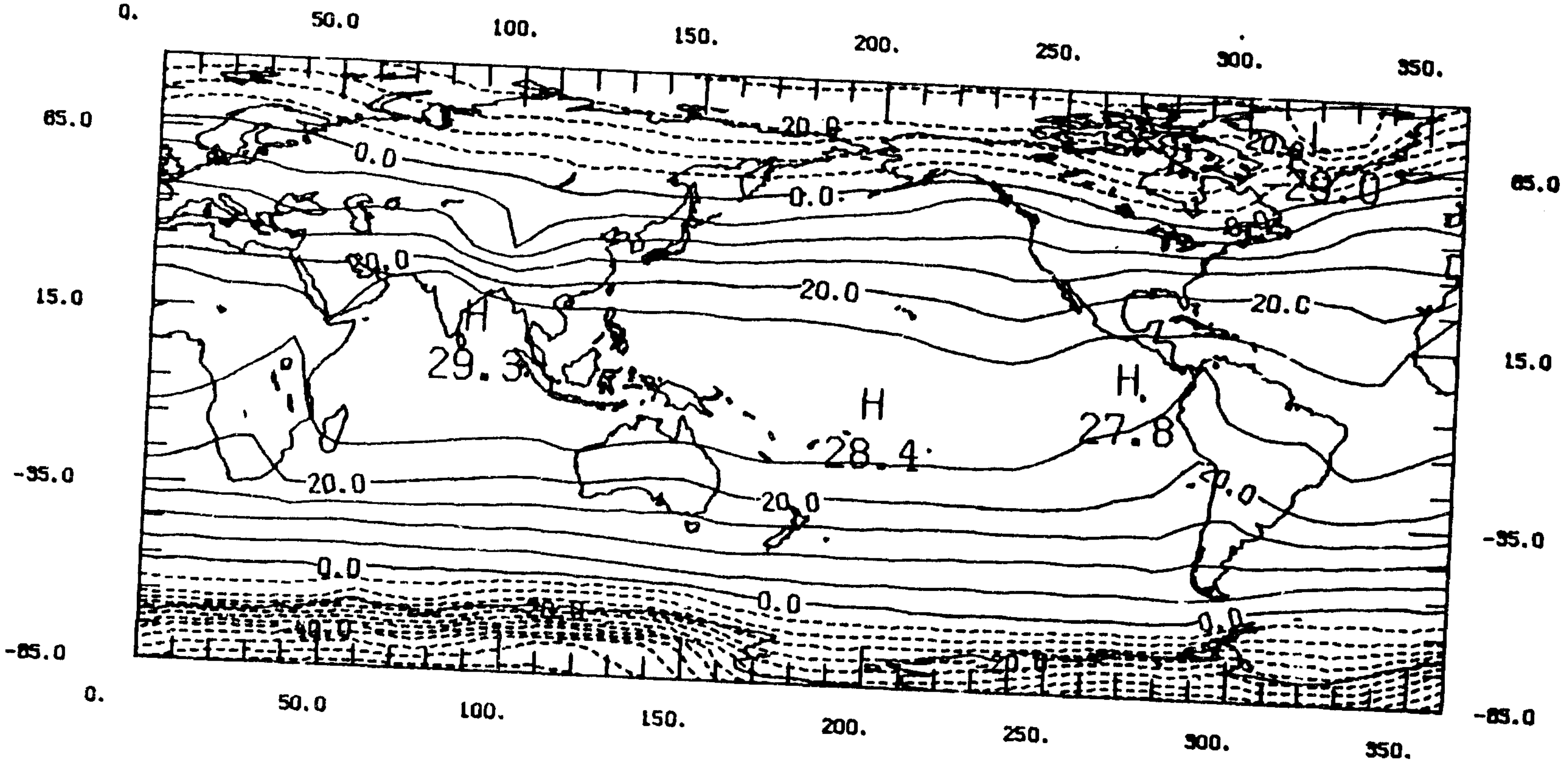

A.3 Climatological T_s map for April, in °C.

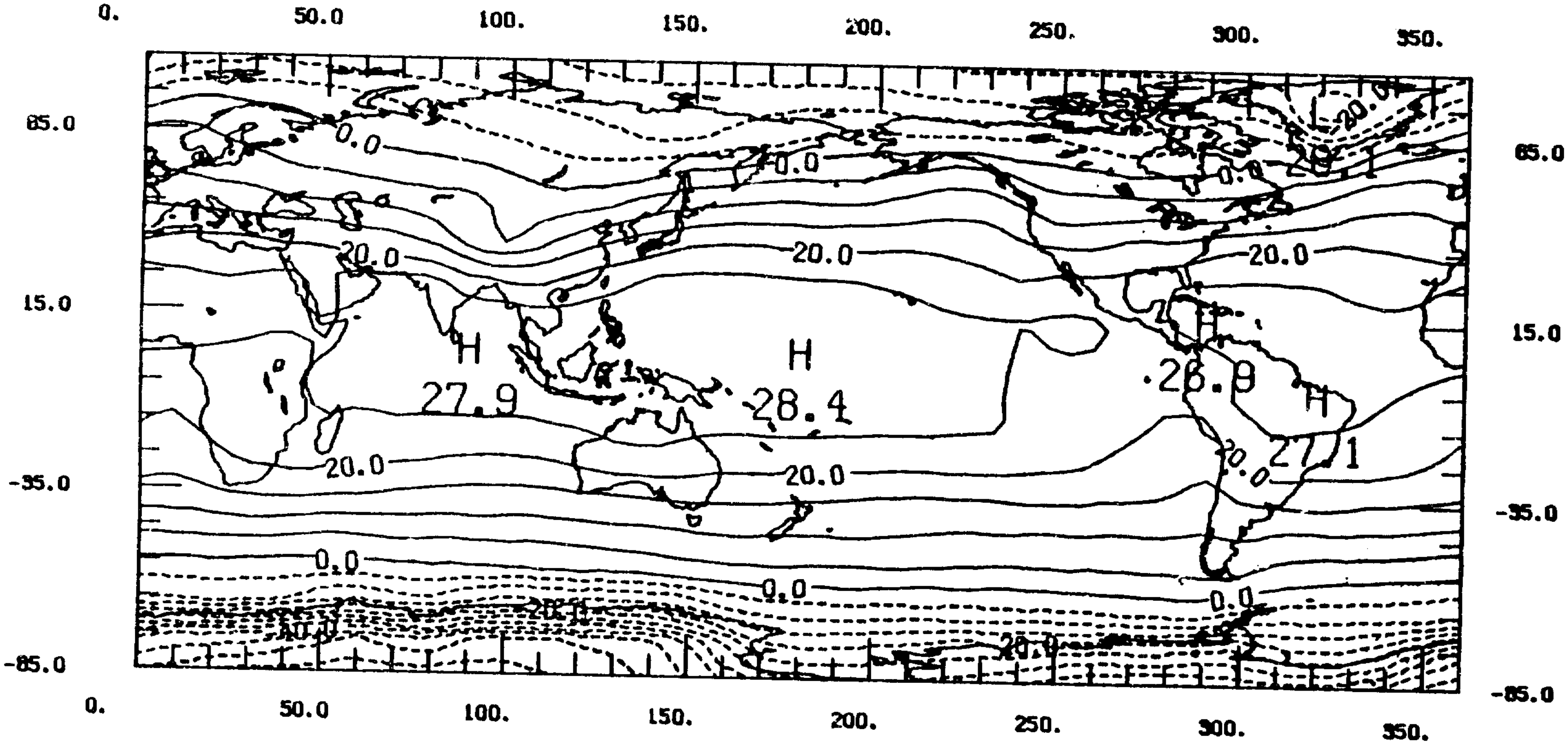

A.4 Climatological T_s map for October, in ^oC.

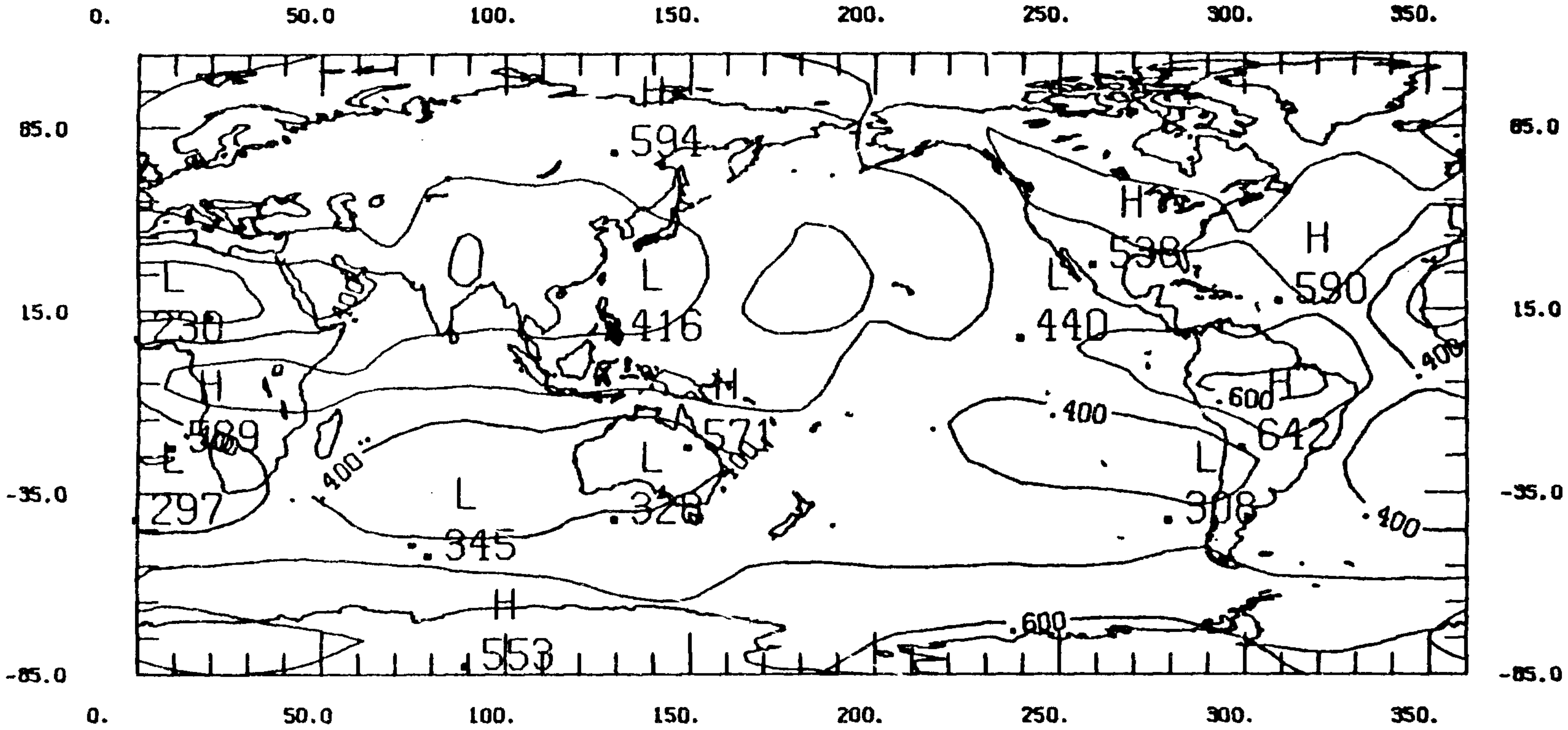

A.5 RH map for April.

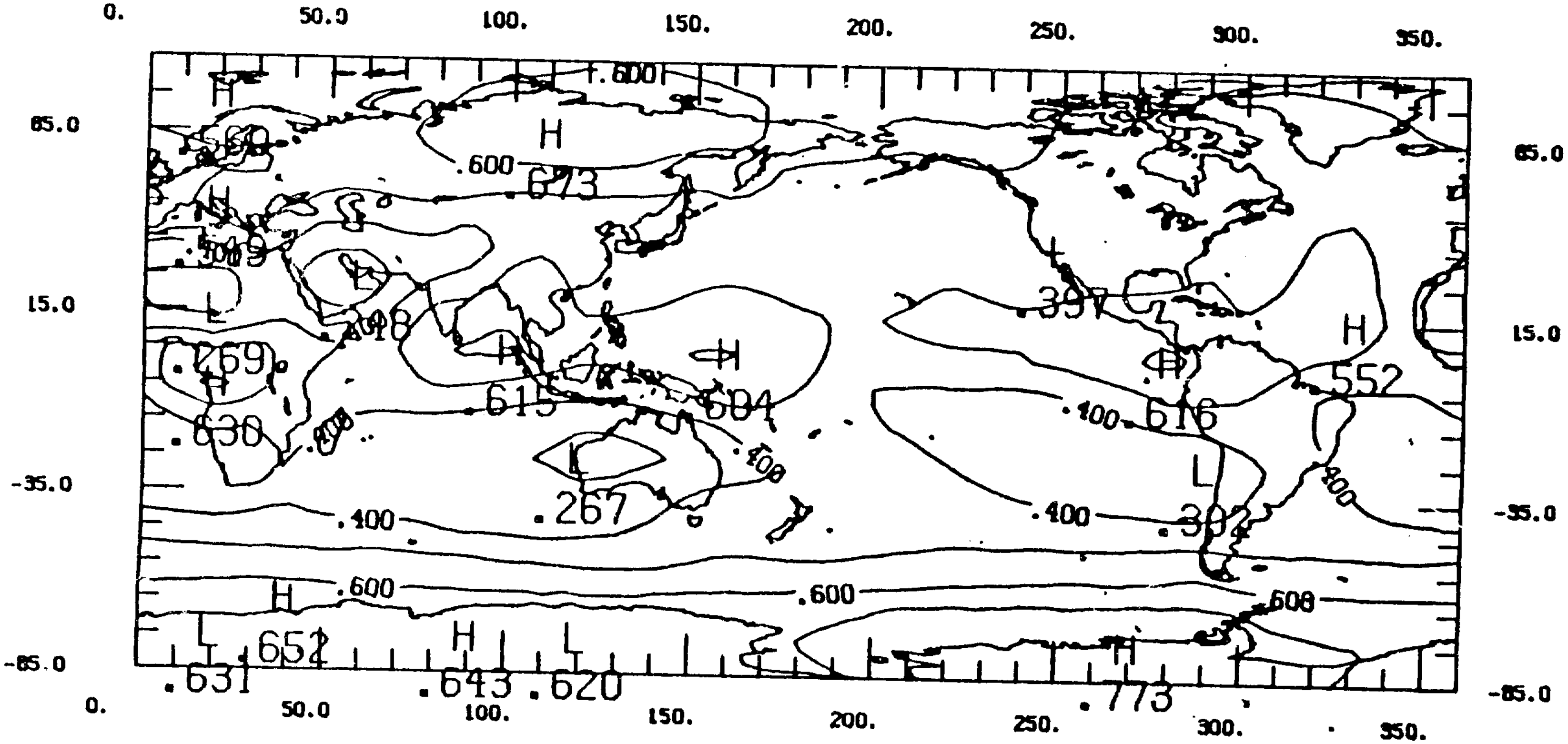

A.6 RH map for October.

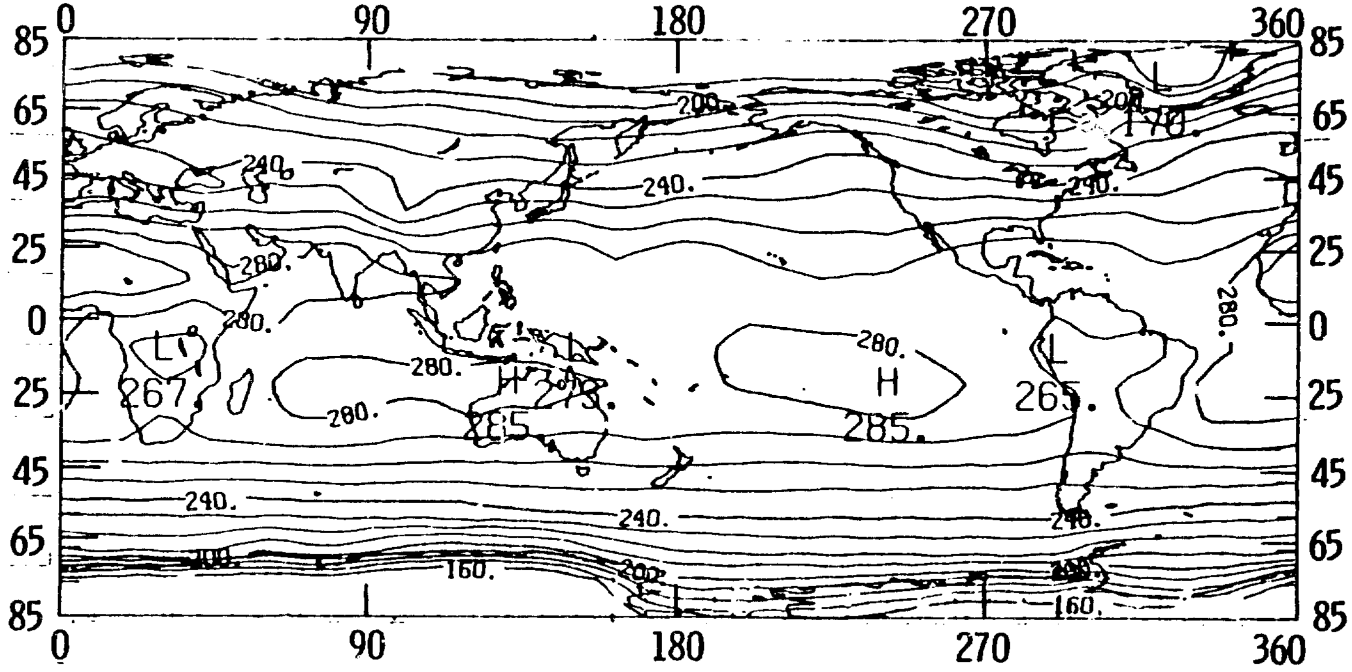

A.7 Clear sky OLWR map for April, in W/m^2.

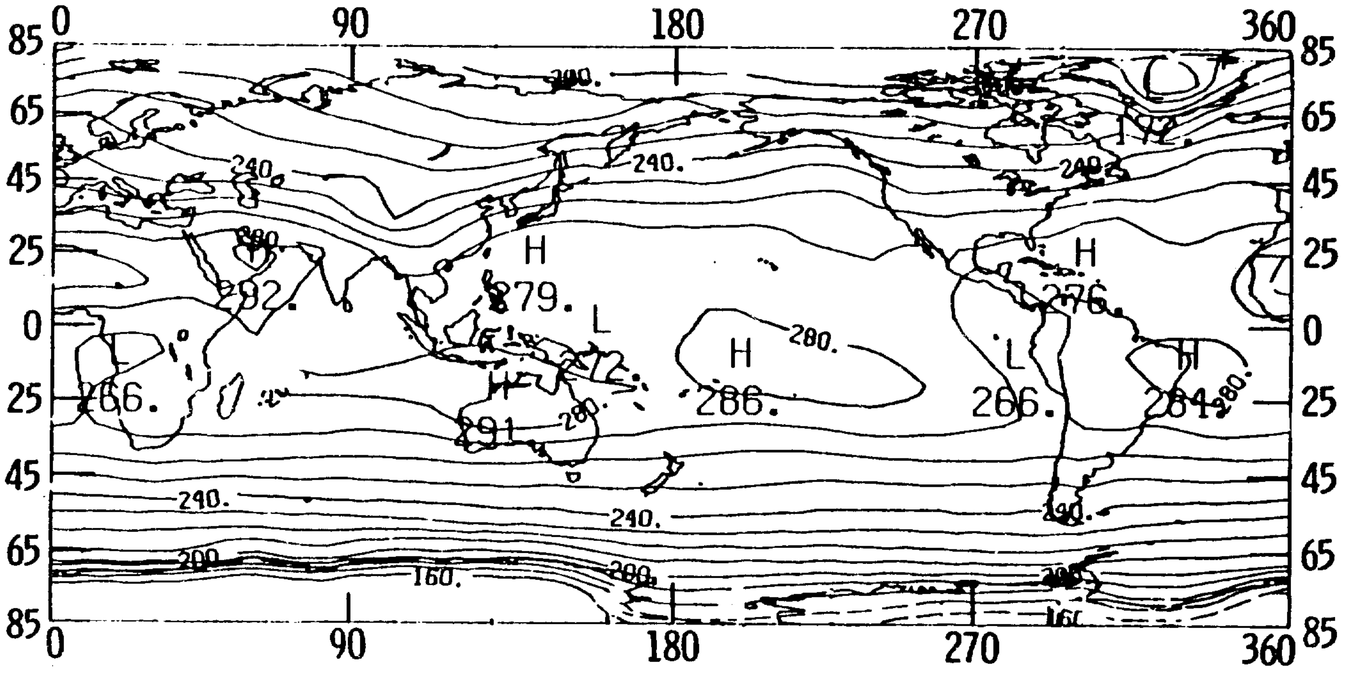

A.8 Clear sky OLWR map for October, in W/m^2.

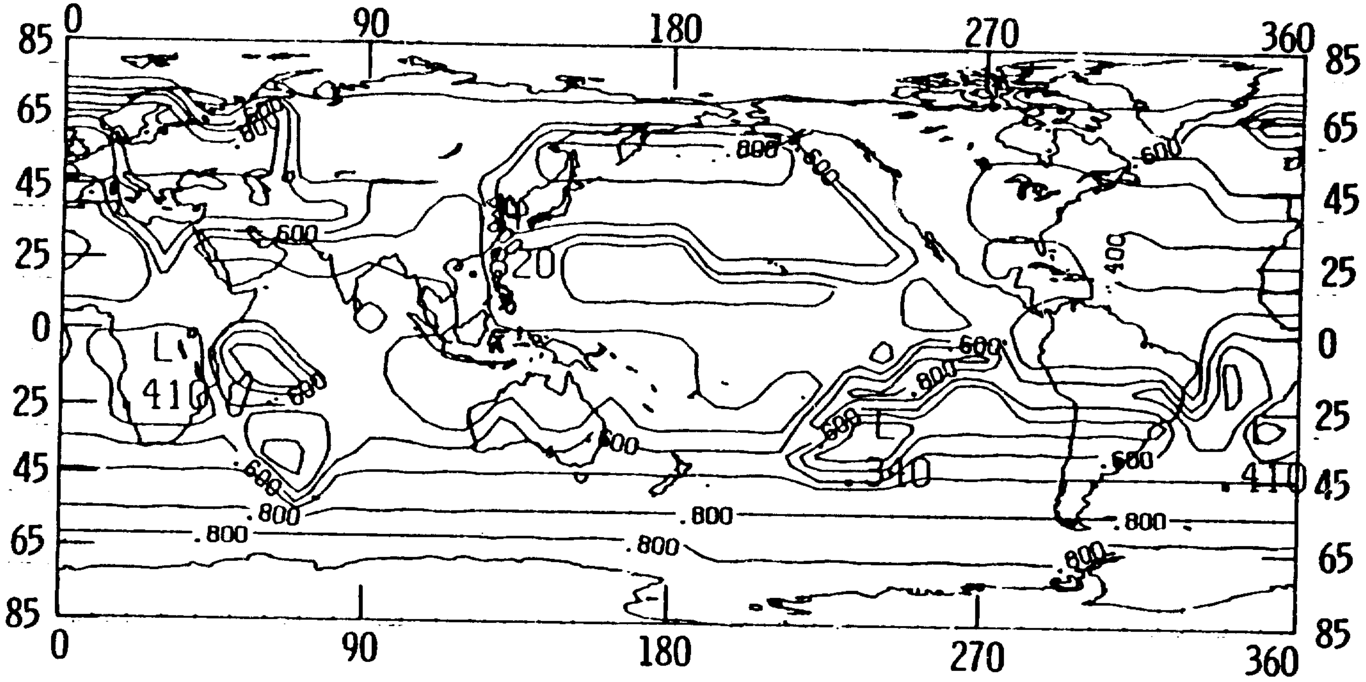

A.9 Cloud cover map for April.

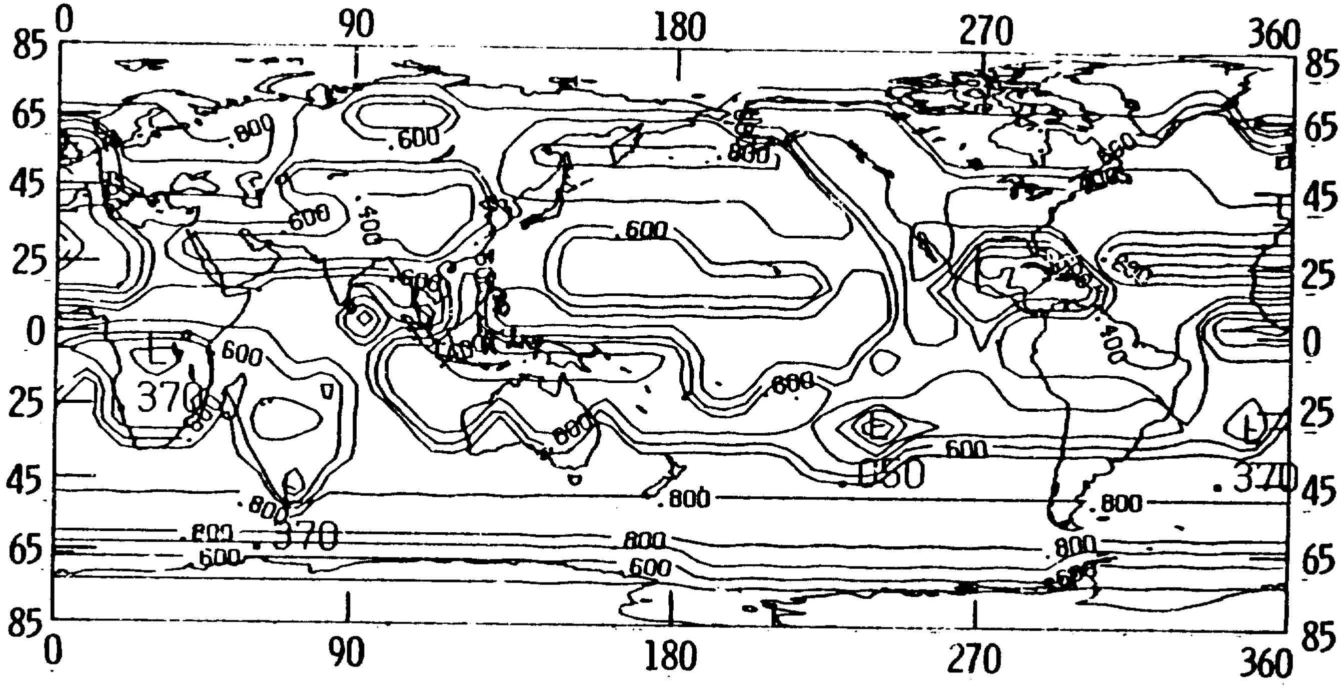

A.10 Cloud cover map for October.

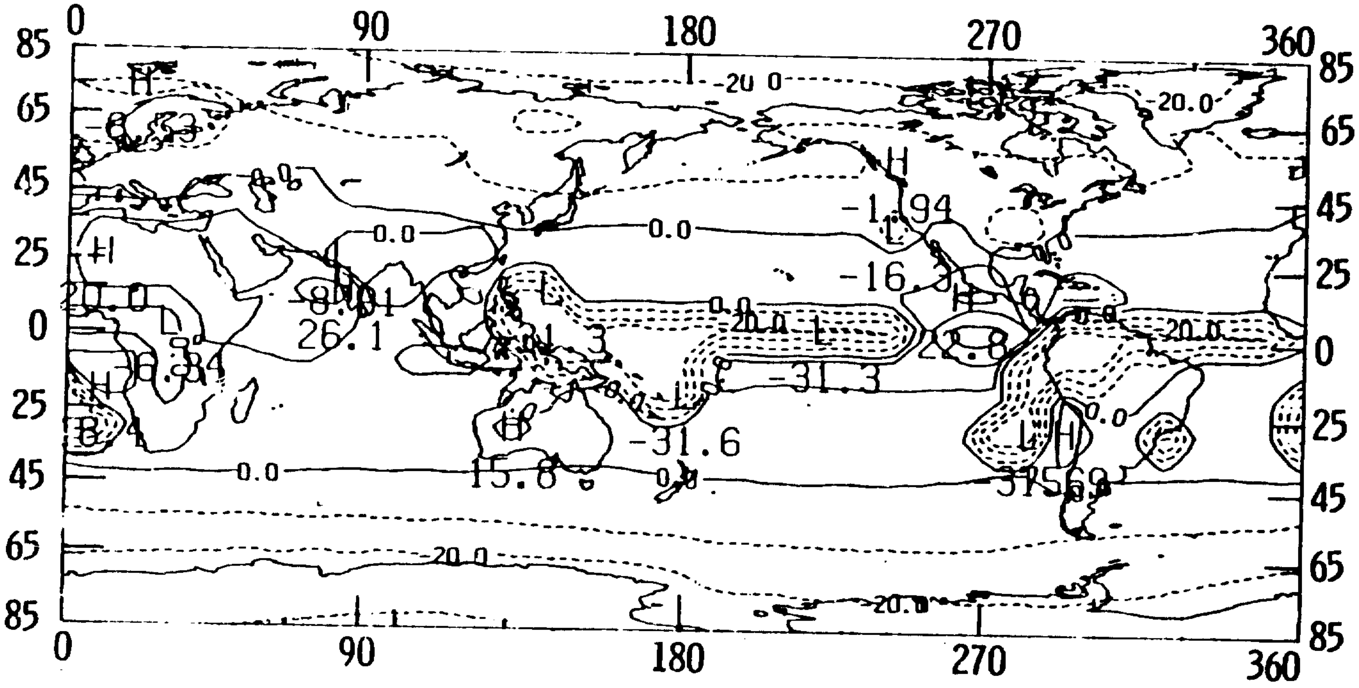

A.11 T_c map for April, in °C.

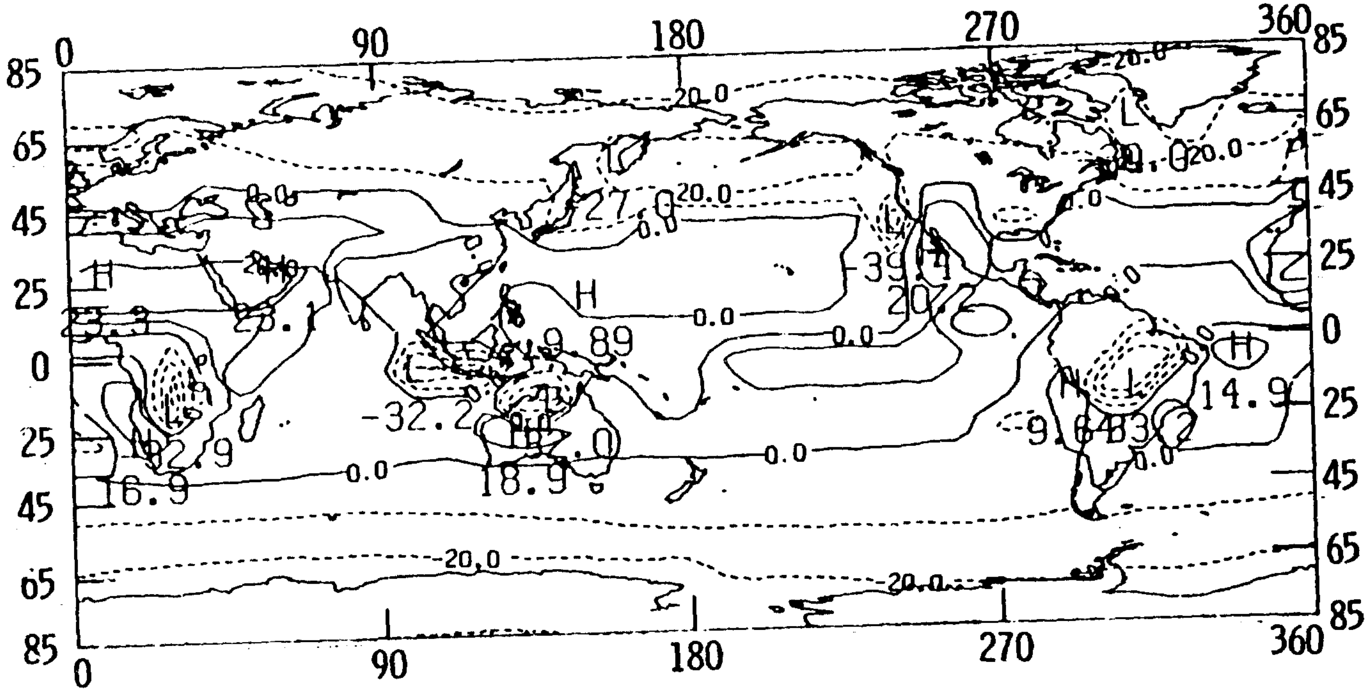

A.12 T_c map for October, in °C.

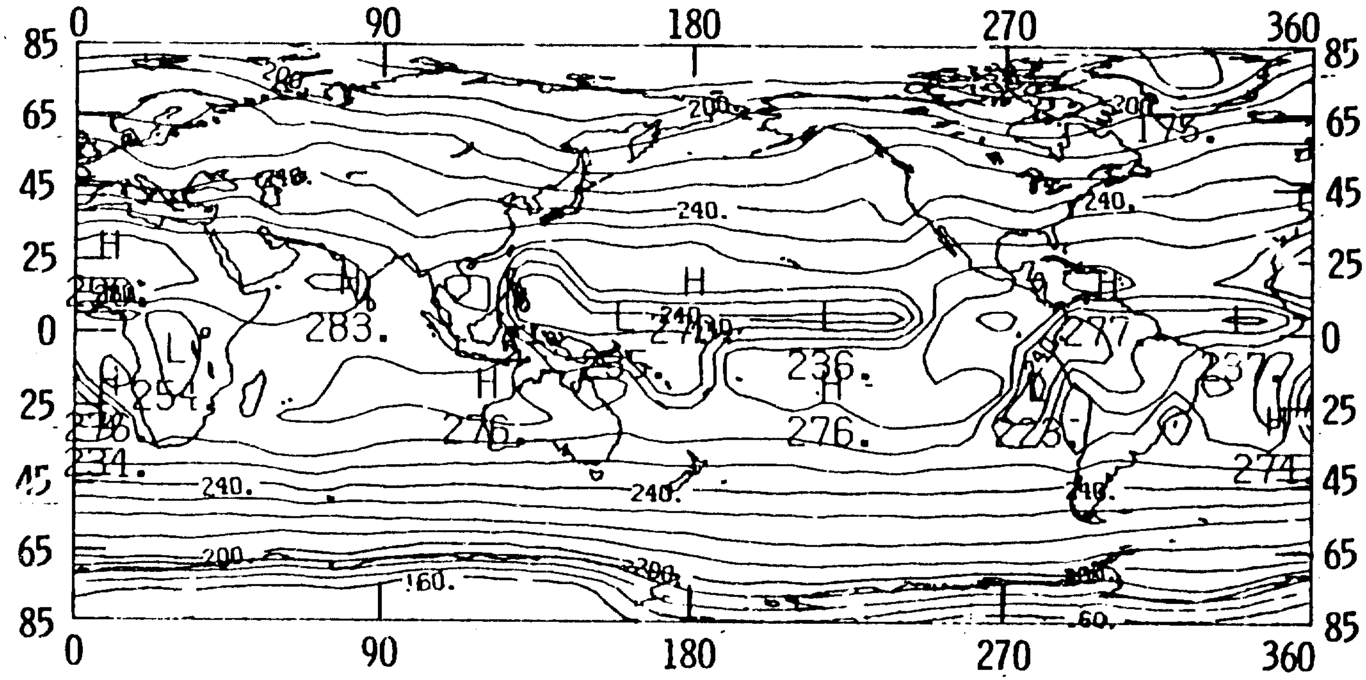

A.13 CD map for April, in W/m^2.

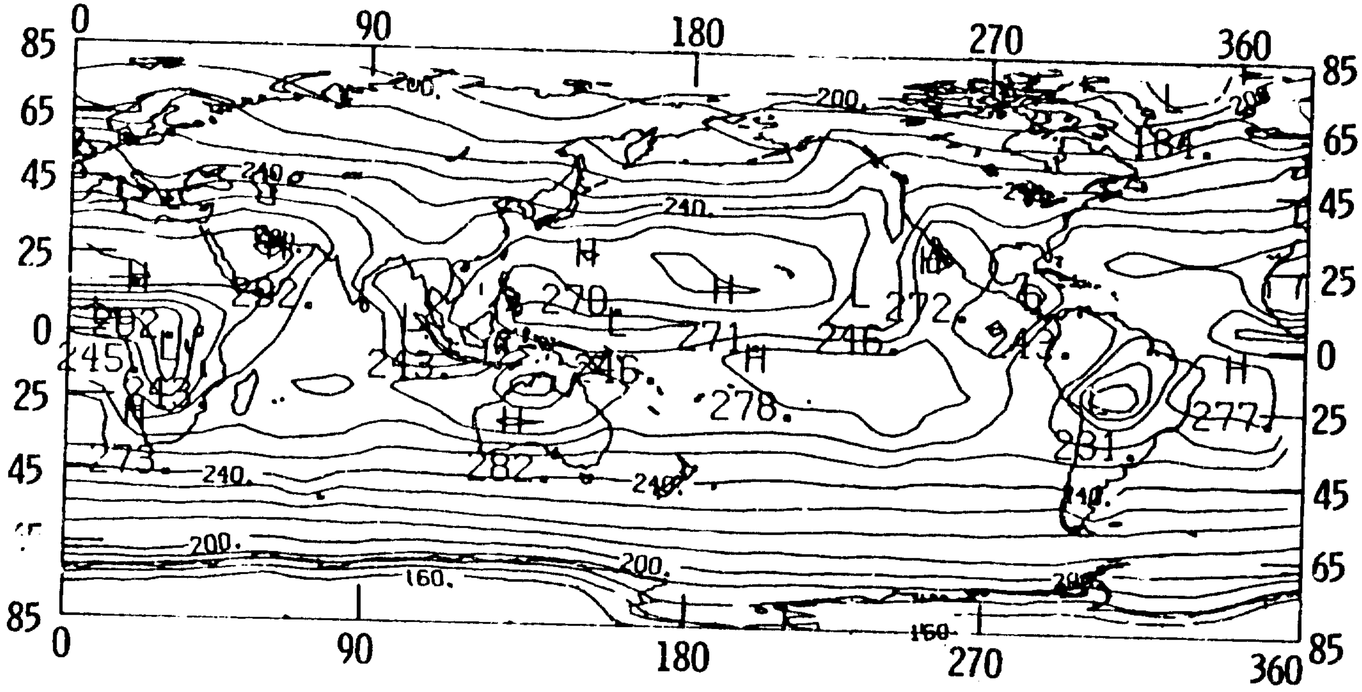

A.14 CD map for October, in W/m^2.

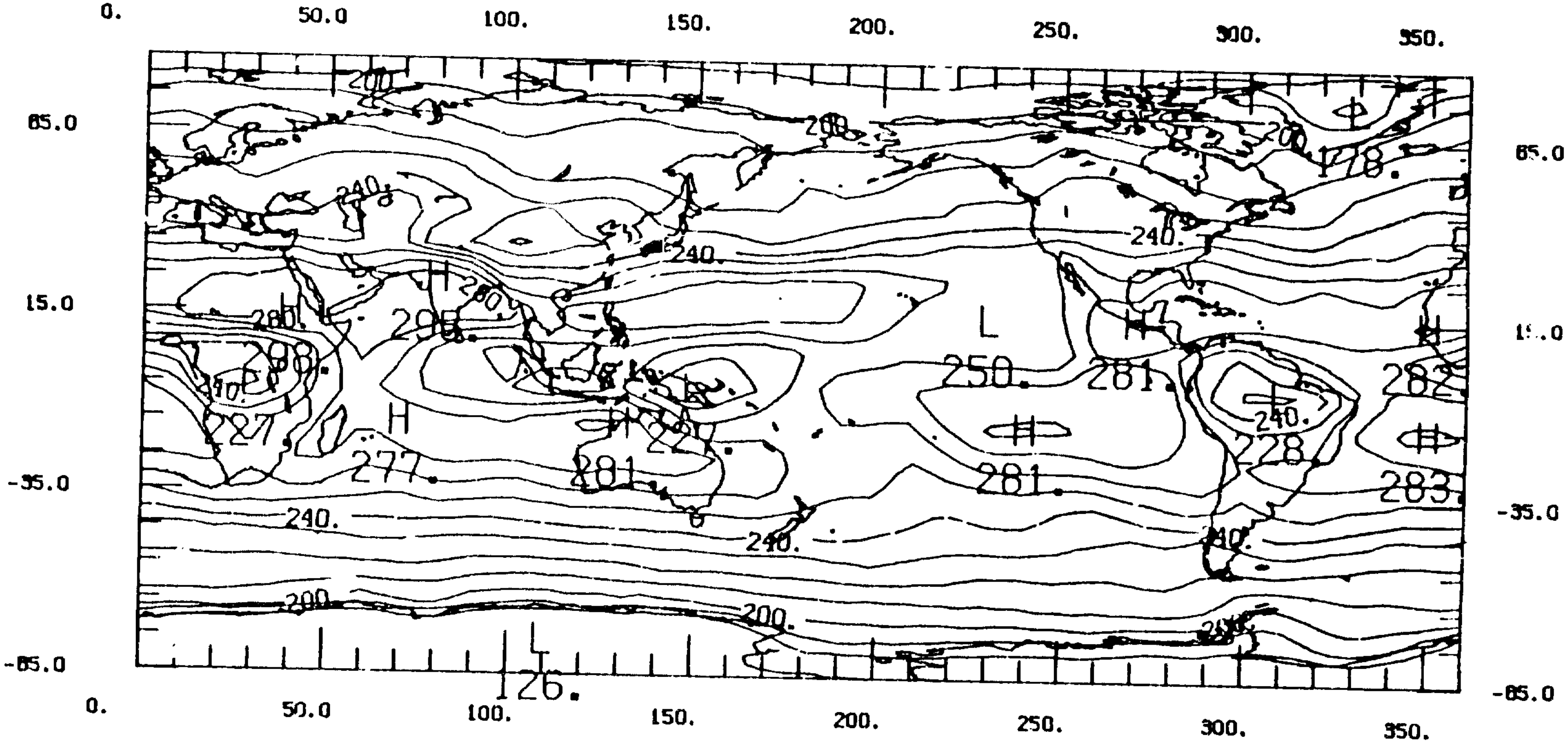

A.15 NOA map for April, in W/m^2.

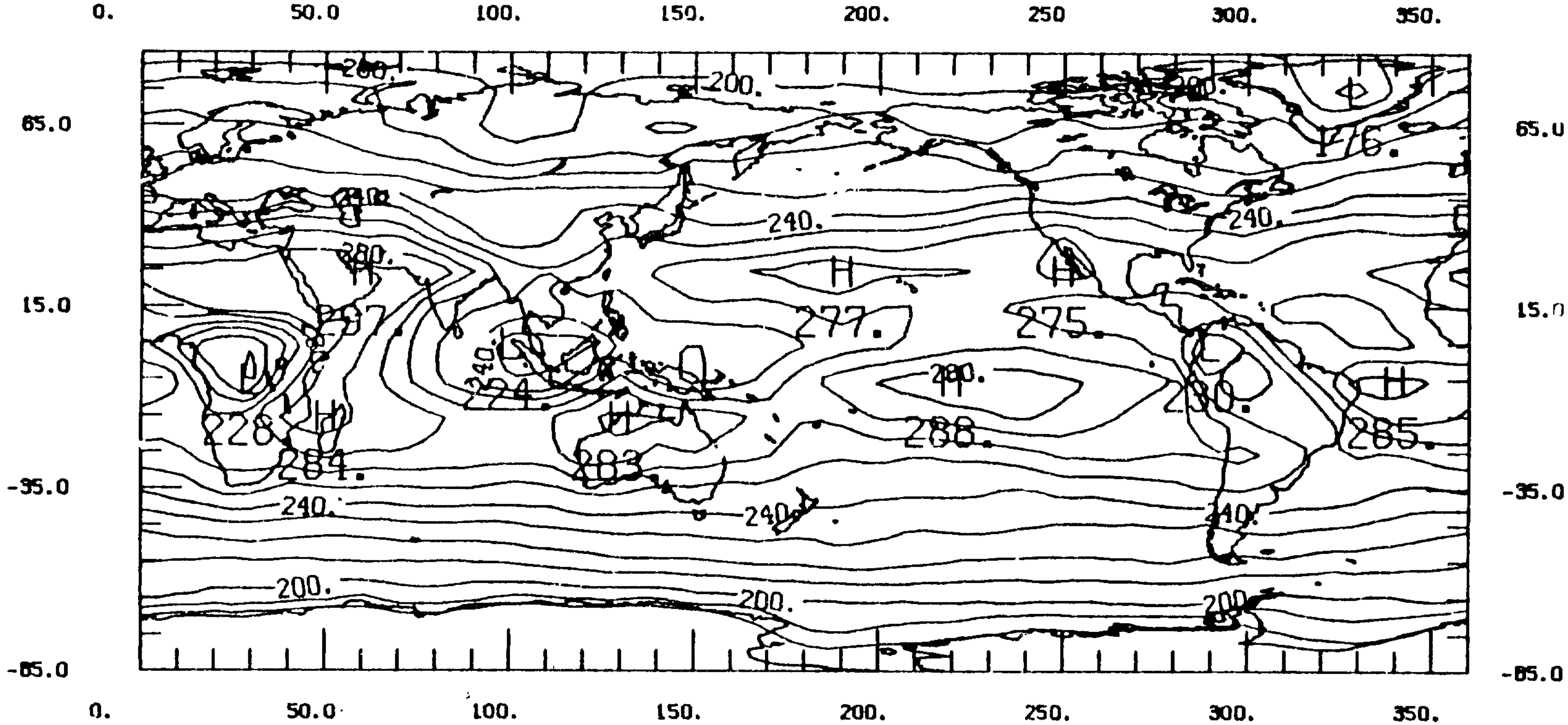

A.16 NOA map for October, in W/m^2.

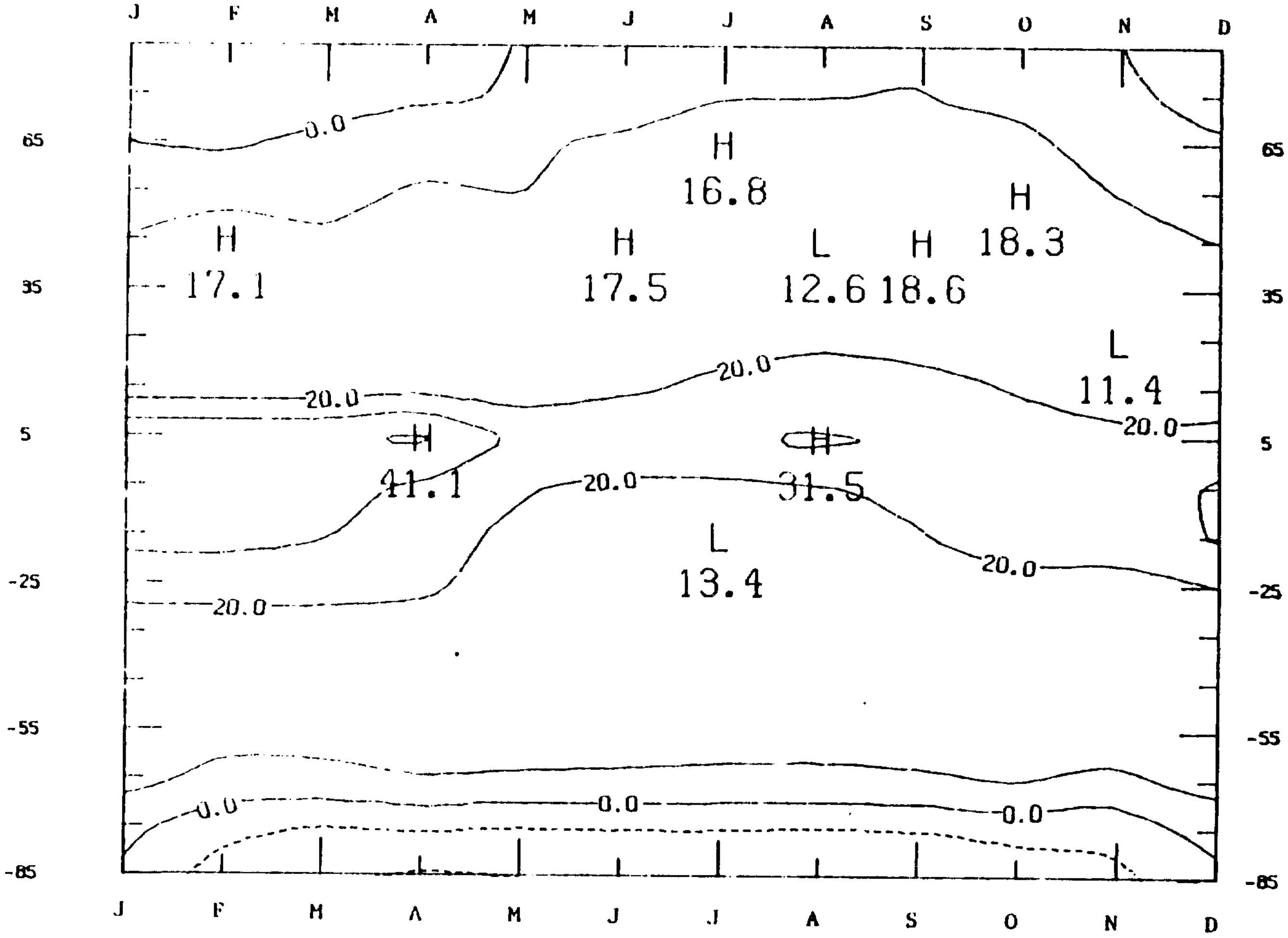

A.17 Time history of T_s-T_c, in ^oK.

A.18 Comparison of the coefficent values from different OLWR parameterizations after Gupta *et al.* (1978); see Equation 2.2 for C_1 and C_2, Z_c is assumed black cloud height.

Reference	C_1 Cal cm^{-2} min^{-1}	C_2 Cal cm^{-2} min^{-1}
Budyko (1969) (empirical)	0.367	0.103
Cess (1974) (Z_c= 6.8 km)	0.368	0.102
Schneider (1972) (Z_c= 5.5 km)	0.399	0.107
Gupta et al. (1978) (Z_c= 6 km)	0.367	0.099

* 100 W/m^2 = 0.144 Cal cm^{-2} min^{-1}

BIBLIOGRAPHY

BIBLIOGRAPHY

Abel, P., and A. Gruber, 1979: An Improved Model for the Calculation of Longwave Flux at 11 µm NOAA Tech. Rep. NESS 106, 24 pp. (NTIS PB 80-119431)

Adem, J., 1969: Numerical Prediction of Mean Monthly Ocean Temperature *JGR*, pp. 1104.

Adem, J., and W. Donn, 1981: Progress in Monthly Climate Forcasting with a Physical Model, *Bull. Ameri. Meteor. Soci.*, 12, No. 12.

Bartman, F., 1980: A Time Variable Model of Earth's Albedo, NASA Contractor Report 159259.

Bartman, F., 1981: Time-Variable Earth's Albedo Model Characteristics and Application to Satellite Sampling Error. NASA Contractor Report 165781.

Bean, S. J., and P. N. Somerville, 1981: Some New Worldwide Cloud-Cover Models. *J. Appl. Meteo.*, *V.* 20, pp. 223-228.

Belov, P. N., L. V. Berkovich, R. L. Alpatova and L. S. Bushueva, 1971: Experiments on Incorporating Radiative Heat Influx in Numerical Forcasting. Advances in Satellite Meteorology, John Wiley & Sons. 305 pp.

Bess, T., R. Green and G. L. Smith, 1981: Deconvolution of Wide Fieldof-View Radiometer Measurements of Earth Emitted Radiation. Part II: Analysis of First Year of Nimbus 6 ERB Data. *J. Atmos. Sci.*, pp. 474.

Briegleb, B., and V. Ramanathan, 1982: Spectral and Diurnal Variations in Clear Sky Planetary Albedo. *J. Appl. Meteo.*, pp. 1160.

Brooks, D., and P. Minnis, 1984: Comparison of Longwave Diurnal Models Applied to Simulations of the Earth Radiation Budget Experiment. *J. Climate Appl. Meteo.*, *V* 23, pp.155-160.

Budyko, M., 1969: The Effect of Solar Radiation Variations on the Climate of the Earth. *Tellus*, *V.* 21, pp. 611.

Campbell, G., and T. Vonder Haar, 1980: Climatology of Radiation Budget Measurements from Satellites. Atoms. Sci. Paper No. 323, Colorado State University, 74 pp.

Cess, R. D., 1974: Radiative Transfer Due to Atmospheric Water Vapor: Global Considerations of the Earth's Energy Balance. *J. Quant. Spectros. Radiat. Transfer*, *V* 14, pp. 861-871.

Cess, R. D., and V. Ramanathan, 1978: Averaging of Infrared Cloud Optics for Climate Modeling. J. Atmos. Sci., V. 35, pp. 919-922.

Cess, R. D., B. P. Briegleb, and M. S. Lian, 1982: Low-Latitude Cloudiness and Climate Feedback: Comparative Estimates from Satellite Data. J. Atmos. Sci., V.39, pp. 53-59

Chahine, M. T., R. Haskins, J. Susskind, and D. Reater, 1983: Remote Sensing of Weather and Climate Parameters. Prac. 5th Conference on Atmospheric Radiation, Oct. 31-4 Nov. Balitmore, MD. Amer. Meteo. Soc.

Charlock, T. P., 1984a: Wavenumber Dependent Investigation of the Terrestrial Infrared Radiation Budget with Two Versions of the LOWTRAN 5 Band Model. J. Climate and Appl. Meteo., V 23. pp. 25-33.

Charlock, T. P., 1984b: CO_2 Induced Climatic Change and Spectral Variations in the Outgoing Terrestrial Infrared Radiation. Tellus, V. 36B, pp. 139-148.

Clapp, P. F., 1964: Global Cloud Cover for Seasons Using TIROS Nephanalyses. Mon. Weather Rev., V 92, pp. 495-507.

Coakley, J. A., and F. P. Bretherton, 1982: Cloud Cover from High-Resolution Scanner Data: Detecting and Allowing for Partially Filled Fields of View. J. Geophy. Res., V 87, pp. 4917-4932.

Coakley, J. A., and G. W. Grams, 1976: Relative Influence of Visible and Infrared Optical Properties of a Stratospheric Aerosol Layer on the Global Climate. J. Appl. Meteo., V 15. pp. 679-691.

Crutcher, H., and J. Meserve, 1970: Selected Level Heights, Temperatures and Dew Points for the Northern Hemisphere. NAVAIF 50-1C-52 (Revised), Chief of Naval Operations. Washington, DC. 17p. plus charts.

Curran, R. J., and Man-Li Wu, 1982: Skylab Near-Infrared Observations of Clouds Indicating Super Cooled Liquid Water Droplets. J. Atmos. Sci., V 39. pp. 635-636.

Drayson, S. R., 1967: Calculation of Longwave Radiative Transfer in Planetary Atmosphere, Ph.D. thesis, Rep. 07584-1-T, 170 pp., College of Engineering., University of Michigan, Ann Arbor, MI.

Ellingson, R. and Ferraro, 1983: An Examination of a Technique for Estimating the Longwave Radiation Budget from Satellite Radiance Observation. J. Climate Appl. Meteo., pp. 1416-1423.

Ellasser, H. W., 1983: Stratospheric Water Vapor. J. Geophys. Res., V 88, pp. 3897-3906.

Falls, L. W., 1974: The Beta Distribution: A Statistical Model of World Cloud Cover. J. Geophys. Res., V 79. pp. 1261-1264.

Fromm, M. D., L. M. Peen, J. J. Cahir, and H. A. Panofsky, 1982: Statistical Estimates of Monthly Mean and International Change of Radiation Fluxes at the Top of the Atmosphere. JAS, V 39, pp. 1545-1554.

Gill, A. E., and E. M. Rasmusson, 1983: The 1982-83 Anamaly in the Equatorial Pacific. Nature, V 306, pp.229-234

Gruber, A., 1972: Fluctuations in the Position of the ITCZ in the Atlantic and Pacific Oceans. J. Atmos. Sci., V 29, pp. 193-197.

Gupta, S. K., S. N. Tiwari, and J.,T. Suttles, 1978: Longwave Radiative Transfer in the Atmosphere. Proc. 3rd Conference on Atmospheric Radiation. Jun 28-30. Davis, CA Amer. Meteo. Soc.

Harries, J., 1976: The Distribution of Water Vapor in the Stratosphere Rev. Geophys. Space Phys., 14, pp. 565.

Hartman, D. L., 1983: Radiation Budget Study. Proc. 5th Conference on Atmospheric Radiation. Oct. 31-Nov. 5. Baltimore, MD.

Henderson-Sellers, A., 1978: Surface Type and its Effect Upon Cloud Cover: A Climatological Investigation. J. Geophys. Res., V 83, pp. 5057-5062.

Herman, G., 1981: Cloud-Radiation Experiments Conducted with GLAS General Circulation Models. Proc. of Workshop on Radiation and Cloud-Radiation Interaction in Numerical Modeling. European Center for Medium Range Weather Forecasts.

Hoyt, D. V., 1976: The Radiation and Energy Budgets of the Earth Using Both Ground-Based and Satellite-Derived Values of Total-Cloud Cover. NOAA Technical Report ERL 362-ARL 4, April.

Hummel, J. R., and W. R. Kuhn, 1983: Calculating Multiple Cloud Cover Amounts from Climatic Data for Use in Climate Studies. IAMAP, Hamburg. 15-27 Aug, 1983. International Union of Geodesy & Geophysics XVII, General Assembly.

International Cloud Atlas, Volume I, 1975: Manual on the Observation of Cloud and Other Meteors. WMO-No.407, World Meteorological Organization, Geneva, Switzerland.

Jenne, R., H. Crutcher, H. von Loon, and J. Taljaard, 1974: A Selected Climatology of the Southern Hemisphere: Computer Methods and Data Availability. NCAR Technical Note STR-92.

Jensenius, J. S., J. J. Cahir, and H. A. Panofsky, 1978: Estimation of Outgoing Longwave Radiation from Meteorological Variable Accessible from Numerical Models. Quart. J. R. Met. Soc. V 104, pp. 119-130.

Kandel, R., 1983: Satellite Observation of the Earth Radiation Budget. Beitr. Phys. Atmos., V 56 No.3, pp. 322-340

Kiehl, J. T., 1983: Satellite Detection of Effects Due To Increased Atmospheric Carbon Dioxide. Science, V. 222, pp. 504-506.

Kneizys, F. X., E. P. Shettle, W. D. Gallery, J. H. Chetwynd, Jr., L. W. Abreu, J. E. Selby, R. W. Fenn, and R. A. McClatchey, 1980: Atmospheric Tranmittance/Radiance: Computer Code LOWTRAN 5, AFGL-TR-80-0067, Air Force Geophysics Laboratory, Hanscom AFB, MA. [NTIS ADA 088215].

Kornfield, J., and F. Hasler, 1969: A Photographic Summary of the Earth's Cloud Cover for the Year 1967. J. Appl. Meteo., V 8, pp. 687-700.

Kuhn, W. R., 1978: Effects of Cloud Height, Thickness and Overlap on Tropospheric Terrestrial Radiation. J. Geophys. Res., V 83. pp. 1337-1346.

Lau, W., and P. Chan, 1983: Atmospheric Teleconnection from Satellite Observation. Second Conference on Climate Variation, New Orleans, January. Ameri. Meteo. Soci.

Liou, K. N., 1980: An Introduction to Atmospheric Radiation. Academic Press. pp. 11 and pp. 340.

List, R. J., 1959: Smithsonian Meteorological Tables, 6th Rev. Ed. Washington, D.C., Smithsonian Institution, 527 pp.

London, J., 1957: A Study of the Atmospheric Heat Balance. Report, Contract AF 19(22)-165, College of Engineering, New York University [NTIS PB 115626].

Luther, F. M., 1983: Results of a Comparison of Infrared Radiative Transfer Model IAMAP, Hamburg. 15-27 Aug. 1983. International Union of Geodesy and Geophysics XVII, General Assembly.

Manabe, S., and R. T. Wetherald, 1967: Thermal Equilibrium of the Atmosphere With a Given Distribution of Relative Humidity. J. Atmos. Sci., V 24, pp. 241-259.

Mastenbrook, H. J., 1968: Water Vapor Distribution in the Stratosphere and High Troposphere. J. Atmos. Sci., V 25, pp. 299-311.

McClatchey, R. A., R. W. Fenn, J. E. Selby, F. E. Volz, and J. S. Garing, 1972: Optical Properties of the Atmosphereic, 3rd ed. AFCRL-72-0497, Air Force Geophysics Laboratory. Hanscom AFB, MA [NTIS AD 753075]

Minnis, P., and E. Harrison, 1983: Diurnal and Seasonal Variation of Clouds from Geostationary Satellite Data. Proc. 5th Conference on Atmospheric Radiation. Oct. 31-Nov. 4. Baltimore, MD. Amer. Meteo. Soci.

Minnis, P., and E. Harrison, 1984: Diurnal Variability of Regional Cloud and Clear-Sky Radiative Parameters Derived from GOES Data. J. Climate Appl. Meteo., V 23, No.7, pp.993-1051, 3 parts.

Newell, R. E., J. W. Kidson, D. G. Vincent, and G. J. Boer, 1972: The General Circulation of the Tropical Atmosphere and Interaction with Extratropical Latitudes, V 1, the MIT Press. 258 pp.

North, G., 1975: Theory of Energy-Balance Climate Models. J. Atmos. Sci., V 32, pp. 2033.

Ohring, G., and P. Clapp, 1980: The Effect of Changes in Cloud Amount on the Net Radiation at the Top of the Atmosphere. J. Atmos. Sci. V 37. pp. 447-454.

Oort, A. H., and E. M. Rasmusson, 1971: Atmospheric Circulation Statistics. NOAA Prof. Pap. No. 5, U.S. Dept. of Commerce, Rockville, MD.

Oort, A. H., 1983: Global Atmospheric Circulation Statistics, 1958-1973, NOAA Professional Paper No. 14, U.S. Goverment Printing Office, Washington, DC., 180pp + 47 microfiches.

Parish, O., and T. Putnam, 1974: Equations for the Determination of Humidity from Dew Point and Psychrometric Data. [NASA TN D-8401].

Quiroz, R., 1983: Seasonal climate Summary: The Climate of the "El Nino" winter of 1982-1983-- A Season of Extraordinary Climate Anomalies. Month. Wea. Rev., V 111, pp. 1685-1706.

Ramanathan, V., 1976: Radiative Transfer Within the Earth's Troposphere and Stratosphere: A simplified Radiative-Convective Model. J. Atmos. Sci., V 33, pp. 1330-1346.

Ramanathan, V., and J. A. Coakley, 1978: Climate Modeling Through Radiative-Convective Models. Rev. Geophy. Spa. Phys., V. 16, pp. 465-489.

Ramanathan, V., M. S. Lian, and R. D. Cess, 1979: Increased Atmospheric CO_2: Zonal and Seasonal Estimates of the Effect on the Radiation Energy Balance and Surface Temperature. J. Geophys. Res., V 84, 4949-4958.

Reck, R. A., 1974: Influence of Surface Albedo on the Change in the Atmospheric Radiation Balance Due to Aerosols. Atmos. Environ., V 8, pp. 823-833.

Richards, J. M., 1971: A Simple Expression for the Saturation Vapor Pressure of Water in the Range -50° to 140°C. J. Phys. D.: Appl. Phys., V 4, L15-L18. (and Corrigendum p. 876).

Rodgers, C. D., and C. D. Walshaw, 1966: The Computation of Infrared Cooling Rate in Planetary Atmosphere, Quart. J. Roy. Meteorol. Soc., V 92, pp. 67-92.

Routhier, F., and D. Davis, 1980: Free Tropospheric/Boundary-Layer Airborne Measurement of H_2O Over the Latitude Range of 58°S to 70°N: Comparison with Simultaneous Ozone and Carbon Monoxide Measurement. J. Geophy. Res., V 85, pp. 7293-7306.

Russell, J. M., J. C. Gille, E. E. Remsberg, L. L. Gordley, P. L. Bailey, H. Fischer, A. Girard, S. R. Drayson, W. F. Evans, and J. E. Harries, 1984: Validation of Water Vapor Results Measured by the LIMB Infrared Monitor of the Stratosphere (LIMS) Experiment on NIMBUS 7. J. Geophy. Res., V. 89.

Sasamori, T., J. London, and D. V. Hoyt, 1972: Radiation Budget of the Southern Hemisphere. Meteor. Monogr., No. 35, Amer. Meteor. Soc.

Saunders, R. and G. Hunt, 1980: Meteosat Observation of Radiation Budget Parameters. Nature, V 283, pp. 645-647.

Schiffer, R. A. and W. B. Rossow, 1983: The International Satellite Cloud Climatology Project (ISCCP): The First Project of the World Climate Research Programme. Bull. Amer. Meteor. Soc., V 64, pp. 779-784.

Schneider, S. H., 1972: Cloudiness as a Global Feedback Mechanism: The Effect of the Radiation Balance and Surface Temperature of Variations in Cloudiness, J. Atmos. Sci., V 29, pp. 1413-1422.

Sellers, W., 1969: A Global Climatic Model Based on the Energy Balance of the Earth-Atmosphere System. J. Appl. Meteo., V 8, pp. 392-400.

Shenk, W. E. and V. Salomoson, 1972: A Simulation Study Exploring the Effects of Sensor Spatial Resolution on Estimates of Cloud Cover from Satellite. J. Appl. Meteo., V 11, pp. 214-220.

Sherr, P., A. Glason, J. Barnes, and J. Willard, 1968: World-Wide Cloud Cover Distribution for Use in Computer Simulations. NASA Contractor Report CR61226, Allied Research Association. 140 pp. + charts.

Short, D. A., G. R. North, T. D. Bess, and G. L. Smith, 1984: Infrared Parameterization and Simple Climate Model. To be published by the J. Climate and Appl. Meteor.

Sirutis, J., K. Miyakoda and J. Ploshay, 1980: Moisture Distribution Derived in Mathematical Models and Four-Dimensional Analysis. Atmospheric Water Vapor, Academic Press, pp.489-496.

Smith, G. and R. Green, 1981: Deconvolution of Wide-Field-of-View Radiometer Measurement of Earth Emitted Radiation, Part I: Theory. J. Atmos. Sci., V 38. pp. 461.

Smith, W. L., 1966: Note on the Relationship Between Total Precipitable Water and Surface Dew Point. J. Appl. Meteo., V 5, pp. 726-727.

Suomi, V., 1960: Radiation Measurement of the Earth from and Artificial Satellite. Rockets and Satellites in IGY, Pergamon.

Taljaard, J., H. von Loon, H. Crutcher, and R. Jenne, 1969: Climate of the Upper Air: Southern Hemisphere, Vol. I, Temperatures, Dew Points and Heights at Selected Pressure Level. NAVAIR 50-1C-35, U. S. Navy, Washington, D. C.

Telegadas, K., and J. London, 1954: A Physical Model of the Northern Hemisphere Troposphere for Winter and Summer Scientific Report No. 1 AF 19(122)-165. Dept. of Meteo. and Ocean. College of Engineering, New York University.

Thompson, S., and S. Warren, 1982: Parameterization of Outgoing Infrared Radiation Derived from Detailed Raduatuve Calculations. J. Atmos. Sci., V 39, pp. 2667; Addendum and Corrigendum, V 40, pp. 1859.

U. S. Standard Atmospheric 1976, NOAA-S/T 76-1562.

von Loon, H., 1972: Cloudiness and Precipitation in the Southern Hemisphere. Meteorological Monographs, V 13, No. 35, pp. 101. Amer. Meteo. Soci.

Vonder Haar, T. H., P. Ciesielski, D. Randel, and D. Stevens, 1982: Radiation Budget Measurement/Model Interface. NASA Contract Report NAG-150.

Wallace, J., and P. Hobbs, 1977: Atmospheric Science, an Introductory Survey, Academic Press, pp. 321.

C-3

Wang, V., J. Zack, M. Kaplan, and S. Chung, 1983: An Numerical Inverstigation of the Effects of Cloudiness on Mesoscale Atmospheric Circulation. Proc. 5th Conference on Atmospheric Radiation. Oct 31Nov. 4, 1983. Baltimore, MD, Amer. Meteo. Soc.

Wang, W. C., and G. A. Domoto, 1974: The Radiative Effect of Aerosols in the Earth's Atmosphere, J. Appl. Meteorol., V 13, pp. 521-534.

Wang, W. C., Y. L. Yung, A. A. Lacis, T. Mo, and J. E. Hansen, 1976: Greenhouse Effects Due to Man-Made Perturbations of Trace Gases, Science, V 194, pp. 685-690.

Warren, S. G., C. Hahn, and J. London, 1983: Distribution of Six Cloud Types Over the Oceans and Their Diurnal and Interannual Variations. Proc. 5th Conference on Atmospheric Radiation. Oct. 31-Nov. 4, Baltimore, MD. Amer. Meteo. Soc.

Warren, S. and S. Thompson, 1983: The Climatological Minimum in Tropical Outgoing Infrared Radiation: Contribution of Humidity and Clouds. Quart. J. Roy. Meteor. Soc., 109, pp. 169.

Wiscombe, W. J., 1975: Solar Radiation Calculation for Arctic Summer Stratus Condition. Climate of the Arctic, G. Weller and S. A. Bowling, Eds. Geophysical Institute, University of Alaska, 245-254.

Wiscombe, W., 1976: Extension of the Doubling Method to Inhomogeneous Sources. J. Quart. Spectrosc. Radiat. Transfer., 16. pp. 447.

Wiscombe, W. J. and Evans, J. W., 1977: Exponential-Sum Fitting of Radiative Transmission Functions. J. Computational Physics., V 24, pp. 416-444.